# INFORMATION TO USERS

This manuscript has been reproduced from the microfilm master. UMI films the text directly from the original or copy submitted. Thus, some thesis and dissertation copies are in typewriter face, while others may be from any type of computer printer.

**The quality of this reproduction is dependent upon the quality of the copy submitted.** Broken or indistinct print, colored or poor quality illustrations and photographs, print bleedthrough, substandard margins, and improper alignment can adversely affect reproduction.

In the unlikely event that the author did not send UMI a complete manuscript and there are missing pages, these will be noted. Also, if unauthorized copyright material had to be removed, a note will indicate the deletion.

Oversize materials (e.g., maps, drawings, charts) are reproduced by sectioning the original, beginning at the upper left-hand corner and continuing from left to right in equal sections with small overlaps.

Photographs included in the original manuscript have been reproduced xerographically in this copy. Higher quality 6" x 9" black and white photographic prints are available for any photographs or illustrations appearing in this copy for an additional charge. Contact UMI directly to order.

Bell & Howell Information and Learning
300 North Zeeb Road, Ann Arbor, MI 48106-1346 USA

UMI®
800-521-0600

# Experimental and Theoretical Investigation of the Curing Process of Thermosetting Composite Structures with Angle–Bend.

Malak Naji

A Thesis

in

The Department

of

Mechanical Engineering

Presented in Partial Fulfillment of the Requirements

for the Degree of Doctor Of Philosophy at

Concordia University

Montréal, Québec, Canada

September 1998

# ABSTRACT

Experimental and Theoretical Investigation of the Curing Process of Thermosetting Composite Structures with Angle–Bend.

Malak Naji, Ph.D.
Concordia University, 1998

The effect of existing cure cycles and processes on the quality of thermoset composite parts with angle–bend is presented. A 2–D finite difference scheme was developed to model the processing of arbitrary shaped composite parts. The formulation includes heat transfer, viscosity, extent of cure, and resin flow submodels. Matrix material properties were allowed to vary with temperature. As a result, various cure parameters such as temperature, degree of cure, viscosity, compaction and fiber volume fraction were examined.

A first set of experiments was done to investigate the effect of different curing cycles on temperature exotherms, thickness variation and fiber volume fraction distribution. Results from both simulation and experiment agree well. They also showed that parts produced using recommended curing cycles from manufacturers were not of good quality in terms of uniform fiber volume fraction and thickness over the cross–section of the part.

Based on these results, an optimal curing process was obtained. An optimal curing process is defined as one which will produce uniform thickness and fiber volume fraction throughout the composite part including straight sections and

curved sections. This process was applied to curved laminates consisting of 50 layers graphite/epoxy Hercules AS4/3501-6. Results obtained from simulation and experiment were compared. Good parts were obtained.

# ACKNOWLEDGEMENTS

I would like to express my deep gratitude to my advisor Professor Suong V. Hoa for his technical input and for his friendship throughout my graduate career. I feel very fortunate to have worked with Dr. Hoa and look forward to many more years of interaction.

The financial support provided by the Canadian International Development Agency (CIDA) and by my supervisor is greatly acknowledged.

This work would not have been possible without the help of numerous individuals. I would like to thank Mr. J. Elliot, Mr. P. Ouellette, Mr. J. Sarruf, Mr. G. Seeger and all the people who helped me in the experimental setup. I am also grateful for the support of my Ph. D. friends: Alata and Molhim. The support of the people at the Concordia Center for Composites was indispensable.

Also, I wish to thank Professor Mohamad Alnimr and Professor Taha Aldoss of Jordan University of Science and Technology (JUST), Jordan, for encouraging and helping me to get the CIDA Scolership and pursue my Ph. D. in Canada.

I am very grateful to my Parents for their love, support, and encouragement to achieve my educational goals.

Last, but not least, my special thanks to my husband Samer, whose love, invaluable support, patience and understanding made the course of this work possible and successful. Off course, the playful, sometimes distracting, times offered by my kids Rafeef and Ziad should not go without mention.

# TABLE OF CONTENTS

# LIST OF FIGURES

# LIST OF TABLES

# LIST OF SYMBOLS

| | |
|---|---|
| e' | Permittivity |
| e" | Loss factor |
| $\sigma$ | Ionic conductivity |
| $x - z$ | Laminate global direction |
| $1 - 3$ | Ply principal direction |
| $\xi - \eta$ | Computational coordinates |
| $T$ | Temperature |
| $T_s$ | Surface Temperature |
| $T_a$ | Autoclave Temperature |
| $k_f$ | Fiber thermal conductivity |
| $k_r$ | Resin thermal conductivity |
| $k_{xx}, k_{zz}, k_{xz}$ | Laminate effective thermal conductivity |
| $k_{11}, k_{33}, k_{13}$ | Ply effective thermal conductivity (principal direction) |
| $t$ | Time |
| $\dot{q}$ | Internal heat generation |
| $\rho$ | Composite density |
| $\rho_f$ | Fiber density |
| $\rho_r$ | Resin density |
| $c_p$ | Composite specific heat |
| $c_{pf}$ | Fiber specific heat |
| $c_{pr}$ | Resin specific heat |
| $v_f$ | Fiber volume fraction |
| $v_r$ | Resin volume fraction |

| | |
|---|---|
| $r_f$ | Fiber radius |
| $S_f$ | Fiber permeability |
| $S_r$ | Resin permeability |
| $S_{xx}, S_{zz}, S_{xz}$ | Laminate effective specific permeability (global direction) |
| $S_{11}, S_{33}, S_{13}$ | Ply effective specific permeability (principal direction) |
| $m$ | $=cos(\theta)$ |
| $n$ | $=sin(\theta)$ |
| $\theta$ | Rotation angle |
| $P$ | Resin pressure |
| $P_{min}$ | Minimum resin pressure |
| $P_f$ | Fiber pressure |
| $P_a$ | Autoclave pressure |
| $P_g$ | Bag pressure |
| $(RH)_o$ | Relative humidity |
| $\mu$ | Resin viscosity |
| $m_v$ | Coefficient of volume change |
| $\alpha$ | Degree of cure |
| $\frac{dH}{dt}$ | Rate of heat flow |
| $\frac{d\alpha}{dt}$ | Rate of cure |
| $H_R$ | Total heat of reaction |
| $A_1, A_2, A_3$ | Pre–exponential factors |
| $E_1, E_2, E_3$ | Activation energies |
| $U$ | Activation energy |
| $R$ | Universal gas constant |
| $K_\mu$ | Viscosity constant |

| | |
|---|---|
| $\kappa$ | Kozeny constant |
| $D$ | Domain boundary |
| $\hat{n}$ | Outward unit normal to the domain surface |
| $h$ | Convective heat transfer coefficient |
| $(\frac{h}{k})_{eff}$ | Effective heat transfer coefficient |
| $(F_c)_{eff}$ | Effective flow coefficient defined in equation 2.15 |
| $\wp, \beta, \gamma$ | Coefficients in the domain transformed equation |
| $e$ | Void ratio |
| $u_{i,j}, v_{i,j}$ | Pseudo–temperature/pressuresolutions |
| $\phi$ | An angle defined in figure 4.4 |
| $l$ | A non-dimensional scale defined in figure 4.4 |
| $LC$ | Logarithm of ionic conductivity |

# Chapter 1

# Introduction

## 1.1 Overview

Due to their high specific strength and stiffness, fiber reinforced plastic materials are firmly established in products ranging from aerospace structures to sporting equipment. Examples of the former include primary and secondary aircraft structures, while the latter includes products such as swimming pools, bicycles, windsurfers and ski-boat hulls. A large percentage of high performance composite parts and structures are constructed from thermosetting resins and continuous fibers and processed through autoclave curing.

Processing converts the ingredients of a product into its designed shape. In the case of composites, processing may alter fiber organization and morphology of the material. The service performance of a composite structure calls for three interactions: material, design and processing. The ultimate service performance of a composite structure will reflect the extent to which the inherent properties of

the product form and design are translated by the conversion processes into an end product.

The ultimate objectives of processing science are threefold: to be able to predict how a material will behave in a known manufacturing operation; to learn how to tailor a material product form so that it can be processed easily; and to devise novel conversion processes to achieve desired end products. The two approaches to these goals are analytical and experimental. The analytical approach to processing must separately address three areas of materials science: chemical change, thermophysical properties, and deformation characterization [1].

The method of processing has a large impact on the properties and quality of composites. There is no one single manufacturing technique that is perfect for every composite part, but improvements are always being made to the manufacturing processes. The evolution of the manufacturing methods for composites tends to favor techniques to produce materials that minimize their defects. It is desirable to establish at an early stage if, and how, chemical changes may occur during processing. Heat exchange, and the thermodynamic properties associated with such temperature changes, play an important role in defining process economics. Uneven temperature profiles resulting from process dynamics can be a cause of non-uniform deformation or failure to conform to shape in the desired manner [1]. They can also cause internal stress in the composite.

Processing concerns associated with thermosetting composites become increasingly important for components of appreciable thickness. In the aerospace industry,

a thick laminate may approach 13 mm (1/2 inch) or more, while for construction and military applications thick laminates can exceed 0.15 m (1/2 ft) in thickness [2]. Perhaps the most familiar concern is an increase in internal temperature resulting from the irreversible exothermic chemical reaction of the matrix phase. Also, the gradients in temperature and degree of cure induce non-uniform curing within the part.

Hence, it is desired to gain a fundamental understanding of the curing process unique to thick angle-bend thermosetting composites parts. This is because gradients in temperature and degree of cure are strongly dependent on part geometry, thermal anisotropy, the chemical cure kinetics and the thermal boundary conditions (curing cycle and tooling).

## 1.2 Thick Composite Processing

Since their introduction as structural materials, composites have primarily been used for thin, laminated plates or shells. This is characteristic of their use in the aerospace industry, where extreme value is placed on weight savings.

The next evolutionary step for composites is to applications that require thick sections. Thick composites could be used for lightweight submarines or ship hulls. Also, an increased emphasis on civilian infrastructure has given new life to the use of composites for bridge decking, pylons, I-beams, etc.. Many of the applications require material thickness that far exceed the capabilities of existing manufacturing

processes. Compared to the strong attention that has been directed at modeling and simulating various aspects of the curing of thin composite parts, there has been somewhat less attention paid to comprehensive models targeting thick parts and to the inherent difficulties of manufacturing a thick-section polymer composite [2, 3]. Improved technologies are needed to support the growing interest in thick composite applications.

There are several inherent difficulties in the manufacture of thick thermosetting polymer composites. Their low thermal conductivity across the thickness presents a large thermal barrier during heat-up and cool down. During a typical cure cycle the interior temperature of a thick section may lag far behind the surface temperature, causing the surface regions to cure more quickly. If they cure too quickly and gel before the interior is consolidated, the excess resin in the interior is trapped. This leads to non-uniform fiber volume distribution and excessive void growth in the resin-rich interior. In order to efficiently manufacture quality parts, on-line control and process optimization are necessary, which in turn require a realistic model of the entire process.

Perhaps the most detrimental behavior observed during thick composite processing is thermal spiking. As the interior heats up, the exothermic curing reaction is initiated and releases energy. This heat is essentially trapped in the interior due to poor thermal conductivity. The entrapped heat raises the temperature of the interior even further, promoting faster curing and more rapid energy release. The process can quickly become unstable, producing a thermal spike. Peak temperatures during

a thermal spike are quite high and can easily lead to matrix degradation [2, 3, 4, 5, 6]. Very slow heat up rates and several intermediate dwells are sometimes used to control thermal spiking. Such cure methods lengthen the processing time and increase the manufacturing cost.

## 1.3 Processing Composite Parts With Angle–Bend

The problem of curing thick thermoset composites is complicated and considerable work has been done to address this problem [2, 3, 5, 6, 7, 8]. Further complications arise when a bend is introduced to the section. Curved section composite structures appear in many applications such as flanges in pipes or pressure vessels, L -shaped hangers, U-shaped sections, T sections, etc. Issues to be addressed are:

- The curve included in these structures enhances fibers displacement where transverse resin flows occur. Transverse flow results in changes in bend thickness and hence in fiber volume fraction (resin–rich areas). The photo in Figure 1.1 shows a cross–section made in a curved laminate with a resin–rich area, and Figure 1.2 shows the variation in thickness between the bend and the straight edges.

- Non-uniform curing process (which is unique to thick sections) leads to gradients in degree of cure in both thickness and length directions due to the geometry of the part. This influences the quality and in-service performance of the finished part by inducing warpage and residual stress during the curing

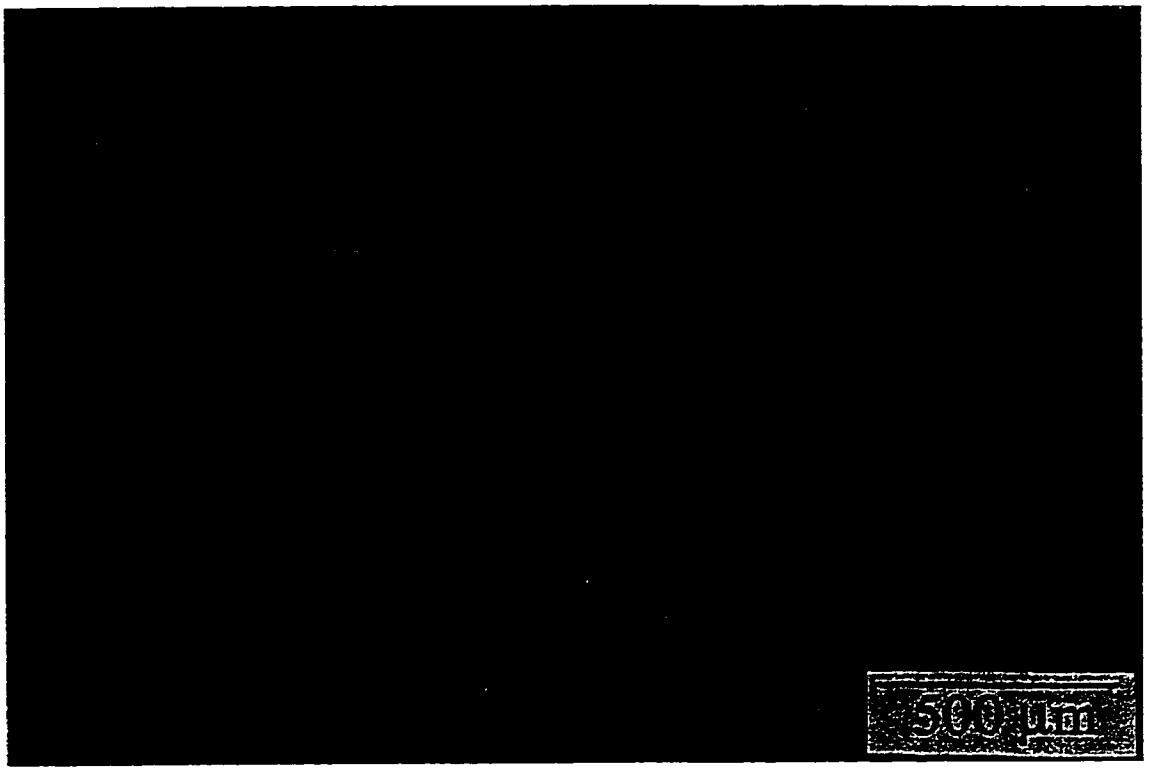


Figure 1.1: Resin–rich areas in a part processed using a conventional curing process (150X).

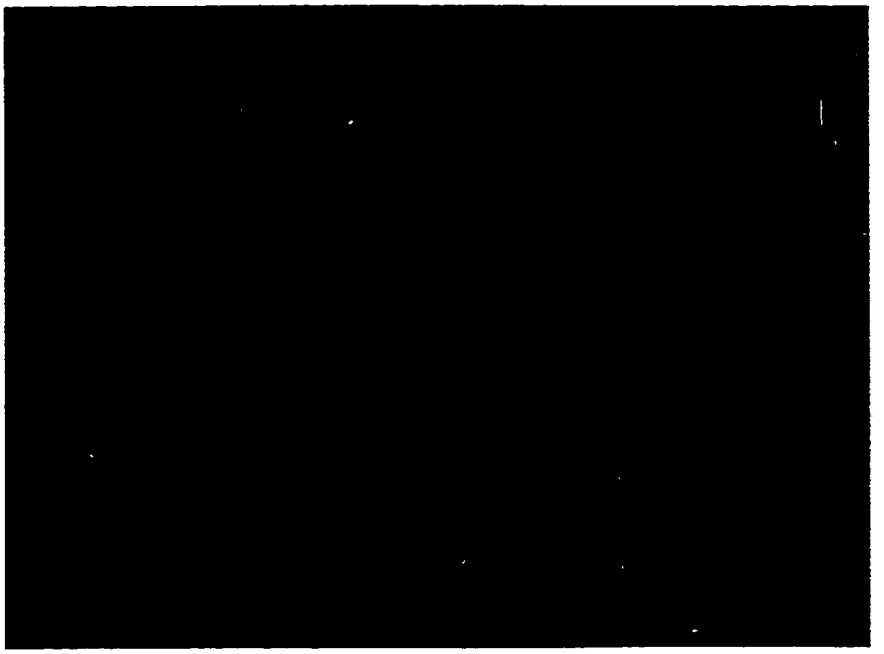

Figure 1.2: Thickness variation between the bend and the straight edges present in curved laminates.

process.

- Dimensional changes (which result from the anisotropic properties of the composite part) lead to a phenomenon called 'Spring In' which is a problem present in sharply curved (90°) thick laminates. A sketch showing this phenomenon is shown in Figure 1.3.

Since those mentioned problems affect the integrity of the structure and hence lead to a low quality part, and there has been very limited work in this area, the processing of thick angle-bend structures will be studied.

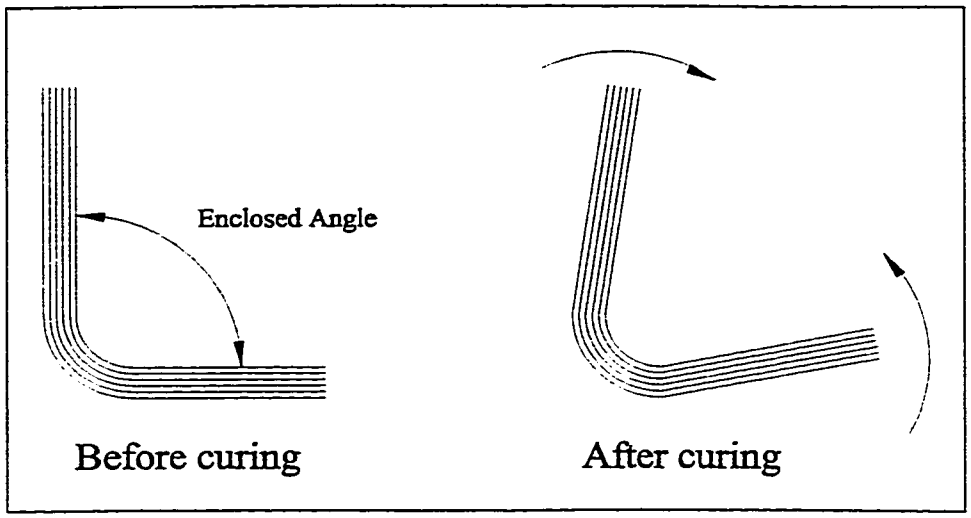


Figure 1.3: Thermal distortion induced in an angle–bend composite part.

## 1.4 The Autoclave Cure Process

The processing of composite laminates having a thermosetting resin matrix is a complex process. It involves simultaneous heat, mass, and momentum transfer along with chemical reaction in a multi phase system with time–dependent material properties and boundary conditions. This is normally accomplished through press cure, autoclave cure, or oven cure. In the case of a press or autoclave cure, temperature and pressure are supplied by the equipment. In an oven cure, heat is supplied by the oven, but pressure must come from another source, typically, a vacuum bag, mandrel expansion, shrink film, expandable rubber, or mechanical clamps.

For epoxies, cure refers to the chemical reaction of an epoxide group in the resin component of the matrix with either an amine or anhydride hardener. The reaction is exothermic in nature, and results in increased molecular weight of the matrix, which is a function of the extent of the curing reaction. The measured

viscosity is related to the size of the molecules present. As the resin and hardener molecules react, larger molecules are formed, resulting in a significant increase in viscosity at moderate temperatures.

An often used production procedure for fabricating a high performance structural laminate is the Autoclave/Vacuum Degassing laminating process. An autoclave is a pressure vessel that operates under controlled temperature and pressure. The vessel, shaped like a cylindrical shell, usually has two door assemblies, utility and instrumentation penetrations, and vessel support. Vessel internals include insulation, sheet metal shroud, ductwork, and electrical heater assembly. Others may also include blower drive assembly and cooling coils. The autoclave is an ideal method for composites that require continuous reinforcement and complex contours.

The curing process has a very large impact on the properties of a composite part. Improvements on composite cure cycle can enhance fabrication time, operational cost and quality of the end product. Autoclaves are designed to produce high quality, reliable parts. In the autoclave process, precut pieces of collimated fibers impregnated with uncured thermosetting resin (prepregs) are laid up on a smooth tool surface in a certain order, orientation and ply count to produce the desired properties in the part. For thick parts, it is often necessary to interrupt the lay–up process at intervals for bulk reduction and consolidation [9]. This consists of placing the partial lay–up in a vacuum bag and heating it to reduce thickness. The vacuum bag is then removed and the lay–up procedure continues. Once the lay–up is complete, resin dams may be placed around it to help control resin flow. Bleeder

material may also be added to absorb extra resin and to help provide a clear path for the volatiles to escape through the vacuum system [9]. The entire composite lay–up assembly is then enclosed in a vacuum bag and sealed. A schematic of the lay–up is shown in Figure 1.4

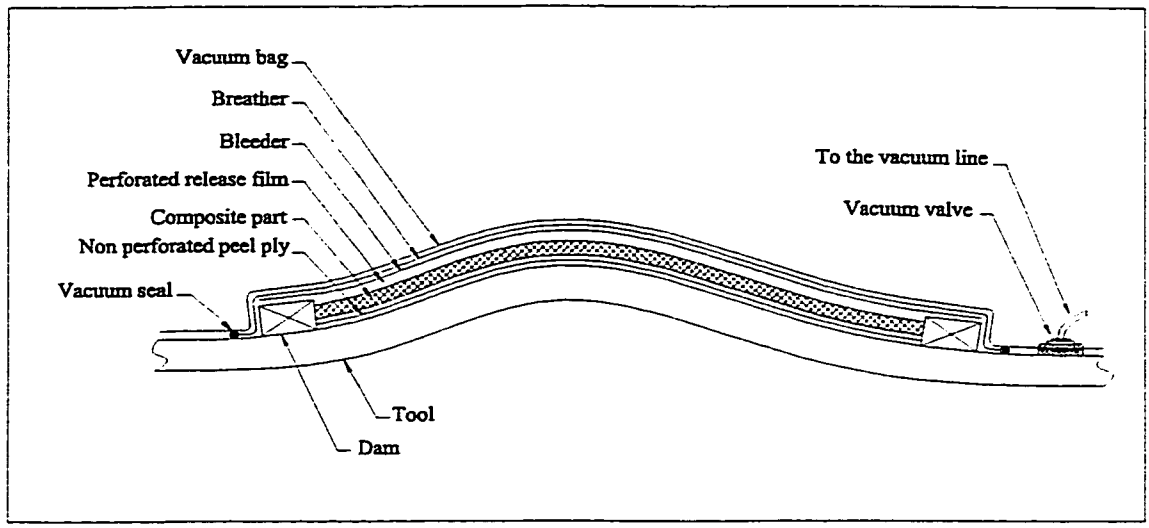


Figure 1.4: Typical autoclave lay–up

After composite part has been shaped from a mixture of uncured resin and fibers and bagged, the curing process is accomplished by moving the entire tool into an autoclave. Heat and pressure is then applied to the laminate according to a given cure cycle. Usually, vacuum is initially applied to the bag while the autoclave temperature and pressure are raised.

Heat lowers the viscosity of the resin but also activates the irreversible chemical cross-linking reactions, which again tend to increase the resin viscosity. These two opposing phenomena mean that a limited time exists during which flow and consolidation can take place. By application of the curing pressure, the excess resin

and air trapped between the plies is squeezed out. Resin flow can occur, initially, both vertically (thickness direction) and horizontally. Furthermore the network of fibers can eventually act as a network of springs to which the vacuum bag and bleeder assembly transfer the load from the autoclave pressure [10]. This load can be transferred through the fiber network to the tool surface with only a slight frictional loss. As the fiber spring network is loaded and compressed more resin flow occurs; however, at this point the resin viscosity is increasing and the permeability is decreasing making resin flow more difficult . Through this consolidation process the fiber volume fraction is increased and made more uniform, leading to improved mechanical properties.

During the cure cycle, the process must meet the following requirements to produce a structurally acceptable part:

- Void elimination: Many prepregs contain a considerable amount of air and moisture that might be a result of manufacturing, storing or stacking. Thus, the curing process must prevent unacceptable porosity levels from these sources by compressing the entrapped air and preventing boiling of water.

- Solvent removal: The solvent will create voids and affect final performance of the part if it remains in the composite. Fortunately, the solvents used for epoxy resins have a low boiling point and evaporate during lay–up.

- Fiber wet-out: A low resin viscosity during cure aids fiber wet-out and reduces the porosity in a cured part.

- Consolidation: The combination of low resin viscosity and pressure decreases the thickness of prepreg materials.

- Resin removal: By taking advantage of the viscosity change during the cure cycle, the excess resin can be removed.

These five items emphasize the criticality of understanding the rheological properties of the resin. These properties can now be studied in the laboratory and then applied to the specific curing process selected for composite manufacture. This technology has only been available since 1978, and many older curing processes are being revised.

The quality of the laminate product is measured in terms of void content, resin content, fiber distribution, extent of cure, and the uniform laminate thickness. These product qualities are difficult to control because of the strong interactions between the effects of autoclave temperature, autoclave pressure, heat of reaction, and the geometry of the part being manufactured. Cure cycle optimization must be done to enhance product qualities [11, 12].

There is an infinite number of combinations of pressure, temperature and time (cure cycles) that can be used to try to achieve this goal. Because of the complexity of the curing process, the composites industry relies to a great extent on cure cycles supplied by material manufacturers. However because the supplier does not have available information on the specific tooling arrangements which will be used, or of the geometry of the parts to be produced, these cycles are in most cases unnecessarily

conservative and costly. It has also been observed in the literature [4, 13] that some commercial cure cycles can result in incomplete ply compacting leading to significant strength and stiffness variations in the laminate.

Industrial practice is to generate a cure cycle through trial and error combined with past experience. Figure 1.5 shows one such standard cure cycle employed for carbon/epoxy composites. There are many key decision variables in the cure cycle including time at which to elevate the temperature and pressure, to what extent they should be raised, and how long the part should be exposed to the conditions. Also, other variables, such as, the ramp rate of temperature and the first and second hold temperatures and times can also influence the product quality. Variations in the properties of the raw materials and the geometry of the part being manufactured will require modifications to the standard cure cycle.

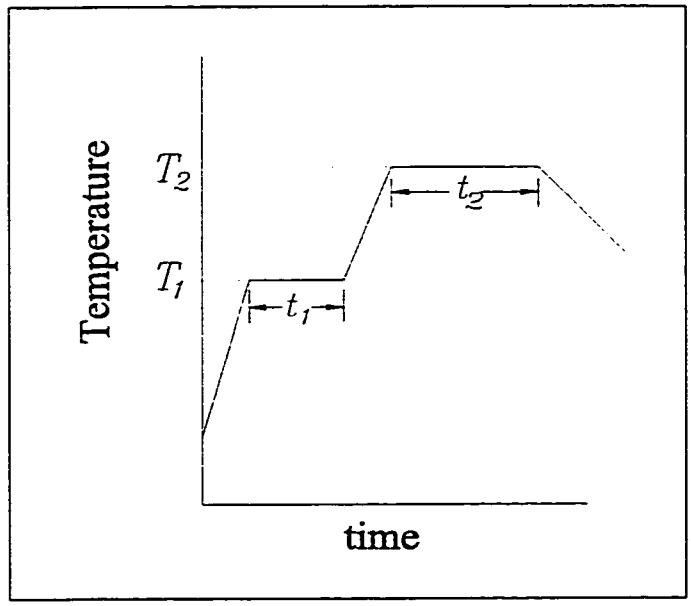


Figure 1.5: Schematic of a standard 2–step cure cycle.

The importance of controlling the cure cycle cannot be underestimated. The process variables must be controlled so that the volatiles are suppressed during processing to provide a void free matrix. If the heating rate is too low, the minimum value of the resin viscosity is increased. This results in obstructed resin flow. Thermal overshoot and uneven heating produce a part that contains thermal stresses, resin rich regions, and void zones. The pressure value and its application point are also important to the product quality. When the pressure is applied at minimum viscosity, it must be above a certain value in order to prevent delaminations. However, when the pressure is applied at a higher viscosity, the result is a higher void content. The pressure in the resin must also be taken into consideration. If it drops to zero too rapidly, void growth during consolidation is favored [4, 12].

The best way to determine an appropriate cure cycle for a desired application is through the use of models. Models are used to simulate the cure process which can then be used to define the cure parameters. Some of the latest research involves modeling the entire consolidation process in order to find the optimal cure cycle. The analysis of the consolidation model results in predicted values of pressure, resin velocity, and laminate thickness throughout the consolidation process. This information can then be used to design the optimal cure cycle.

Computer simulation provides a powerful tool with which cost effective cure cycles producing high quality laminates can be designed. This is mainly because a number of different processing techniques, operating conditions and tooling arrangements can be investigated quickly and inexpensively with the aid of a personal

computer. Currently, research is heading toward the automatic computer control of curing processes through the use of dielectric sensors. Dielectric analysis measures the capacitance and conductance of a material, which can be correlated to molecular activity. Such correlation allows the scientist to probe the chemistry, rheology, and molecular mobility of the polymeric materials.

The future of autoclave processing relies on the ability to have precise control over the curing process. The quality of autoclave cured composite parts will greatly improve when the curing process can be precisely tailored for each specific application.

## 1.5 Dielectrometry

### 1.5.1 Dielectric Monitoring

Recently, efforts have been made to *insitu* monitor the curing process of thermoset composite materials. Cure characterization based on dielectric spectrometry was investigated as a non–destructive technique in References [14, 15, 16, 17, 18, 19, 20]. Correlating dielectric response and material rheological properties was the subject of References [21, 22, 23, 24]. Also, relaxation behavior of thermoset resins was studied in References [25] and [26].

Several sensors have been developed to withstand the severe environments found in production presses and autoclaves. Out of these sensors, dielectric sensing is considered to be the most promising technique for monitoring and controlling

composite curing processes [27]. The dielectric technique consists of three major steps [28]:

1. Measurement of a signal related to some dielectric property of the material.

2. Conversion of the measured signal to the actual value of the dielectric property.

3. Conversion of the experimentally determined dielectric property to the viscosity and degree of cure of the material.

The first two steps are well in hand and can be obtained directly from the dielectric instrument itself. Regarding the third step, many correlations were made to convert some dielectric properties to the viscosity and degree of cure of the material.

### 1.5.2 Dielectric Theory

Dielectric measures two fundamental electrical characteristics of a material: Capacitance and Conductance, as a function of time, temperature and frequency. The capacitive nature of a material is its ability to store electric charge, and the conductive nature is its ability to transfer electric charge. While these electrical properties are important in themselves, they have been more significant when they are correlated to molecular activity. Such correlation allows the scientist to probe the chemistry, rheology (flow) and molecular mobility (relaxation) of the polymeric materials.

Some uses of dielectric analysis include: Resin flow and cure, Time required to reach full cure, Relative degree of cure, Off-line material processing information, Storage stability information, Change in properties due to exposure to environment

(oxidation, thermal breakdown), and many more. In dielectric analysis, a sinusoidal voltage is applied to a sample placed between two gold electrodes to create an alternating electric field. This produces polarization in the sample, which oscillates at the same frequency as the electric field but has a phase angle shift. This phase angle shift is measured by comparing the applied voltage to the measured current which is separated into capacitive and conductive components.

The current can be measured by a low-impedance current meter or by using the current to charge a load capacitor and then measuring the voltage across the capacitor. Measurements of capacitance and conductance are used to calculate the following variables, which provide valuable information about molecular motion:

e' = permittivity, which is proportional to capacitance;

e" = loss factor, which is proportional to conductance;

$tan\delta$ = dissipation factor, which equals e"/e';

$\sigma$ = ionic conductivity, which is derived from measurement of e" [1].

These are the characteristic parameters that describe the polarization of a dielectric material by dipole orientation in an applied electric field. A dipole is a chemical bond that has an unbalanced distribution of charge in a molecule. One part is partially negative and the other partially positive. Permanent dipoles exist in the absence of an applied electrical field, and are caused by the differences in

[1] $\sigma = 2\pi f e" e_0$ where $f$ is the frequency and $e_0$ is the absolute permittivity of free space ($8.85 \times 10^{-12} F/m$).

electronegativity of the bonded atoms (e.g., carbonyl bond C=O, C–N). Induced dipoles are those created by the applied electrical field, which causes redistribution of electrons shared between bonded atoms with similar electronegativity. Permittivity e' and loss factor e" both provide valuable information about molecular motion. e' measures the alignment of dipoles, while e" represents the energy required to align dipoles and move ions.

## 1.6 Literature Survey

Numerous studies have been directed at the modeling and simulation of various aspects of the consolidation and cure of thin composite parts. Studies of the curing process have focused on the thermal and chemical interactions, degree of cure profiles, viscosity behavior, void formation and growth, and resin flow phenomena occurring in the composite under the application of a specified temperature and pressure cure cycle history.

### 1.6.1 Thick Composites

#### Modeling and Simulation

Loos and Springer [4] developed a comprehensive one-dimensional simulation model to describe the curing process of flat plate unidirectional graphite/epoxy composite laminates. The model integrated submodels which describe the fundamental mechanisms associated with the curing process, such as, the thermochemical interactions,

resin flow, and void formation. Governing equations describing the curing process were solved with an implicit finite difference method. Temperature, degree of cure, resin flow and void size, among other processing variables were predicted as a function of the autoclave pressure and temperature cure cycle history. Experimental verification of the model was performed and results were in good agreement with simulated predictions.

Kays [7] conducted a comprehensive investigation on the processing issues unique to large area thick section laminates. The baseline material system was unidirectional graphite/epoxy. Cure simulation models were developed and used in the investigation. Various autoclave procedures, cure monitoring and non-destructive evaluation techniques for thick section laminates were developed and evaluated. Contributions towards the development of a generic methodology for processing thick section laminates were made. Interesting observations reported in the study were the development of microcracks and delamination under certain processing conditions, indicating the importance of processing on the cure and performance of thick section composites.

Twardowski et al. [2] developed a simulation that recovers much of the thermal behavior of a 5 cm thick, unidirectional graphite/epoxy charge, cured in a one-dimensional manner. An experiment was designed which is capable of testing simulation results. The following results were found: initial extent of reaction is relatively unimportant; consolidation is important; the peak temperature originates

near the surface of the laminate and propagates to the center; asymmetric temperature application changes the viscosity and cure profiles; viscosity never reaches low values simultaneously through the thickness in laminates in excess of 10 cm thickness.

Bogetti and Gillespie [5] conducted a fundamental study of process-induced residual stress in the thick-section thermosetting composites. A one-dimensional cure simulation model was employed. Residual stresses were shown to be strongly influenced by gradients in temperature and degree of cure. In another investigation [3], they proposed a two-dimensional cure simulation for thick thermosetting composites.

Hojjati [6] developed a one-dimensional through-the-thickness and a two-dimensional simulations for thick thermosetting structures. Heat conduction, kinetic, viscosity, and flow equations were solved as a coupled system of equations. Experimental results for temperature history and compaction were compared with simulation results and good agreement was obtained. He found that pre-bleeding technique is the most promising method for fabrication of thick composites.

Tredoux and Westhuizen [29] developed a 2–D finite element numerical code that simulates combined heat transfer, resin flow, and compaction during composites processing. The autoclave cure of a flat unidirectional 256–ply carbon/epoxy laminate was modeled. Results showed the variation in temperature, degree of cure, and fiber volume fraction along the horizontal and vertical midplanes of the laminate.

### Cure Process Development

Researchers have worked on the development and optimization of curing cycles associated with autoclave processing of thick laminates. Hjellming and Walker [8] considered cylinders with 0.15 m and 0.30 m thick made of graphite fibers and thermoset resin. They showed that it is possible to achieve: (1) a consolidation period with a viscosity which is everywhere relatively low for a reasonable period of time, and (2) a complete cure with the temperature never exceeding 180° C. The different results obtained illustrated that there is no simple scaling law for thickness.

Joseph et al. [30] used a feedback control strategy for autoclave curing of carbon/epoxy composites. They demonstrated that neural network can be used to control the laminate thickness and maximum void size by applying a higher pressure earlier during the process and by significantly lowering the cure temperatures used.

Chang et al. [31] applied genetic algorithm to design a cure cycle for the consolidation of thick laminated composites. They obtained an optimized cure cycle that results in a shorter cycle time for the process while avoiding the thermal runaway inside the composites.

Shim et al. [32] studied void generation in composite structures caused by different lay–up techniques, such us varying the vacuum pressure. They showed that lower void content was produced when full vacuum with a moderate autoclave pressure (170 KPa) were applied.

Kim and Lee [33] developed an autoclave cure cycle to reduce the temperature

overshoot in thick composite laminates. They simulated the curing process and used the results to modify the cure cycle through steps of cooling and reheating. The developed cure cycle was tested on 15 and 30 mm thick laminates and was found to be effective in reducing temperature overshoot.

### 1.6.2 Thick Composite Structures with Angle–Bend

In their work, Bogetti and Gillespie [3] dealt with a thermoset angle-bend structural composites. Only temperature and degree of cure distributions within the cross-section were predicted as a function of the autoclave temperature history. They provided insight into the non-uniform curing process unique to thick-sections. The spatial gradients in degree of cure directly influence the quality and in-service performance of the finished component by inducing warpage and residual stress during the curing process.

Furthermore, Gilmore and Guceri [34] developed a numerical approach to analyze the processing of thermoplastic–matrix composites of complex geometry's including angle-bend structures. In both studies [3] and [34], the boundary-fitted coordinate system transformation technique was combined with a finite difference method to determine the temperature distribution within the part.

Johnston et al. [35] developed a 2–D finite element process model for laminated composite structures. Their model allowed for the analysis of heat transfer, cure kinetics, resin flow, and residual stresses and deformations in complex geometries. They studied a symmetric 24 ply quasi–isotropic $[0/+45/-45/90]_{3s}$ composite

angle part processed on a solid, square aluminum tool. The composite material properties used were typical of a second generation carbon–fiber toughened–epoxy resin material. Their results showed that process tooling affected the overall process cycle time and, more important, the part thermal behavior where non–symmetric temperature and degree of cure gradients were obtained through the part thickness. Also, resin flow was shown to be uneven resulting in non–uniform resin distribution throughout the part and uneven part thickness. Figure 1.6 shows their simulation output of the curved part at the end of processing, which shows the fiber volume fraction to be nonuniform. In their work, springback angle was predicted and found to be influenced by two factors: choice of tool material, and surface friction condition.

### 1.6.3 Dielectric Measurements

Kenny et al. [36] developed and tested a chemorheological model for a commercial carbon fiber/epoxy prepreg. Predictions of the viscosity changes during prepreg cure qualitatively agreed with dielectric measurements of the inverse of the ionic conductivity in the epoxy matrix. In particular, predicted and measured times at which minimum viscosity occurred showed excellent agreement, even for complicated cure cycles.

Ciriscioli et al. [37] performed tests measuring the temperature, ionic conductivity, and compaction in 16 to 200 ply thick graphite/epoxy laminates. They used the dielectric measurements to gather some information regarding the validity of the

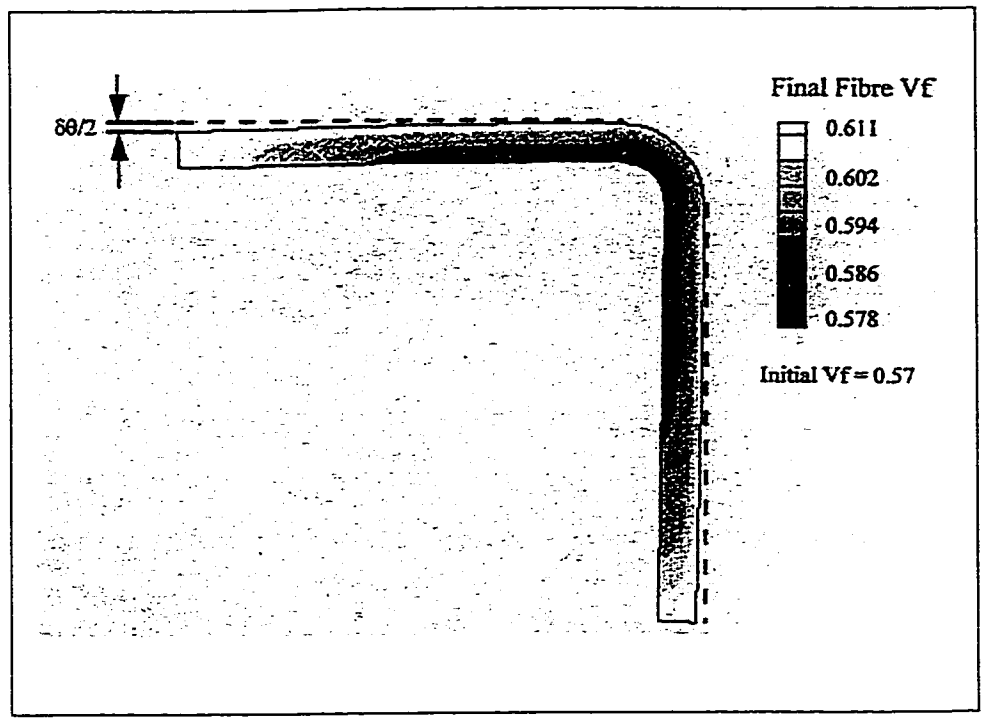


Figure 1.6: Fiber volume fraction distribution at the end of processing obtained from simulation results [35].

Loos-Springer CURE model [4]. A modified ionic conductivity (that exhibits similar trends as the viscosity) was calculated and plotted versus time. The plots show that the calculated viscosity reaches a minimum at the same time as the measured modified ionic conductivity, and the calculated rate of degree of cure becomes zero at about the same time as the measured rate of modified ionic conductivity.

Day [27] monitored the dielectric properties of AS4/3501–6 graphite epoxy during several different curing cycles. He found that the measured dielectric viscosity (inverse of ionic conductivity) was correlated well with predicted viscosity. Also, he calculated the dielectric cure index using the data obtained from the temperature dependence of the ionic conductivity for un–cured and cured material. The results

were compared to the degree of cure from model predictions and found to exhibit similar shapes.

Kim and Lee [38] calculated the degree of cure from a modified dissipation factor D*, that has the value between 0 and 1. D* predicted well the degree of cure of the carbon fiber epoxy materials under various temperature profiles. Also, comparing the derivative of the dissipation factor with respect to time $dD/dt$ and the isothermal degree of cure, they found that the cure started at the point of maximum $dD/dt$ and the cure ended at the point of zero $dD/dt$.

Maffezzoli and et al. [39] presented a method for the complete thermal, rheological and dielectric characterization of an epoxy matrix. The ionic resistivity and degree of reaction data were correlated during the cure of the epoxy matrix and good agreement between the model predictions and the experimental data was observed under isothermal and non–isothermal conditions. Moreover, degree of reaction data calculated from dielectric measurements was used in a chemorheological model for viscosity calculation, to obtain very good correlation between measured and predicted values.

## 1.7 Need for Research

Many laminated composite structures, such as a flange, an angle bracket, a co–cured web, or a frame have a loaded curved portion. The final failure in such structures may be a complex progression of ply cracking, delamination, and fiber failure. More

recently, efforts at measuring interlaminar tensile strength have been focused on the curved–beam test methods (C–shaped and L–shaped), because of the difficulties in introducing loading onto the flatwise specimens.

Because curved thick laminates (especially with small curvature) are very difficult to manufacture with consistent quality [40], semicircular specimens are of poor quality with a high void content and thickness variations. Furthermore, interlaminar strength is degraded by manufacturing and processing defects such as porosities, resin pockets, and resin–rich interlayers. As composite components increase in complexity, there is a higher possibility of porosity existing in the structure. It is well known [41, 42] that porosities in composites, either artificially induced or processing caused, can result in significant reduction in structural strength and life. A number of papers have been published on the experimental determination of the interlaminar tensile strength following the L–beam test method:

- Martin [43] investigated the delamination failure in a 24–ply AS4/3501-6 unidirectional curved laminate. The laminates "were cured according to the material manufacturer's instructions". Nothing was mentioned about the quality of the laminates except that $v_f$ in the curved region was less than that in the leg (2.6%).

- Jackson and Martin [44] conducted experiments to determine the interlaminar tensile strength for different AS4/3501-6 unidirectional curved laminates. They mentioned that they used a "thermal blanket on the 48–ply specimens

to ensure uniform heating" and that debulking was done every four plies. The quality of the laminates was highest in the inner half of the thickness where $v_f$ "was observed to vary through the thickness.

- Martin and Jackson [45] worked on damage prediction in cross–plied curved laminates. Nothing was mentioned about the quality of the laminates except that "the specimens had an average $v_f$ in the curved region of 54.7%.

- Jackson and Ifju [46] examined different laminates to determine their through the thickness tensile strength. Unidirectional tape laminates were made with 24– and 48–ply AS4/3501-6. "One side of the specimen was against a male tool and the other side was bagged". They noticed that "in several panels, the curved region was slightly thicker than the loading arms".

- Researchers in references [47, 48] fabricated 16–, 24– and 32–ply AS4/3501-6 unidirectional curved laminates for interlaminar tension tests. They found that the poor quality of the 32–ply laminates compared to the other laminates contributed to the nonlinear response in load–displacement curve. "Ply crimps and waviness were almost unavoidable after molding about 25 plies for the 32–ply laminate and, hence, contributed to the development of resin–rich pockets".

Curing thick laminates by the conventional cure cycle leads to temperature overshoot at the center of the laminate during the exothermic reaction. This overshoot can lead to matrix degradation and thermal residual stress. Furthermore, as

was mentioned before, the variation in thickness and fiber volume fraction through a curved laminate leads to poor quality specimens. Hence, a cure process which can reduce temperature overshoot and produce a curved laminate with minimum thickness and fiber volume fraction variation is necessary for processing thick angle–bend laminates.

## 1.8 Thesis Outline

In Chapter 2, the two–dimensional models that govern the curing process are constructed along with boundary conditions. These models account for thermochemical interactions from which temperature, degree of cure and viscosity are predicted, as well as resin flow which includes pressure, fiber volume fraction and compaction predictions. Numerical solution of the governing equations is the subject of chapter 3 in which the material system and models are defined. To verify the simulation model results, experiments were made and results are presented and compared in Chapter 4. Based on these results, modifications were made on the curing process (including the cure cycle) and a modified cure process was presented and tested in chapter 5. Chapter 6 summarizes the significance, findings and contributions of the present work, and recommends several areas for future study and development. Much of the mathematical development along with instrumental and experimental data has been put into appendices so as not to distract the reader.

# Chapter 2

# Process Modeling

## 2.1 Background

Modeling usually consists of representing the process under consideration by mathematical equations and then solving them numerically on a computer in order to predict behavior. Although models have limitations, they can be used for quick, cost-effective investigation of a variety of similar situations and can optimize a given process. Models should be used not only in the development of a process but also as part of the process control package on the manufacturing level.

The history of process modeling is relatively short. Most previous applications of mathematical modeling have been in the fields of heat transfer, fluid flow, and mechanics. Examples include predicting heat flow through complex shapes or sophisticated re-entry thermal protection materials, investigating boundary layer and aerodynamic flow systems, and estimating the stresses in materials under load. The actual computer programs have often been quite large and sophisticated, requiring

trained specialists and mainframe computers. These factors have tended to discourage most manufacturing engineers from even exploring the modeling approach. This will rapidly change as some of the models become easier to use and run on microcomputers.

Once a process model has been constructed and verified, it can be used to explore the effects of systematically varying the process variables without resorting to a large number of laboratory experiments. Critical variables can be identified, and the results used to optimize the process. This leads to an improved understanding of the process itself. The model can be used by the materials development engineer to investigate process variables for different product geometries and to consider the changes in processing caused by altering material properties. Different process paths can then be proposed, analyzed, and compared by running the process model. The ability to predict the outcome of a given process path allows the engineer to determine the optimal process path and identify the critical variables that must be monitored during processing to properly control the process.

It is important to realize that because of their simplified assumptions, models do not yield exact solutions to problems; by their very nature, modeling solutions are approximate. Therefore, models must be verified by comparison with experimental data. Examples of simplifications include geometry, such as representing a two-dimensional problem with one-dimensional equations; composition, such as treating the material as homogeneous rather than heterogeneous; properties, such as using constant properties instead of temperature dependent properties; and numerical,

such as utilizing a small number of grid points, hence losing information. Some simplifications are made because there is no alternative, such as when specialized property data are not available. Therefore, all models have limited application. It is imperative to recognize these limits in order to draw reasonable conclusions from the predictions. Although comprehensive models can be developed, they are invariably impractical due to the large amount of input data and computer requirements.

## 2.2 The General Model

The overall problem can be divided into several parts. One such division has been proposed by Loos and Springer [4], suggesting four submodels. Others ([2, 3, 5]) suggested two divisions, with even these being closely related. The first division includes the thermochemical properties such as the extent of cure, temperature and viscosity, as well as flow, including resin flow, fiber volume fraction and consolidation, and fiber orientation. The second division would include the calculation of residual stresses, and the requirements for void suppression and removal. The thermochemical solutions and resin flow are arguably key in understanding and utilizing any simulation, but the residual stress and void calculations would be desirable in an optimized simulation.

The matrix properties required would include thermodynamic properties such as density, specific heat, heat of fusion, and heat of reaction; transport properties, such as viscosity and thermal conductivity; and mechanical properties, such

as thermal expansion, strength, and elasticity. All of these properties would be dependent upon chemical state, physical state, and temperature. The fiber properties required would include thermodynamic, transport and mechanical properties that are dependent upon temperature and direction (axial and radial). The chemical state would include history- dependent and temperature-dependent reaction kinetics (Arrhenius coefficients). The physical state would include temperature- dependent phase changes.

The solution to the system of equations would yield predicted temperature, pressure, and stress as a function of time and position within the material being processed. This system of equations is not only complicated but impossible to solve analytically. The combination of simplified assumptions (geometry, properties, and magnitude of terms) and the numerical methods used in the solution procedure cause the model to be approximate.

## 2.3 Submodels

The submodels that are needed to obtain the governing equations describing the fundamental mechanism in curing are not independent from each other, but are in fact coupled through various laws and conservation equations. Nevertheless, submodels are frequently used to decouple the balance equations in order to investigate a particular aspect of interest or to simplify the manipulations required to solve the equations. It is also convenient to decouple them for discussion purposes.

In the following sections, the five submodels that will be used are described for a general 2–D problem shown in Figure 2.1.

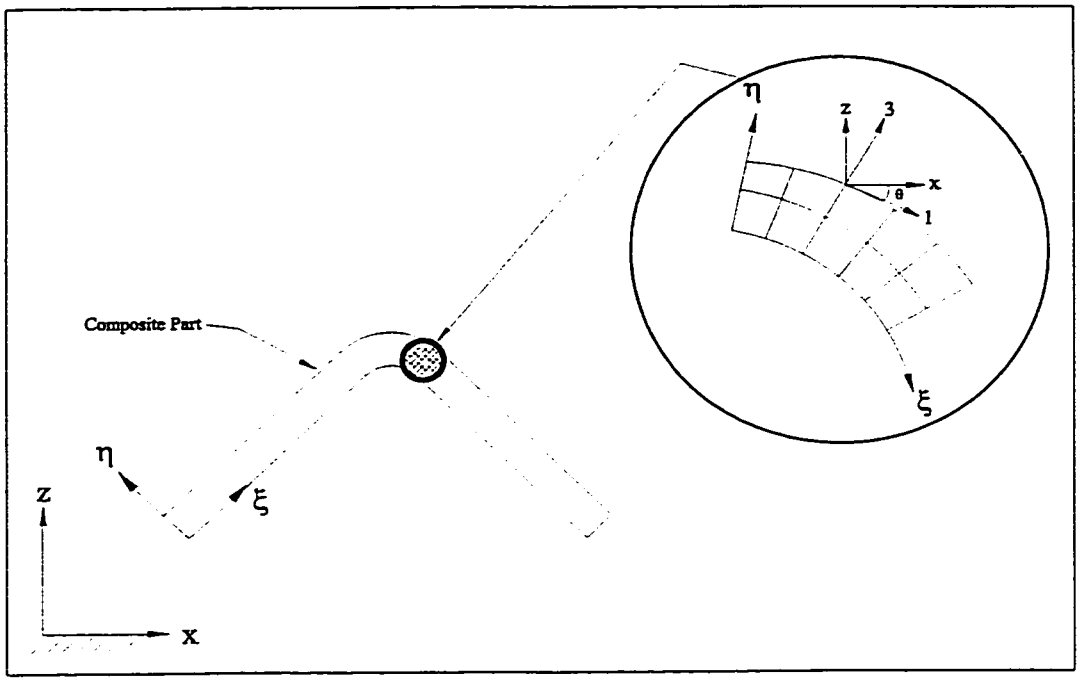


Figure 2.1: The general system of coordinates. $x - z$ is the laminate system of coordinates (global) and $1 - 3$ is the ply system of coordinates (principal direction).

### 2.3.1 Heat Balance Model

The heat balance is described by the conservation of energy equation and is expressed as changes in temperature as a function of position and time. Source terms are required to represent chemical kinetics, such as the exothermic reaction releasing heat within the material. The kinetics, in turn, need to be described by a differential equation since the degree of cure must be calculated. The density and the specific heat of the material are also required data. A variety of different heat sources can be used with the heat submodel through boundary conditions; these include conduction

(heated molds) or convection (autoclave). Radiation or induction heat sources could be accommodated as well, although they would complicate the boundary condition formulation.

Several workers have described heat transfer modeling of composite processing [49, 4, 7, 5, 8, 2, 6]. In this submodel, the temperature solutions are based on Fourier's heat conduction equation for transient anisotropic heat transfer with constant material properties and an internal heat generation source term. This equation may be expressed as:

$$k_{xx}\frac{\partial^2 T}{\partial x^2} + 2k_{xz}\frac{\partial^2 T}{\partial x \partial z} + k_{zz}\frac{\partial^2 T}{\partial z^2} + \dot{q} = \rho c_p \frac{\partial T}{\partial t} \tag{2.1}$$

where $t$ is the time and the $\dot{q}$ term represents the internal heat generation. $\rho$, $c_p$ and $T$ are the density, specific heat and temperature of the composite, respectively. $k_{xx}, k_{zz}$ and $k_{xz}$ are the coefficients of effective anisotropic thermal conductivities. The coordinate directions in equation 2.1 are defined in a fixed global $(x - z)$ coordinate system. Since thermal properties are defined in a principle coordinate system with coordinate axes parallel and perpendicular to the fiber direction then, based on the transformation from the on–axis to the off–axis properties, the coefficients of $k_{xx}, k_{zz}$ and $k_{xz}$ are given by:

$$\begin{Bmatrix} k_{xx} \\ k_{zz} \\ k_{xz} \end{Bmatrix} = \begin{bmatrix} m^2 & n^2 & -2mn \\ n^2 & m^2 & 2mn \\ mn & -mn & m^2 - n^2 \end{bmatrix} \begin{Bmatrix} k_{11} \\ k_{33} \\ k_{13} \end{Bmatrix} \tag{2.2}$$

where $m = cos(\theta)$ and $n = sin(\theta)$. $k_{11}$, $k_{33}$ and $k_{13}$ are the longitudinal, transverse and cross–term thermal conductivities of the composite in its principle (1–3) material coordinate system, respectively. The rotation angle $\theta$ is defined as the local orientation between the fiber or tangent to the fiber direction and the global $(x - z)$ coordinate system.

### 2.3.2 Flow Model

Flow models start with the conservation of momentum equation [10, 50, 51, 52], with pressure, density, viscosity, and local velocity being the primary variables. Since properties such as viscosity are dependent upon temperature, then the energy balance must also be solved in order to investigate pressure–velocity interactions. Fiber orientation may be included in a sophisticated model but neglected in a simpler model. Alternate schemes may be used to simplify or emphasize special aspects of interest. For example, Darcy's law is sometimes used to investigate resin flow through a porous media. The resin may be considered to be Newtonian or even viscoelastic in nature. Based on geometric considerations, the number of dimensions in the problems may be reduced.

When pressure is applied to a composite bleeder system in an autoclave, resin flows from the composite in the directions normal and parallel to the laminate surface [10]. The resin flow rate depends on:

- the magnitude of the portion of the applied pressure which is transmitted to the resin,

- the gas pressure in the bag,
- the viscosity of the resin,
- the specific permeability of the fiber network in each direction,
- the porosity of the fiber network,
- the dimensions of the composite laminate, and
- the boundary condition on the surface such as impermeable boundary or permeable boundary.

The flow is not a steady state, but is transient since there is a continuous depletion of epoxy from the composite with time.

Dave [10] and Gutowski [52] developed, independently, a flow model that is described in terms of Darcy's Law for flow in a porous medium. Unlike previous resin flow models [4, 50, 51], this model properly considers the flow in different directions to be coupled, and provides a unified approach in arriving at the solution. The governing differential equation satisfying the consolidation of a porous bed within a given time interval with 2–D flow and 1–D confined compression condition is given by [10]:

$$S_{xx}\frac{\partial^2 P}{\partial x^2} + 2S_{xz}\frac{\partial^2 P}{\partial x \partial z} + S_{zz}\frac{\partial^2 P}{\partial z^2} = \mu m_v \frac{\partial P}{\partial t} \tag{2.3}$$

where $P$ is the hydraulic resin pressure within the pores, $\mu$ is the viscosity, and $m_v$ is the coefficient of volume change. $m_v$ describes the stress–strain behavior of a body in confined compression. For a porous medium, it is the ratio of change in

porosity to axial stress. $S_{xx}$, $S_{zz}$ and $S_{xz}$ are the coefficients of effective anisotropic specific permeabilities, which depend on the stress level. The off-axis permeabilities are defined in the same way as the off-axis conductivities.

### 2.3.3 Thermo–Kinetic Model

This model describes the kinetics of the chemical transformations in the matrix. It predicts the exothermal heat of reaction and the degree of cure as a function of time and temperature.

For curing reactions, the rate of heat flow ($\frac{dH}{dt}$) can be measured by a differential scanning calorimeter DSC. It has been assumed that $\frac{dH}{dt}$ is directly proportional to the rate of disappearance of reactive groups during curing ($\frac{d\alpha}{dt}$), and full curing, where $\alpha$ is degree of cure and $\alpha = 1$ means that all reactive groups have reacted.

The total heat released to yield a fully cured thermoset is defined as the total heat of reaction $H_R$. So, the reaction rate can be expressed as:

$$\frac{d\alpha}{dt} = \frac{\frac{dH}{dt}}{H_R} \tag{2.4}$$

where $\frac{dH}{dt}$ is the ordinate in a DSC thermogram. Hence, the internal heat generation term $\dot{q}$ in equation 2.1 can be represented as:

$$\dot{q} = \rho_r v_r H_R \frac{d\alpha}{dt} \tag{2.5}$$

where $\rho_r$ and $v_r$ are the resin density and volume fraction, respectively.

The dependence of the cure on the temperature and on the degree of cure must be known to completely define the model. This functional relationship along with

the value of $H_R$ has been determined experimentally for different materials [53, 54]. The usual expression that is used to obtain the kinetic equation for both epoxy and unsaturated polyester systems can be written as:

$$\frac{d\alpha}{dt} = (A_1 \exp(\frac{-E_1}{RT}) + A_2 \exp(\frac{-E_2}{RT})\alpha^{a_1})(B_o - \alpha^{a_2})(1 - \alpha^{a_4})^{a_3} \qquad (2.6)$$

subjected to the initial condition $\alpha(x, z) = 0$ at $t = 0$. $A_1$ and $A_2$ are pre–exponential factors, and $E_1$ and $E_2$ are activation energies. $a_1, a_2, a_3, a_4$, and $B_o$ are constants. $R$ is universal gas constant.

### 2.3.4 Viscosity Model

The viscosity model should be able to predict the viscosity at any combination of temperature and time. Since viscosity $\mu$ depends on the degree of cure, the viscosity model has to be combined with the thermo–kinetic model to become useful. This combination describes the chemorheological behavior of the thermoset. There are two different phenomena which govern the viscosity of a thermoset. One phenomenon is the growing size of the molecules during curing which increases the viscosity of the resin. The other is the effect of temperature on molecular mobility. These two mechanisms together determine the viscosity of reactive polymers in the fluid state. The following expression can be used to describe the resin viscosity of an epoxy system according to Lee and his co-workers [55]:

$$\mu = \mu_\infty \exp\left(\frac{U}{RT} + K_\mu \alpha\right) \qquad (2.7)$$

where $U$ is the activation energy, $R$ is the universal gas constant, $T$ is the absolute temperature, $K_\mu$ is a constant, and $\alpha$ is the degree of cure.

### 2.3.5 Void Model

Ideally, a void model should predict the void size distribution and the positions of the voids at any combination of time, temperature and pressure during the curing process. For the construction of this submodel, a description of the thermo–kinetics, the viscosity and flow behavior of the resin is needed as input data [56]. Unfortunately, it is very difficult to obtain all the information needed to perform the predictions. But a simplified void model can at least help us to limit the risk for voids in our choice of the optimum cure conditions in terms of time, temperature and pressure. The resin pressure early in the cure cycle and the initial resin moisture content are critical considerations in producing void–free laminates.

Since the driving force for diffusion rises with temperature, and in order to prevent the potential for pure water void growth by moisture diffusion in a laminate at all times and temperature, the resin pressure at any point within the curing laminate must satisfy the following inequality [57]:

$$P_{min} \geq 4.962 \times 10^3 exp\left(-\frac{4892}{T}\right)(RH)_o \tag{2.8}$$

where $P_{min}$ (atm) is the minimum resin pressure required to prevent void growth by moisture diffusion at any time during cure, $(RH)_o$ (%) is the relative humidity to which the resin in the prepreg is equilibrated prior to processing, and $T$ (K) is the

temperature at any time during processing.

Equation 2.8 was derived from the requirement that void growth by moisture diffusion at any temperature cannot occur if the pressure within the void is greater than the saturated vapor pressure at that temperature. In terms of moisture concentration, it implies that if the concentration of the water inside the void is always greater than that within the bulk resin, then there is no net positive driving force for void growth during the cure cycle.

## 2.4 Boundary Conditions

### 2.4.1 Temperature Boundary Conditions

A generalized boundary condition formulation is used to permit complete flexibility in the simulation of the autoclave curing process. This is expressed mathematically as:

$$a\frac{\partial T_s}{\partial \hat{n}} + bT_s + cT_a = 0 \text{ for } T(x,z) \text{ on } D \tag{2.9}$$

where $D$ represents the domain boundary, $T_s$ is the specified surface boundary temperature that need to be solved (objective) as a function of time, and $\hat{n}$ is the outward unit normal to the domain surface defined in the $(x,z)$ global coordinate system. The coefficients $a$, $b$ and $c$ define the appropriate effective condition across the boundary of the domain. $T_a$ is the temperature at the boundary surface which can be constant or variable depending on the values of $a$, $b$ and $c$. The three different boundary conditions that may be enforced on the domain boundaries are either

Dirichlet, Neumann or Robin conditions. Table 2.1 summarizes these conditions for temperature boundaries.

| coeff. | $a$ | $b$ | $c$ |
|---|---|---|---|
| **Dirichlet** | 0 | 1 | -1 |
| **Neumann** | 1 | 0 | 0 |
| **Robin** | 1 | $(\frac{h}{k})_{eff}$ | $-(\frac{h}{k})_{eff}$ |

Table 2.1: Generalized Temperature Boundary Condition Coefficients.

Here, $(\frac{h}{k})_{eff}$ is the effective heat transfer coefficient at the laminate surfaces to account for all the thermal resistance associated with the tooling and bag assembly.

- The Dirichlet, or prescribed boundary condition, is most useful when experimental transient part surface temperatures $T_s$ are known.
- The Neumann, or insulated boundary condition, is used when symmetry conditions or insulated surfaces are imposed.
- Robin, or mixed boundary condition, is used when temperature profiles $T_s$ on the boundary are not known prior to simulation.

### 2.4.2 Pressure Boundary Conditions

A generalized boundary condition equation for pressure is used which is similar to that used for temperature. It is written as:

$$a\frac{\partial P_s}{\partial \hat{n}} + bP_s + cP_g = 0 \text{ for } P(x,z) \text{ on } D \tag{2.10}$$

where $P_s$ is the surface boundary pressure that need to be solved as a function of time, and $P_g$ is the actual pressure boundary condition of the surrounding (bag pressure) which can be constant or variable with time.

Formulating pressure boundary conditions for the Dirichlet or Neumann case is a straight forward procedure. When pressure values at the surface boundaries $P_s$ are known, their values are directly applied. Also, when no flow occurs at a surface boundary that has outward unit normal $\hat{n}$, then $\frac{\partial P_s}{\partial \hat{n}}$ is set equal to zero. However, when flow proceeds through different media (as in the case for resin flow out of the laminate through the perforated release film, bleeder and breather layers) and the pressure value at this boundary changes with resin build–up, neither Dirichlet nor Neumann cases will succeed in representing the real situation. Therefore, a generalized boundary condition formulation for pressure must be derived for the following reasons:

1. to avoid the assumption of "free bleeding", i.e. $P_s = 0$ that is associated by excluding the effect of the bleeder on the resin flow behavior [1],

2. to overcome difficulties in modeling the detailed flow at the perforated release film, bleeder and breather layers where resin would bleed out of the laminate freely at first, and then will be restricted when the different cloths are filled with resin [2], and

[1] A procedure followed by most researchers.

[2] A situation that was addressed in Reference [58], and solved by setting $P_s = 0$ at the laminate top surface and $P_s = 0.5MPa$ at the edges.

3. to quantify the combined resistance of release, bleeder and breather materials to flow at that boundary.

To formulate a generalized boundary condition for pressure as well, Darcy's law of permeability will be used. Resin flow rate at the laminate surface, according to this law, is written as [59, 60]:

$$q_n = -\frac{S_p}{\mu}\frac{\partial P_s}{\partial \hat{n}} = -\frac{S_b}{\mu}\frac{\partial P_s}{\partial \hat{n}} \tag{2.11}$$

where $S$ is the permeability in the $\hat{n}$ direction, and subscripts $p$ and $b$ refer to the prepreg material and the bagging materials (perforated release film, bleeder and breather layers), respectively, as shown in Figure 2.2.

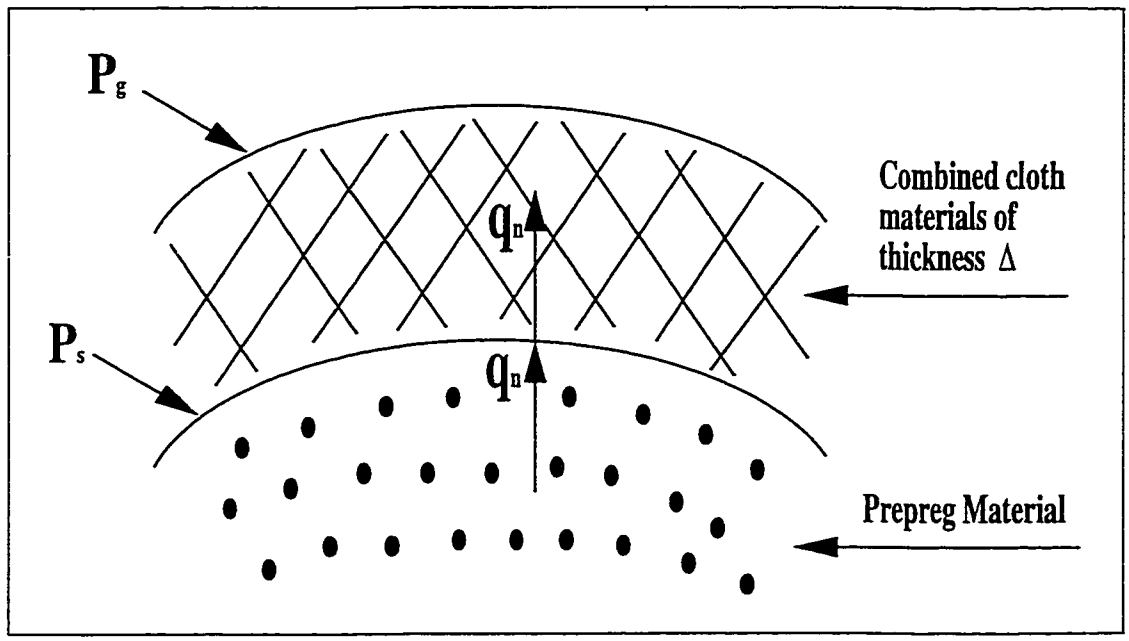


Figure 2.2: Resin flow out of the laminate through the combined release, bleeder and breather materials.

The second term in Equation 2.11 can be approximated by:

$$\frac{S_b}{\mu}\frac{\partial P_s}{\partial \hat{n}} = -\frac{S_b}{\mu}\frac{P_s - P_g}{\Delta} \tag{2.12}$$

$$\begin{aligned} \text{or} \quad & \tfrac{S_b}{\mu}\tfrac{\partial P_s}{\partial \hat{n}} = -\bar{f}_c(P_s - P_g) \\ & \text{where} \quad \bar{f}_c = \tfrac{S_b}{\mu.\Delta} \end{aligned} \tag{2.13}$$

$\bar{f}_c$ is an average flow coefficient that is analogous to the average heat transfer coefficient $h$. $\Delta$ is the thickness of the different bagging materials. Hence, combining equations 2.11 and 2.13, resin flow can be written as:

$$\frac{S_p}{\mu}\frac{\partial P}{\partial \hat{n}} = \bar{f}_c(P_s - P_g) \tag{2.14}$$

$$\begin{aligned} \text{or} \quad & \tfrac{\partial P}{\partial \hat{n}} = (F_c)_{eff}(P_s - P_g) \\ & \text{where} \quad (F_c)_{eff} = \tfrac{S_b}{S_p.\Delta} \end{aligned} \tag{2.15}$$

$(F_c)_{eff}$ is an effective flow coefficient that is analogous to $(\frac{h}{k})_{eff}$ used in heat flow equations. When the value of $(F_c)_{eff}$ is small, then the resistance to flow from laminate to boundary layer is high, and vice versa. Now using equation 2.15 will enable us to formulate a generalized boundary condition for pressure, the same as temperature. This is expressed as follows:

$$a\frac{\partial P}{\partial \hat{n}} + bP_s + cP_g = 0 \ \text{ for } P(x,z) \text{ on } D \tag{2.16}$$

which is the same equation that we started with, Equation 2.10. The three different boundary conditions that may be enforced on the boundaries are summarized in Table 2.2 below.

| coeff. | a | b | c |
|---|---|---|---|
| **Dirichlet** | 0 | 1 | -1 |
| **Neumann** | 1 | 0 | 0 |
| **Robin** | 1 | $(F_c)_{eff}$ | $-(F_c)_{eff}$ |

Table 2.2: Generalized Boundary Condition Coefficients.

- The Dirichlet condition is used when pressure values $P_s$ are known at the boundaries.

- The Neumann condition is used when no–flow or insulated conditions are imposed.

- Robin condition is used to account for the resistance for resin to flow, which is associated with the situation when release, bleeder and breather layers are placed in contact with the surface of the laminate.

The following figure 2.3 shows the implementation of the generalized temperature and pressure boundary conditions for the kind of lay–up that was shown in Figure 1.4. $y_1$ and $y_2$ can be any number.

The next chapter shows the implementation of the governing equations in the numerical solution and the material system used for the simulation and experiments.

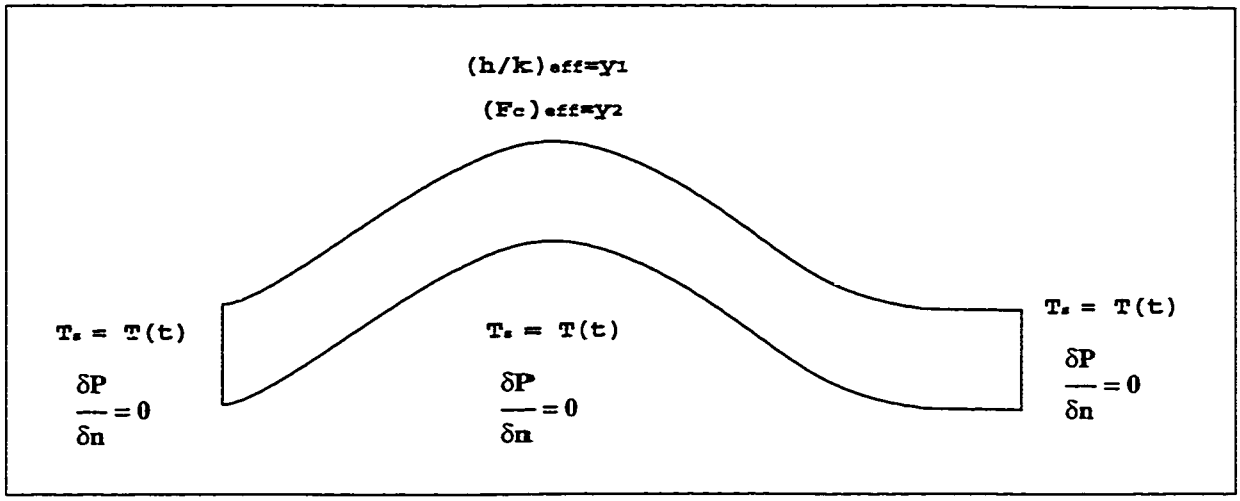


Figure 2.3: Temperature and pressure boundary conditions.

# Chapter 3

# Numerical Solution

## 3.1 Introduction

The strategy to be followed to solve the problem of 2-dimensional anisotropic cure simulation of thick thermosetting arbitrary composite section will be explained and presented in this chapter. Temperature and pressure solutions are based on an incremental transient finite difference formulation. The 2–D analysis utilizes the Boundary–Fitted Coordinate System (BFCS) transformation technique to accommodate arbitrarily shaped cross–sectional geometries. To solve the resulting finite difference equations, the Alternating Direction Explicit (ADE) method is utilized. These methods are discussed below.

## 3.2 Coordinate Transformation

A method is needed with which the irregular physical shape can be mapped into a rectangular computational domain. Thompson [61, 62] described a method called a Boundary-Fitted coordinate System (BFCS) for mapping via a general coordinate transformation, as shown in figure 3.1. The transformation is governed by a set of partial differential equations (PDEs) relating the physical coordinates $x$ and $z$ to the computational coordinates $\xi$and $\eta$ . Also the governing equations and boundary conditions for the problem must be transformed into this computational domain. Once this is done, the problem can be easily solved in the rectangular domain by using finite difference expressions to evaluate the partial derivatives. Solutions are obtained in the computational domain and subsequently mapped back into the physical domain through the correspondence of nodes in the respective planes.

As mentioned previously, the domain transformation is governed by a pair of PDEs. While there may be several types of PDEs which would suffice, the Laplacian equations are chosen because they produce a smoothly distributed grids which conform nicely to the pre-defined boundaries of the domain [63]. This can be described as:

$$\begin{aligned} \frac{\partial^2 \xi}{\partial x^2} + \frac{\partial^2 \xi}{\partial z^2} &= 0 \\ \frac{\partial^2 \eta}{\partial x^2} + \frac{\partial^2 \eta}{\partial z^2} &= 0 \end{aligned} \tag{3.1}$$

These PDEs govern the transformation from the $x - z$ (physical) plane to the $\xi - \eta$ (computational) plane. However, the problem in hand is of the reverse order; the transformed coordinates $(\xi, \eta)$ are the known values while the physical coordinates

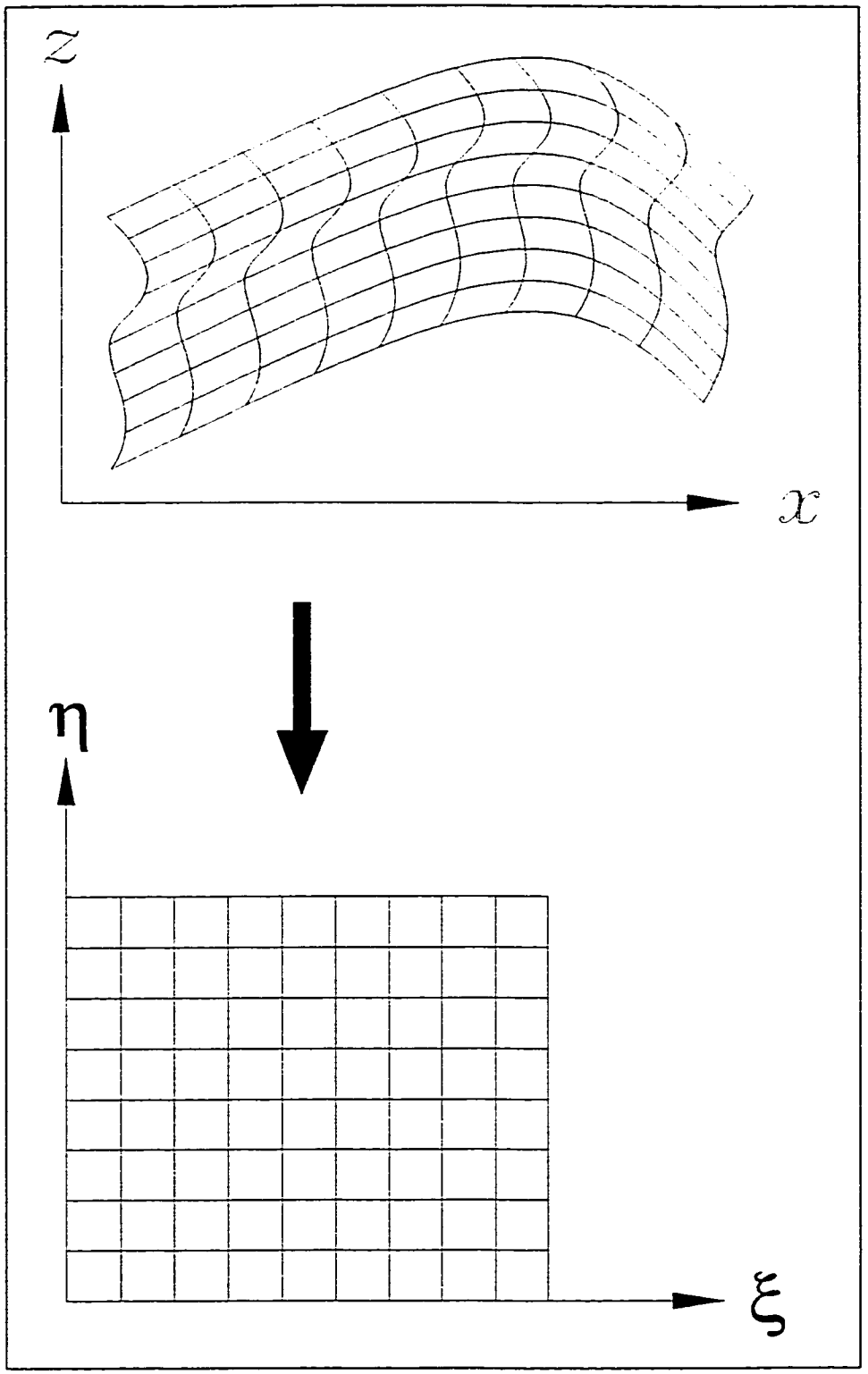


Figure 3.1: Mapping from a physical domain to a computational domain.

are what we are seeking. In order to solve this problem, the dependent and independent variables in Equation 3.1 must be interchanged to provide the inverse transformation. This produces the following equations:

$$\begin{aligned} \wp\frac{\partial^2 x}{\partial \xi^2} - 2\beta\frac{\partial^2 x}{\partial \xi \partial \eta} + \gamma\frac{\partial^2 x}{\partial \eta^2} = 0 \\ \wp\frac{\partial^2 z}{\partial \xi^2} - 2\beta\frac{\partial^2 z}{\partial \xi \partial \eta} + \gamma\frac{\partial^2 z}{\partial \eta^2} = 0 \end{aligned} \tag{3.2}$$

in which $x = x(\xi, \eta)$ and $z = z(\xi, \eta)$ , while the coefficients are expressed as follows:

$$\begin{aligned} \wp &= \left(\frac{\partial x}{\partial \eta}\right)^2 + \left(\frac{\partial z}{\partial \eta}\right)^2 \\ \beta &= \frac{\partial x}{\partial \xi}\frac{\partial x}{\partial \eta} + \frac{\partial z}{\partial \xi}\frac{\partial z}{\partial \eta} \\ \gamma &= \left(\frac{\partial x}{\partial \xi}\right)^2 + \left(\frac{\partial z}{\partial \xi}\right)^2 \end{aligned}$$

and vary from point-to-point throughout the domain. The necessary boundary conditions for equation 3.2 are the $x$ and $z$ coordinates of the nodes along the boundary of the physical domain. Defining the boundary conditions as the specific coordinates of the physical boundaries of the domain gives a unique solution for the mapping.

To solve equation 3.2, the derivatives are approximated by using central finite difference equations (FDEs). These are shown in Appendix A, where $\Delta\xi$ and $\Delta\eta$ are both set equal to 1 to achieve simplicity. This system of equations for $x$ and $z$ can be solved by a number of means among which is the Gauss-Seidel iteration method.

## 3.3 Transformation of Governing Equations

To enable the consideration of irregular shapes, the governing equations introduced in the previous chapter are transformed into a general curvilinear coordinate system

as described in the previous section. The transformation was performed only on the geometrical coordinates and not in the time domain. Since these derivations are rather lengthy, they are given in Appendix B with the results provided below.

Bogetti [64] used the BFCS technique in transforming the heat equation 2.1 and the generalized boundary condition equation 2.9. Following his steps, the transformation of the heat conduction equations 2.1 into the computational domain produces the following equation:

$$\mathcal{A}_1\frac{\partial^2 T}{\partial \xi^2}+\mathcal{A}_2\frac{\partial^2 T}{\partial \eta^2}+\mathcal{A}_3\frac{\partial^2 T}{\partial \xi \partial \eta}+\mathcal{A}_4\frac{\partial T}{\partial \xi}+\mathcal{A}_5\frac{\partial T}{\partial \eta}+\dot{q}=\rho c_v\frac{\partial T}{\partial t} \tag{3.3}$$

Similarly, for the resin flow equation 2.3, transformation produces:

$$\mathcal{B}_1\frac{\partial^2 P}{\partial \xi^2}+\mathcal{B}_2\frac{\partial^2 P}{\partial \eta^2}+\mathcal{B}_3\frac{\partial^2 P}{\partial \xi \partial \eta}+\mathcal{B}_4\frac{\partial P}{\partial \xi}+\mathcal{B}_5\frac{\partial P}{\partial \eta}=\mu m_v\frac{\partial P}{\partial t} \tag{3.4}$$

The coefficients $\mathcal{A}_i$ are functions of the effective thermal conductivities, and $\mathcal{B}_i$ are functions of the effective permeabilities and are both defined in Appendix B.

Also, the generalized boundary condition equations 2.9 and 2.16 need to be transformed since $\frac{\partial T}{\partial \hat{n}}$ and $\frac{\partial P}{\partial \hat{n}}$ on the domain boundary are required. The transformations were given by Trafford [65], but are shown in Appendix C for the sake of completeness. For each surface of the four boundaries shown in Figure 3.2, the transformations produce the following:

$$\begin{aligned}
&a\tfrac{\overline{\rho}\Psi_\xi-\beta\Psi_\eta}{J\sqrt{\overline{\rho}}}+b\Psi_s+c\Psi(t)=0 && \text{on the } \hat{n}(+\xi)\text{face}\\
&a\tfrac{\overline{\gamma}\Psi_\eta-\beta\Psi_\xi}{J\sqrt{\overline{\gamma}}}+b\Psi_s+c\Psi(t)=0 && \text{on the } \hat{n}(+\eta)\text{face}\\
&a\tfrac{\beta\Psi_\eta-\overline{\rho}\Psi_\xi}{J\sqrt{\overline{\rho}}}+b\Psi_s+c\Psi(t)=0 && \text{on the } \hat{n}(-\xi)\text{face}\\
&a\tfrac{\beta\Psi_\xi-\overline{\gamma}\Psi_\eta}{J\sqrt{\overline{\gamma}}}+b\Psi_s+c\Psi(t)=0 && \text{on the } \hat{n}(-\eta)\text{face}
\end{aligned} \tag{3.5}$$

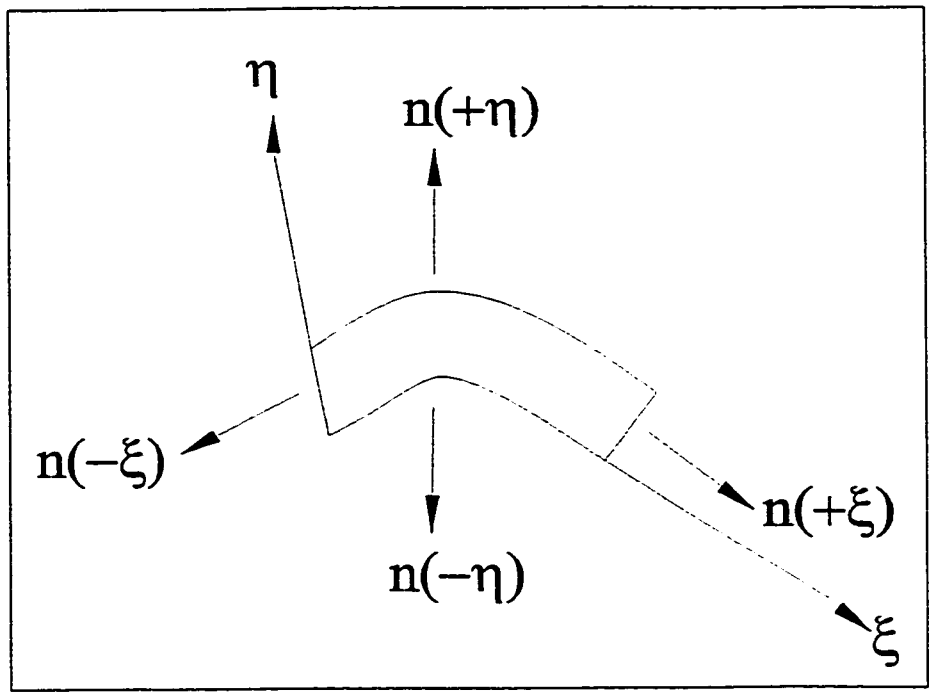


Figure 3.2: Different faces of the computational domain.

where $\Psi$ can be either $T$ or $P$, and $\hat{n}(+\xi)$, $\hat{n}(+\eta)$, $\hat{n}(-\xi)$ and $\hat{n}(-\eta)$ are the faces of the four boundaries. Subscripts $\xi$ and $\eta$ denote partial differentiation with respect to the rectangular $(\xi, \eta)$ computational domain spatial coordinates.

As one can see, the general coordinate transformation substantially complicated the governing equation. This was the price paid for the ability to analyze complex shapes with relatively simple finite difference equations. One should note that these transformed equations were independent of the method used to generate the coordinate mesh.

## 3.4 Material System Used

Physical properties of the composite are considered to be function of fiber volume fraction. This type of calculation provides more accurate results in the simulation. Due to the non-uniform resin flow through the thickness, there would be a fiber volume fraction gradient, causing different physical properties at different locations.

Hercules graphite/epoxy prepregs, commercially called AS4/3501-6, is chosen due to the wealth of information available in the literature. This is a representative epoxy system used widely in aerospace applications. The prepreg specifications as well as kinetic and viscosity parameters that will be used in the rest of this work are taken from [55, 66], and shown in table 3.1 below. The thickness of each ply is approximately 0.16 mm and it has 36% resin content by weight. The chemical composition along with basic epoxy reactions are explained in Appendix D.

## 3.5 Micromechanics

### 3.5.1 Thermal Kinetics

The composite heat capacity $c_p$ , density $\rho$ and conductivity $k_{11}$ in the fiber direction are calculated using rule of mixture:

$$\begin{aligned} \rho &= \rho_f v_f + \rho_r(1 - v_f) \\ c_p &= c_{pf} m_f + c_{pr}(1 - m_f) \\ k_{11} &= k_f v_f + k_r(1 - v_f) \end{aligned} \tag{3.6}$$

| | | |
|---|---|---|
| Fiber radius | $r_f$ | $3.5 \times 10^{-6} m$ |
| Fiber density | $\rho_f$ | $1.79 \times 10^3 \frac{kg}{m^3}$ |
| Specific heat of fiber | $c_{pf}$ | $7.12 \times 10^2 \frac{J}{kg.K}$ |
| Thermal conductivity of fiber | $k_f$ | $26 \frac{W}{m.K}$ |
| Resin density | $\rho_r$ | $1.26 \times 10^3 \frac{kg}{m^3}$ |
| Specific heat of resin | $c_{pr}$ | $1.26 \times 10^3 \frac{J}{kg.K}$ |
| Thermal conductivity of resin | $k_r$ | $0.167 \frac{W}{m.K}$ |
| Pre-exponential factor | $A_1$ | $2.101 \times 10^9 min^{-1}$ |
| Pre-exponential factor | $A_2$ | $-2.014 \times 10^9 min^{-1}$ |
| Pre-exponential factor | $A_3$ | $1.96 \times 10^5 min^{-1}$ |
| Activation energy | $E_1$ | $8.07 \times 10^4 \frac{J}{mol}$ |
| Activation energy | $E_2$ | $7.78 \times 10^4 \frac{J}{mol}$ |
| Activation energy | $E_3$ | $5.66 \times 10^4 \frac{J}{mol}$ |
| Heat of reaction | $H_R$ | $4.74 \times 10^5 \frac{J}{kg}$ |
| Activation energy for viscosity | $U$ | $9.08 \times 10^4 \frac{J}{kg}$ |
| Viscosity constant | $\mu_\infty$ | $7.93 \times 10^{-14} Pa.s$ |
| Viscosity constant | $K_\mu$ | 14.1 |

Table 3.1: Material properties of Hercules AS4/3501-6 [55,66].

where subscripts $f$ and $r$ stands for fiber and resin, respectively. $v$ is the volume fraction and $m$ is the mass fraction.

The composite thermal conductivity $k_{33}$ perpendicular to the fiber direction is calculated using Springer and Tsai model [67]:

$$\frac{k_{33}}{k_r} = \left(1 - 2\sqrt{\frac{v_f}{\pi}}\right) + \frac{1}{\mathcal{D}}\left[\pi - \frac{4}{\sqrt{1-\frac{\mathcal{D}^2 v_f}{\pi}}} \arctan\left(\frac{\sqrt{1-\frac{\mathcal{D}^2 v_f}{\pi}}}{1+\mathcal{D}\sqrt{\frac{v_f}{\pi}}}\right)\right] \qquad (3.7)$$
$$\mathcal{D} = 2\left(\frac{k_r}{k_f} - 1\right)$$

The cross-term thermal conductivity $k_{13}$ equals to zero.

### 3.5.2 Chemical Reaction Kinetics

The reaction rate expression for Hercules 3501-6 resin can be expressed as [55]:

$$\frac{d\alpha}{dt} = \begin{cases} (K_1 + K_2\alpha)(1-\alpha)(0.47-\alpha) & \alpha \leq 0.3 \\ K_3(1-\alpha) & \alpha > 0.3 \end{cases} \qquad (3.8)$$
$$\text{where} \quad K_i = A_i \exp\left(\frac{-E_i}{RT}\right) \quad ; \quad i = 1,2,3$$

subjected to the initial condition $\alpha(x,z) = 0$ at $t = 0$.

### 3.5.3 Flow Kinetics

The axial and transverse permeabilities are functions of the state of the fiber bed. Traditionally, researchers have relied on the Carman–Kozeny equation [59] to calculate $S_{11}$ and $S_{33}$. This is given by:

$$S_{11} = \frac{r_f^2}{4\kappa_{11}} \frac{(1-v_f)^3}{v_f^2}$$
$$S_{33} = \frac{r_f^2}{4\kappa_{33}} \frac{(1-v_f)^3}{v_f^2} \qquad (3.9)$$

Here, $r_f$ is the fiber radius, $\kappa$ is the Kozeny constant and takes the values 0.3 along the fibers ($i$=1) and 6.0 transverse to the fibers ($i$=3). $\kappa$ is not a true

constant but, for limited ranges of porosity, it can be considered constant. However, equation 3.9 does not yield a very satisfactory approach for describing fiber bed permeabilities because of its empirical nature [29].

Van der Westhuizen and Du Plessis [68, 69] developed a closed form solution for the permeability of unidirectional laminates. These solutions were shown to compare well with experimental measurements. For circular fibers, these permeabilities are:

$$\begin{aligned} S_{11} &= \frac{r_f^2(\pi+2.15v_f)(1-v_f)^2}{48v_f^2} \\ S_{33} &= \frac{r_f^2\pi(1-v_f^*)(1-\sqrt{v_f^*})^2}{24(v_f^*)^{1.5}} \end{aligned} \tag{3.10}$$

where
$$\begin{aligned} v_f^* &= v_f & v_f < 0.5 \\ v_f^* &= 2.22v_f^2 - 1.22v_f + 0.56 & v_f \geq 0.5 \end{aligned}$$

The cross-term permeability $S_{13}$ equals to zero. Equation 3.10 was used throughout this research.

### 3.5.4 Coefficient of Volume Change

According to Dave et. al. [10, 70], the coefficient of volume change $m_v$ is expressed as:

$$m_v = \frac{1}{v_f}\frac{dv_f}{dP_f} \tag{3.11}$$

where $P_f$ is the fiber pressure.

### 3.5.5 Stress–Strain Relations

Many workers tried to model the stress–strain relationship of a fiber bed. Dave et al [10] used a stress–strain relation which was based on experimental data by Gutowski [52] to simulate composite processing. The stress–strain relationship they used was:

$$e = \begin{cases} -1.556 \times 10^{-3} P_f + 0.810 & 0 \leq P_f \leq 68.747\ kPa \\ -0.134 \log P_f + 0.951 & 68.747 \leq P_f \leq 1030.61\ kPa \end{cases} \tag{3.12}$$

where $P_f$ is the fiber pressure in $kPa$. $e$ is the void ratio (volume of voids per unit volume of solid constituents) given by the ratio $\frac{1-v_f}{v_f}$. Hence, equation 3.12 can be written as:

$$v_f = \begin{cases} 5.0329 \times 10^{-4} P_f + 0.552 & 0 \leq P_f \leq 68.747\ kPa \\ 0.0444 \ln P_f + 0.395 & 68.747 \leq P_f \leq 1030.61\ kPa \end{cases} \tag{3.13}$$

The stress–strain relationship used by Gutowski [52] was:

$$e = \begin{cases} -1.552 \times 10^{-3} P_f + 0.810 & 0 \leq P_f \leq 68.95\ kPa \\ -0.247 \log P_f + 1.899 & 68.95 \leq P_f \leq 1034\ kPa \end{cases} \tag{3.14}$$

from which we get:

$$v_f = \begin{cases} 5.033 \times 10^{-4} P_f + 0.55 & 0 \leq P_f \leq 68.95\ kPa \\ 0.275 P_f^{0.0679} & 68.95 \leq P_f \leq 1034\ kPa \end{cases} \tag{3.15}$$

Also, Hojjati [6] used another relationship in his work given by:

$$v_f = \begin{cases} 6.915 \times 10^{-4} P_f + 0.530 & 0 \leq P_f \leq 68.7\ kPa \\ 0.109 \log P_f + 0.377 & 68.7 \leq P_f \leq 1030.61\ kPa \end{cases} \tag{3.16}$$

In this work, the stress–strain relation obtained by Gutowski (equation 3.14) will be used. So, from equation 3.15, $\frac{dv_f}{dP_f}$ can be obtained as:

$$\frac{dv_f}{dP_f} = \begin{cases} 5.033 \times 10^{-4} & 0 \leq P_f \leq 68.95\ kPa \\ \frac{0.0187}{P_f^{0.932}} & 68.95 \leq P_f \leq 1034\ kPa \end{cases} \tag{3.17}$$

### 3.5.6 Void Growth

In this part of the general model, the resin pressure $P$ calculated from the flow model is checked against $P_{min}$ calculated from Equation 2.8. If $P$ is always greater than $P_{min}$ throughout the curing cycle, then the potential for void growth can be minimized.

## 3.6 Finite Difference Solution Procedure

This section describes the numerical methods used to solve the transformed governing equations and boundary conditions. As explained previously, the BFCS technique allowed for irregularly–shaped domains via relatively straight forward finite difference approximations of the derivatives in the transformed equations.

The Alternating Direction Explicit (ADE) finite difference method [71] is employed in the solution of equations 3.3 and 3.4. The computational mesh of nodal dimensions $m$ and $n$ is illustrated in the Figure 3.3. Central differencing formulas are employed at all interior nodes, while forward and backward differencing formulas are used on the boundary nodes.

### 3.6.1 The ADE Method

Substantial reduction in computation time is realized when the ADE method is used rather than an implicit method [64]. The ADE does not require matrices to be inverted, a situation encountered in the implicit approach. It is also preferred over

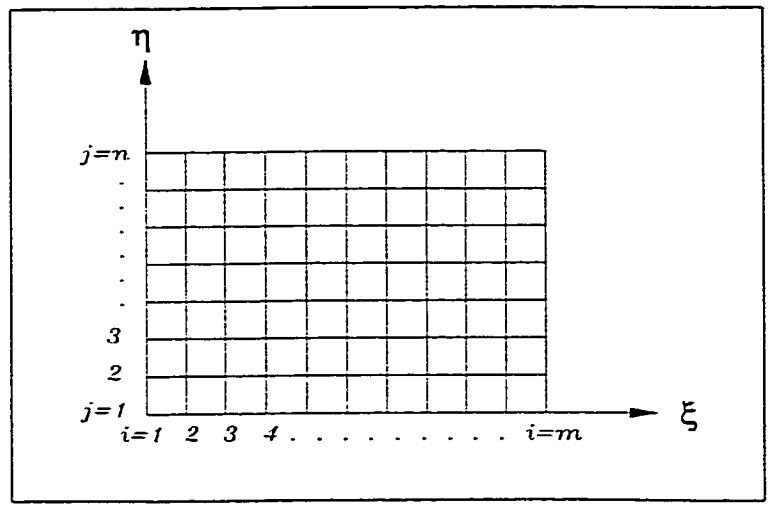


Figure 3.3: The rectangular computational mesh.

a fully explicit method since it has been shown to be unconditionally stable with time step size, and is less sensitive to computational errors [71].

The ADE finite difference method applies a fully explicit approach twice on the computational domain for each time step increment. The calculation procedure is simultaneously marched in both forward and reverse directions and the resulting solutions are averaged to obtain the final value. One sweep through finite difference mesh is made in a systematic forward direction where a pseudo–temperature $(u_{i,j})_T$ or pseudo–pressure $(u_{i,j})_P$ solution, at each interior node is defined explicitly in terms of adjacent nodes. For the same time step, another sweep is made in exactly the reverse direction to obtain a second pseudo–temperature $(v_{i,j})_T$ and pseudo–pressure $(v_{i,j})_P$ solutions. The temperature/pressure at node $i, j$ is then computed at each interior node for the current time step as the arithmetic average of the two

pseudo–temperature/pressure solution:

$$T^t_{i,j} = \frac{\left(u^t_{i,j}\right)_T + \left(v^t_{i,j}\right)_T}{2} \tag{3.18}$$

$$P^t_{i,j} = \frac{\left(u^t_{i,j}\right)_P + \left(v^t_{i,j}\right)_P}{2} \tag{3.19}$$

The advantage of this method is two fold. First it is unconditionally stable, and second the truncation error is approximately $O[(\Delta t)^2, (\Delta\xi)^2, (\Delta\eta)^2]$.

### 3.6.2 Temperature Equation

Following the detailed procedure described by Barakat and Clark [71] and implemented by Boggetti [64], Equation 3.3 is discretized in the forward direction as follows:

$$\begin{aligned}(\mathcal{A}_1)_{i,j}\left[u^t_{i+1,j} - \left(u^t_{i,j} + u^{t+\Delta t}_{i,j}\right) + u^{t+\Delta t}_{i-1,j}\right] + (\mathcal{A}_2)_{i,j}\left[u^t_{i,j+1} - \left(u^t_{i,j} + u^{t+\Delta t}_{i,j}\right) + u^{t+\Delta t}_{i,j-1}\right] \\ + \left(\tfrac{\mathcal{A}_3}{4}\right)_{i,j}\left(u^t_{i+1,j+1} - u^{t+\Delta t}_{i+1,j-1} - u^t_{i-1,j+1} + u^{t+\Delta t}_{i-1,j-1}\right) + \left(\tfrac{\mathcal{A}_4}{2}\right)_{i,j}\left(u^t_{i+1,j} - u^{t+\Delta t}_{i-1,j}\right) \\ + \left(\tfrac{\mathcal{A}_5}{2}\right)_{i,j}\left(u^t_{i,j+1} - u^{t+\Delta t}_{i,j-1}\right) + \dot{q}^t_{i,j} = (\rho c_p)_{i,j}\left(\tfrac{u^{t+\Delta t}_{i,j} - u^t_{i,j}}{\Delta t}\right)\end{aligned} \tag{3.20}$$

from which the expression for the temperature $(u_{i,j})_T$ at the time step $t + \Delta t$ for an interior node during a forward sweep is given by:

$$\begin{aligned}\left(u^{t+\Delta t}_{i,j}\right)_T = \left(\tfrac{1}{\frac{\rho c_p}{\Delta t} + \mathcal{A}_1 + \mathcal{A}_2}\right)_{i,j}\Big[&\left(\tfrac{\rho c_p}{\Delta t}\right)_{i,j} u^t_{i,j} + \dot{q}^t_{i,j} \\ &+ (\mathcal{A}_1)_{i,j}\left(u^t_{i+1,j} - u^t_{i,j} + u^{t+\Delta t}_{i-1,j}\right) \\ &+ (\mathcal{A}_2)_{i,j}\left(u^t_{i,j+1} - u^t_{i,j} + u^{t+\Delta t}_{i,j-1}\right) \\ &+ \left(\tfrac{\mathcal{A}_3}{4}\right)_{i,j}\left(u^t_{i+1,j+1} - u^{t+\Delta t}_{i+1,j-1} - u^t_{i-1,j+1} + u^{t+\Delta t}_{i-1,j-1}\right) \\ &+ \left(\tfrac{\mathcal{A}_4}{2}\right)_{i,j}\left(u^t_{i+1,j} - u^{t+\Delta t}_{i-1,j}\right) + \left(\tfrac{\mathcal{A}_5}{2}\right)_{i,j}\left(u^t_{i,j+1} - u^{t+\Delta t}_{i,j-1}\right)\Big]\end{aligned} \tag{3.21}$$

The $(u_{i,j})_T$'s at time $t + \Delta t$ step on the right–hand side of equation 3.21 all have previously been computed during the same time step. Similarly, Equation 3.3 is discretized in the backward direction to yield:

$$\begin{aligned}(\mathcal{A}_1)_{i,j}\left[v_{i+1,j}^{t+\Delta t} - \left(v_{i,j}^{t+\Delta t} + v_{i,j}^{t}\right) + v_{i-1,j}^{t}\right] + (\mathcal{A}_2)_{i,j}\left[v_{i,j+1}^{t+\Delta t} - \left(v_{i,j}^{t+\Delta t} + v_{i,j}^{t}\right) + v_{i,j-1}^{t}\right] \\ + \left(\tfrac{\mathcal{A}_3}{4}\right)_{i,j}\left(v_{i+1,j+1}^{t+\Delta t} - v_{i+1,j-1}^{t} - v_{i-1,j+1}^{t+\Delta t} + v_{i-1,j-1}^{t}\right) + \left(\tfrac{\mathcal{A}_4}{2}\right)_{i,j}\left(v_{i+1,j}^{t+\Delta t} - v_{i-1,j}^{t}\right) \\ + \left(\tfrac{\mathcal{A}_5}{2}\right)_{i,j}\left(v_{i,j+1}^{t+\Delta t} - v_{i,j-1}^{t}\right) + \dot{q}_{i,j}^{t} = (\rho c_p)_{i,j}\left(\tfrac{v_{i,j}^{t+\Delta t} - v_{i,j}^{t}}{\Delta t}\right)\end{aligned} \tag{3.22}$$

from which the pseudo–temperature $(v_{i,j})_T$ at time step $t + \Delta t$ for an interior node during a backward sweep is given by:

$$\begin{aligned}\left(v_{i,j}^{t+\Delta t}\right)_T = \left(\tfrac{1}{\frac{\rho c_p}{\Delta t} + \mathcal{A}_1 + \mathcal{A}_2}\right)_{i,j}\Big[&\left(\tfrac{\rho c_p}{\Delta t}\right)_{i,j} v_{i,j}^{t} + \dot{q}_{i,j}^{t} \\ &+ (\mathcal{A}_1)_{i,j}\left(v_{i+1,j}^{t+\Delta t} - v_{i,j}^{t} + v_{i-1,j}^{t}\right) \\ &+ (\mathcal{A}_2)_{i,j}\left(v_{i,j+1}^{t+\Delta t} - v_{i,j}^{t} + v_{i,j-1}^{t}\right) \\ &+ \left(\tfrac{\mathcal{A}_3}{4}\right)_{i,j}\left(v_{i+1,j+1}^{t+\Delta t} - v_{i+1,j-1}^{t} - v_{i-1,j+1}^{t+\Delta t} + v_{i-1,j-1}^{t}\right) \\ &+ \left(\tfrac{\mathcal{A}_4}{2}\right)_{i,j}\left(v_{i+1,j}^{t+\Delta t} - v_{i-1,j}^{t}\right) + \left(\tfrac{\mathcal{A}_5}{2}\right)_{i,j}\left(v_{i,j+1}^{t+\Delta t} - v_{i,j-1}^{t}\right)\Big]\end{aligned} \tag{3.23}$$

where the $(v_{i,j})_T$'s at time step $t + \Delta t$ on the right-hand side of equation 3.23 are those previously computed during the same time step. Temperature is then calculated using equation 3.18.

The heat generation term $\dot{q}_{i,j}^{t}$ is computed from equation 2.5 as:

$$\dot{q}_{i,j}^{t} = \rho H_R \left(\frac{d\alpha}{dt}\right)_{i,j}^{t} \tag{3.24}$$

where $\left(\frac{d\alpha}{dt}\right)_{i,j}^{t}$ is the instantaneous cure rate evaluated at time step $t$. Also,

$$\alpha_{i,j}^{t+1} = \alpha_{i,j}^{t} + \Delta t \left(\frac{d\alpha}{dt}\right)_{i,j}^{t+1} \tag{3.25}$$

Instantaneous cure rates are computed based on instantaneous temperature and degree of cure through the empirical rate expression shown in equation 3.8. Temperature Distributions at time step $t+\Delta t$ are obtained by solving the finite difference equations 3.21 and 3.23 and substituting into 3.18 in conjunction with the appropriate boundary condition.

### 3.6.3 Pressure Equation

Following the same procedure in discretising temperature, pressure $P^t_{i,j}$ at each point is calculated using equation 3.19. The pseudo–pressure equations are derived as above, and are given below.

$$\begin{aligned}\left(u^{t+\Delta t}_{i,j}\right)_P = &\left(\tfrac{1}{\frac{\mu m_v}{\Delta t}+\mathcal{B}_1+\mathcal{B}_2}\right)_{i,j}\Big[\left(\tfrac{\mu m_v}{\Delta t}\right)_{i,j}u^t_{i,j}\\ &+(\mathcal{B}_1)_{i,j}\left(u^t_{i+1,j}-u^t_{i,j}+u^{t+\Delta t}_{i-1,j}\right)\\ &+(\mathcal{B}_2)_{i,j}\left(u^t_{i,j+1}-u^t_{i,j}+u^{t+\Delta t}_{i,j-1}\right)\\ &+\left(\tfrac{\mathcal{B}_3}{4}\right)_{i,j}\left(u^t_{i+1,j+1}-u^{t+\Delta t}_{i+1,j-1}-u^t_{i-1,j+1}+u^{t+\Delta t}_{i-1,j-1}\right)\\ &+\left(\tfrac{\mathcal{B}_4}{2}\right)_{i,j}\left(u^t_{i+1,j}-u^{t+\Delta t}_{i-1,j}\right)+\left(\tfrac{\mathcal{B}_5}{2}\right)_{i,j}\left(u^t_{i,j+1}-u^{t+\Delta t}_{i,j-1}\right)\Big]\end{aligned} \tag{3.26}$$

and

$$\begin{aligned}\left(v^{t+\Delta t}_{i,j}\right)_P = &\left(\tfrac{1}{\frac{\mu m_v}{\Delta t}+\mathcal{B}_1+\mathcal{B}_2}\right)_{i,j}\Big[\left(\tfrac{\mu m_v}{\Delta t}\right)_{i,j}v^t_{i,j}\\ &+(\mathcal{B}_1)_{i,j}\left(v^{t+\Delta t}_{i+1,j}-v^t_{i,j}+v^t_{i-1,j}\right)\\ &+(\mathcal{B}_2)_{i,j}\left(v^{t+\Delta t}_{i,j+1}-v^t_{i,j}+v^t_{i,j-1}\right)\\ &+\left(\tfrac{\mathcal{B}_3}{4}\right)_{i,j}\left(v^{t+\Delta t}_{i+1,j+1}-v^t_{i+1,j-1}-v^{t+\Delta t}_{i-1,j+1}+v^t_{i-1,j-1}\right)\\ &+\left(\tfrac{\mathcal{B}_4}{2}\right)_{i,j}\left(v^{t+\Delta t}_{i+1,j}-v^t_{i-1,j}\right)+\left(\tfrac{\mathcal{B}_5}{2}\right)_{i,j}\left(v^{t+\Delta t}_{i,j+1}-v^t_{i,j-1}\right)\Big]\end{aligned} \tag{3.27}$$

## 3.7 Solution Algorithm

A computer code was developed to solve the cure simulation equations. The flow chart for solution algorithm is shown in Figure 3.4. The output includes temperature $T$, pressure $P$, degree of cure $\alpha$, viscosity $\mu$ and fiber volume fraction $v_f$ at each time step. Updating the mesh is carried out by fixing the laminate surfaces adjacent to the mold surface and the dams, and by moving the free upper surface as a result of laminate compaction.

To coduct the cure simulation, the time step $\Delta t$ and the total cure time must be defined. Small time step size, on one hand, means accurate solution and, on the other hand, means more computational time. Bogetti [64] showed that even though the ADE method is unconditionally stable with any time step size, a time step size between one and two seconds yielded converged solutions for all the cure simulations conducted in his work.

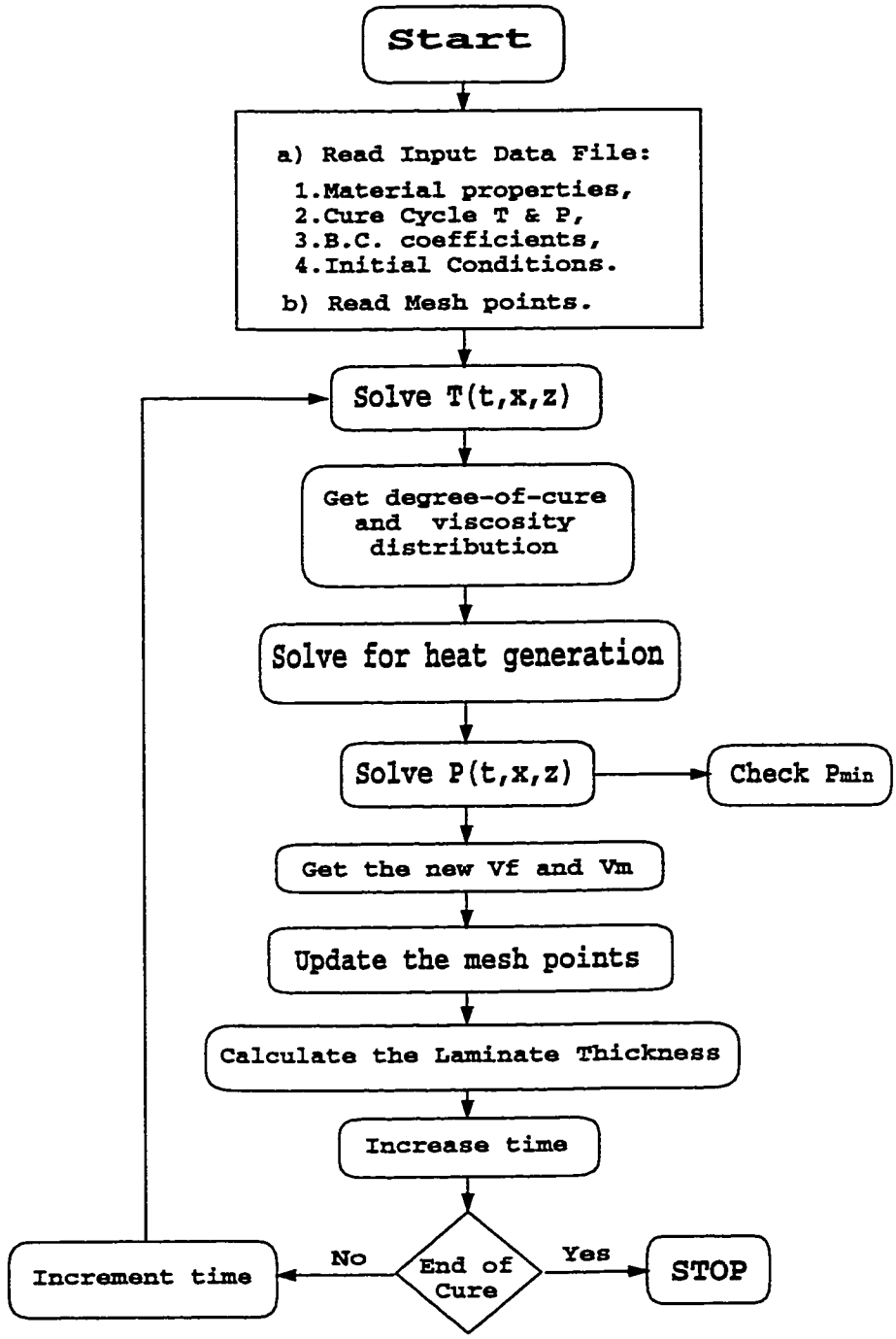


Figure 3.4: The solution algorithm flow chart.

# Chapter 4

# Experimental and Simulation Results

## 4.1 Introduction

Although most models are based on first principles, their validation must be determined by tests. In fact, numerous measurements have been reported on composite temperatures and degree of cure variations during cure. Specifically, the two main goals of this chapter are (1) to perform experiments based on the recommended cure cycles and compare the results with the output of the computer code based on the various cure models, and (2) to reveal problems unique to the angle–bend composite parts.

## 4.2 Experimental Apparatus and Procedure

Hercules AS4/3501-6 graphite/epoxy laminate made of 50 layers of unidirectional tape was cured inside an Autoclave. A photo of the autoclave is shown in Figure 4.1. The thickness of each ply is approximately 0.16 mm and has 36% resin content by weight before cure. The cure assembly consisted of the following components [1] as shown in Figure 4.2:

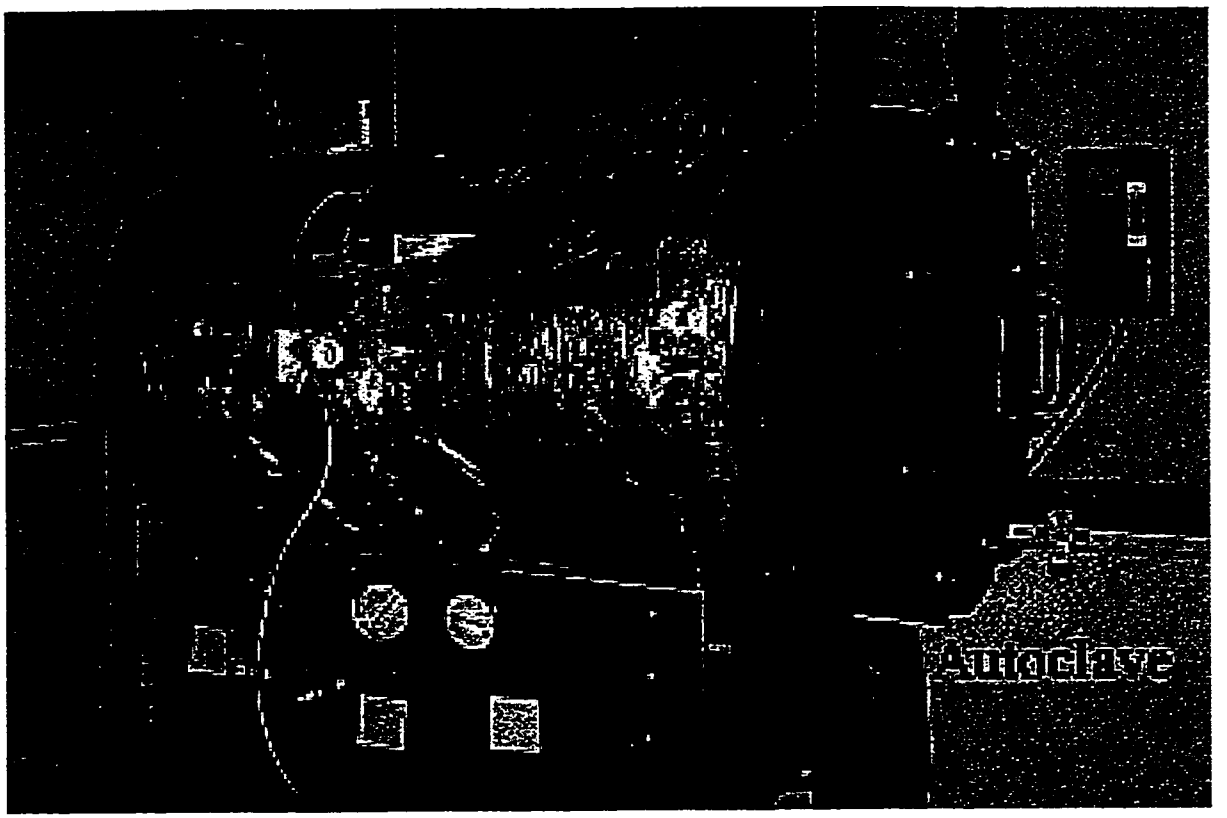

Figure 4.1: A photo of the autoclave used to process the samples.

[1]Bagging materials were provided by the AIRTECH International INC.

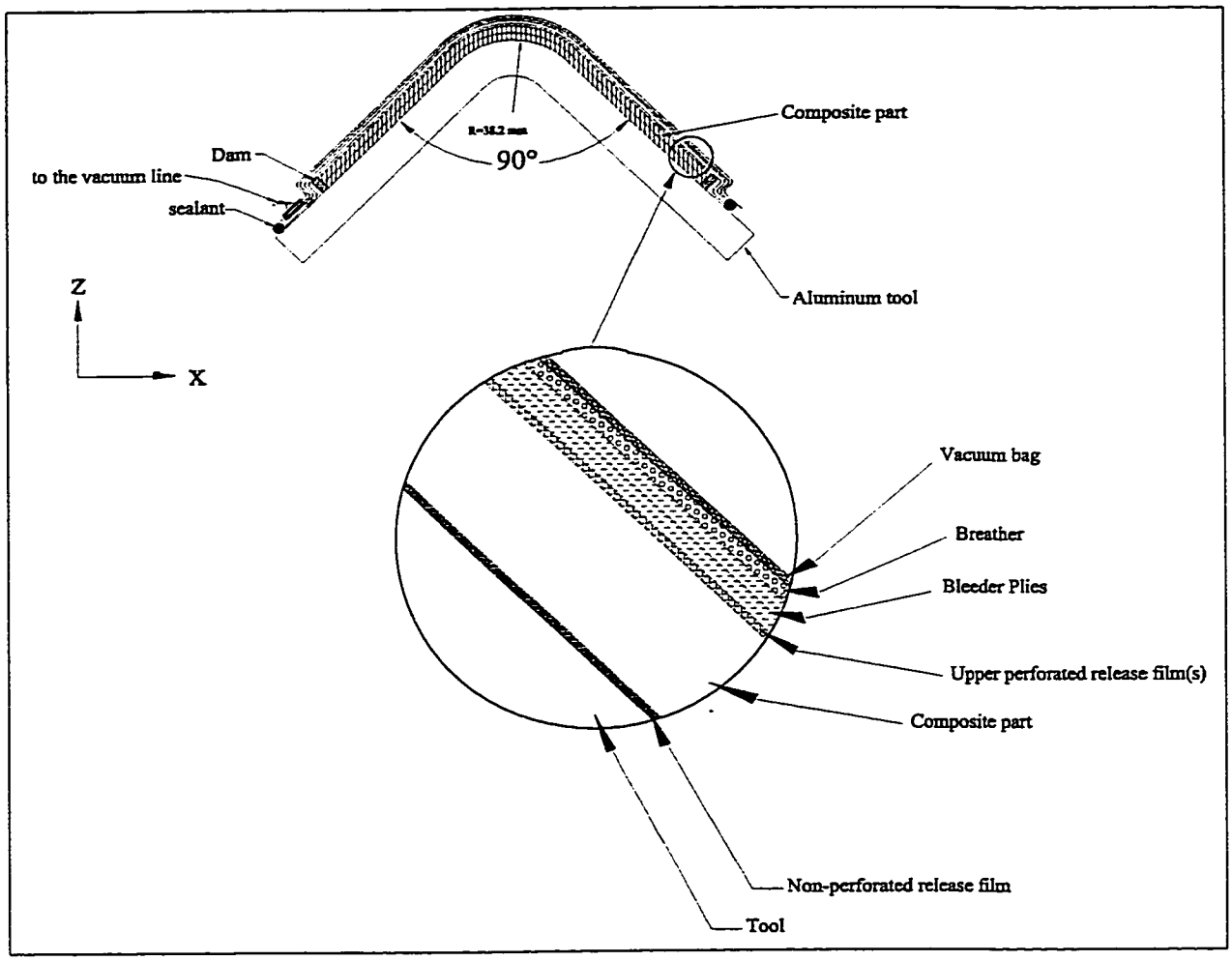


Figure 4.2: Components of the cure assembly.

- Aluminum mold machined from a $25mm$ thick plate with 90° angle and $165mm \times 153mm$ sides.
- Non–perforated Teflon ply (Release Ease 234 TFP Non–Perforated).
- 50 layers of AS4/3501-6 graphite/epoxy.
- Perforated release coated glass fabric (Release Ease 234 TFP Perforated) with 0.003 inch ply thickness.
- 3 layers of bleeder plies (Air Weave FR) placed on top of the laminate. Fabric thickness is 0.013 inch.
- One breather layer.
- Vacuum bag.

Insulator dams were installed in the $y$–direction to restrict resin and heat flows. This was done using one-inch thick fire brick stone. To allow one dimensional compaction, two aluminum dams of thickness $6mm$ were installed as shown in Figure 4.2. A vacuum line was fed into this outer layer before inserting the charge into the autoclave.

The temperature of the Autoclave was measured by a K-type thermocouple placed below the assembly inside the autoclave. Referring to Fig. 4.3, the prepreg material was cured according to the manufacturers recommended standard 2–step cure schedule [2] with: $T_1 = 115°C$, $t_1 = 60$ min, $T_2 = 177°C$ and $t_2 = 120$ min.

A pressure of $0.584MPa$ (85 psi) was applied initially, and a vacuum was drawn on the bagged charge. A second, modified 3–step curing schedule suggested by the manufacturer for thicker parts [2], was also applied with: $T_1 = 115°C$, $t_1 = 120$ min, $T_2 = 150°C$, $t_2 = 90$ min, $T_3 = 177°C$ and $t_3 = 240$ min. The same pressure and vacuum were drawn on the bag as above. Five samples were processed in the autoclave using both curing cycles. They were prepared as follows:

**# 2** The 50 layers were laid with debulking after each 10 layers, and the sample was cured using the 2-step curing cycle. 1 layer of perforated release film is applied.

**# 3** The 50 layers were laid with debulking after each 5 layers, and the sample was cured using the 3-step curing cycle. 1 layer of perforated release film is applied.

**# 4** The 50 layers were laid in one shot, and the sample was cured using the 2-step curing cycle. 2 layers of perforated release film are applied to restrict resin flow.

**# 5** The 50 layers were laid with debulking after each 10 layers, and the sample was cured using the 3-step curing cycle. 2 layers of perforated release film are applied to restrict resin flow.

**# 1** The same as sample # 4 with two sensors (thermocouple and dielectric) inserted at points A and B, respectively, as shown in Figure 4.4 (the dielectric

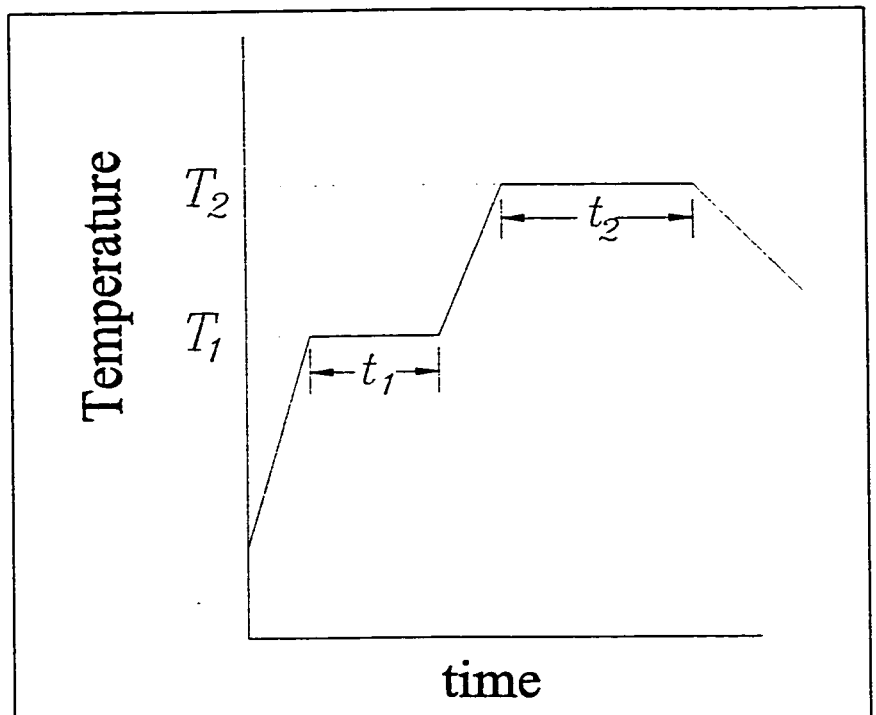


(a) 2–step curing cycle.

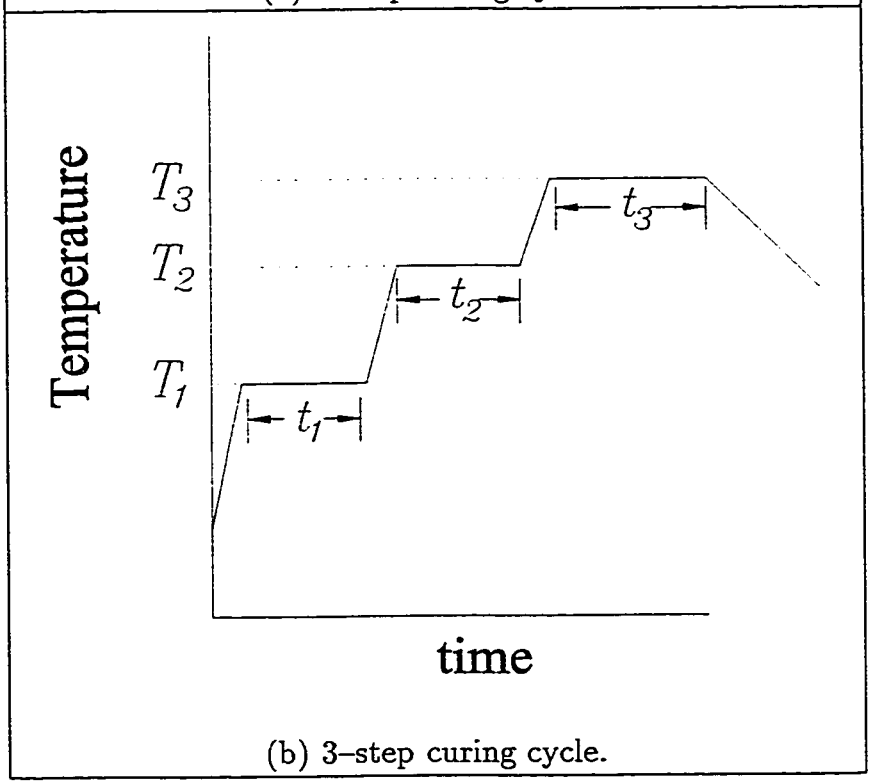


(b) 3–step curing cycle.

Figure 4.3: Processing cure cycles used in 2–step and 3–step cycles.

sensor measures temperature as well).

It was noted during the autoclave processing that the rate of heating was $2.2°C$.

To help in the analysis, an angle $\phi$ and a non-dimensional scale $l$ (in the thickness direction) were defined as shown in Figure 4.4. $l$=0 at the bottom (mold surface), $l$=1/2 at the middle and $l$=1 at the top surface. (For point A: $\phi = 70°$ and $l$=1/2. For point B: $\phi = 45°$ and $l$=1/2.)

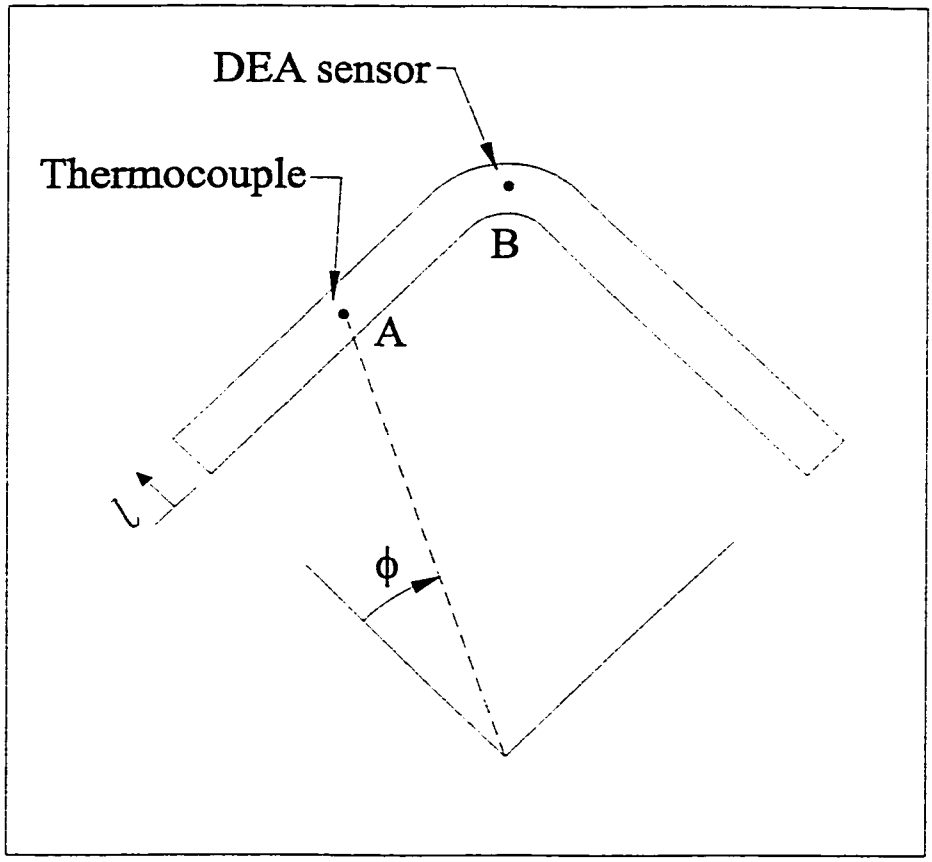


Figure 4.4: Thermocouple A and dielectric sensor B locations for sample # 1.

For sample # 1, the ionic conductivity was measured by a TA Instruments Dielectric Analyzer (DEA) which incorporates technology licensed from Micromet

instruments. A photo of the DEA system is shown in Figure 4.5 and an overview of the specifications is described in Appendix E. Figure 4.6 shows the interface box connected to the remote sensor and the autoclave.

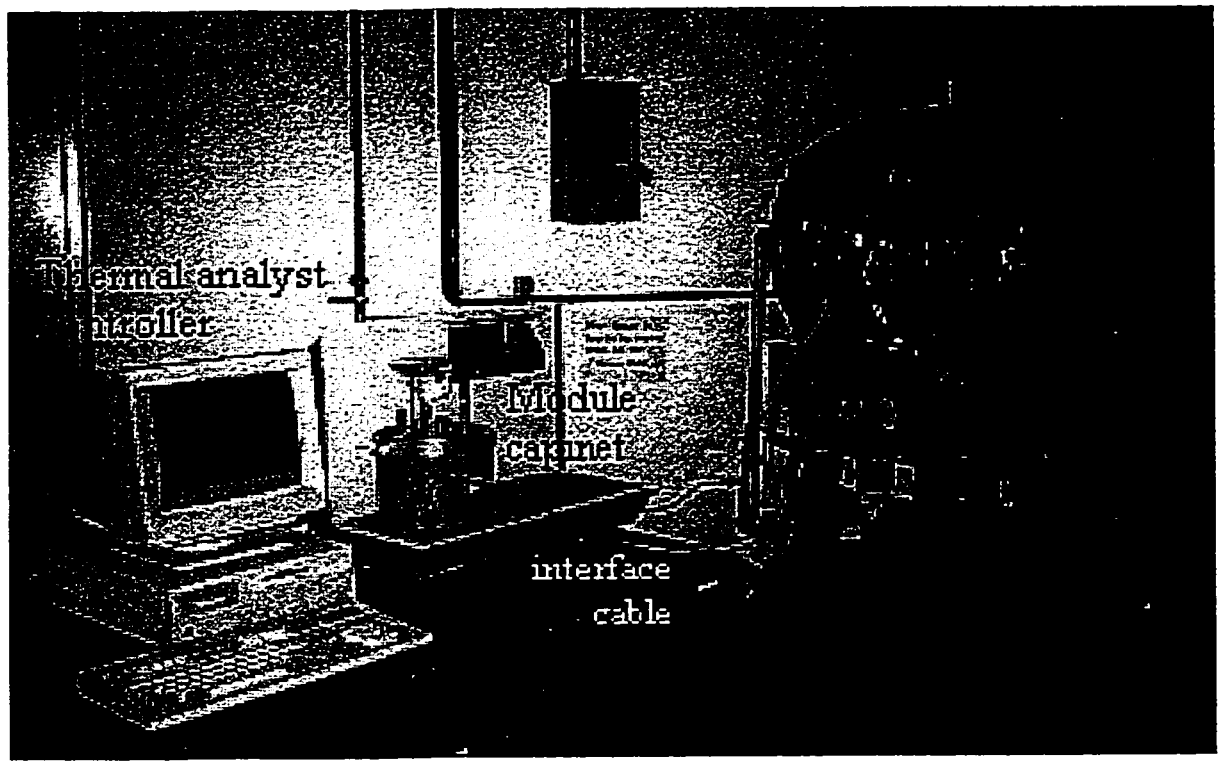


Figure 4.5: Dielectric Analyzer with TA Instruments Thermal Analyst Controller attached to the autoclave.

The type of the sensor used with the DEA was a Micromet Low Conductivity Dielectric remote single surface sensor mounted at point B. A photograph of the sensor is shown in Figure 4.7. The Micromet instrument provides directly four major properties: the permittivity e', the loss factor e", the dissipation factor e"/e', and the ionic conductivity $\sigma^{-1}$.

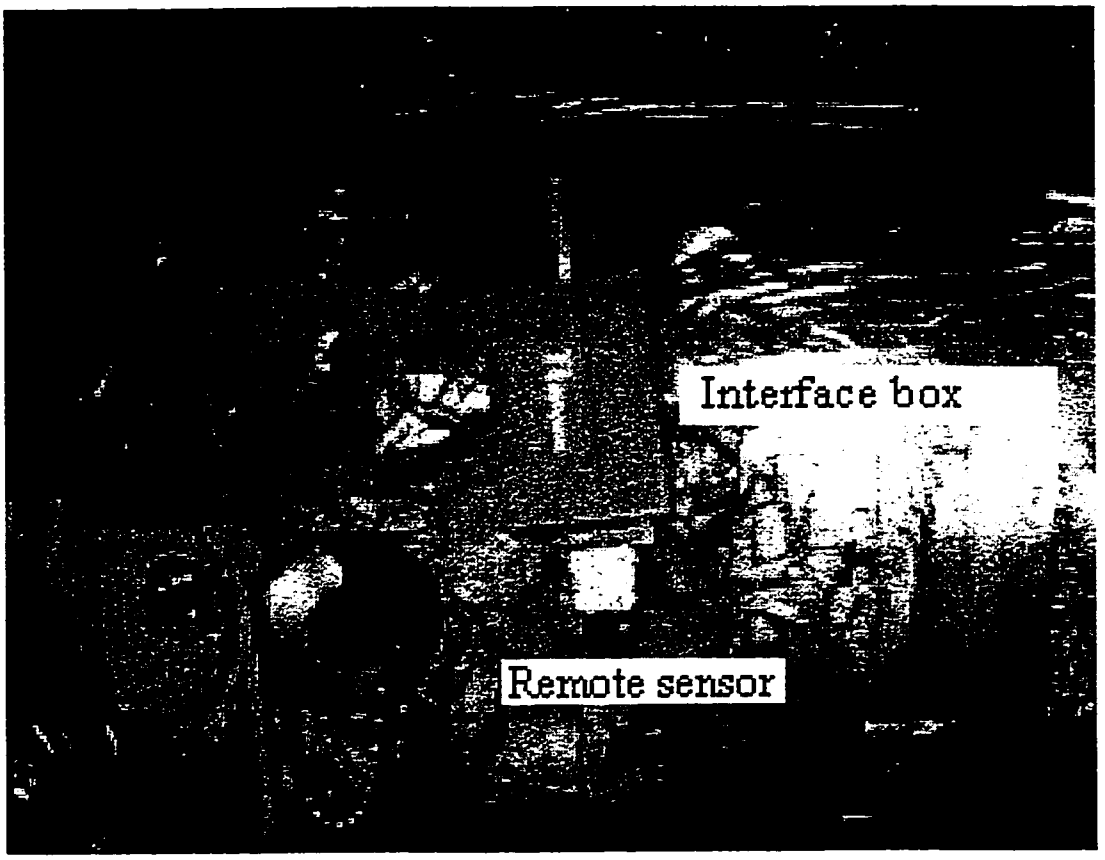


Figure 4.6: The interface box connected to the autoclave through the remote sensor.

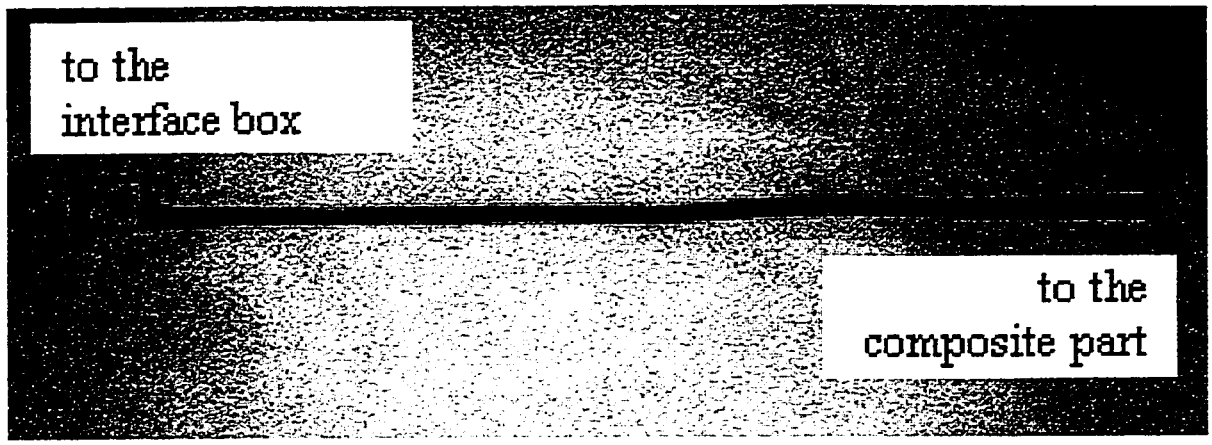


Figure 4.7: Dielectric remote single surface sensor.

In the DEA experiment, pre-selected frequencies in the range between 0.3 and $10^5$ Hz were scanned during experimental measurements to ensure that the data satisfy the conditions of the instrument [37]. Some gaps in the data (shown in the next section) occurred during the first holding temperature and also when the most appropriate frequency was between any of these pre-selected frequencies. However, these gaps were of no concern here since the major interest was in the trend in the data and not in the individual data points. The signals from the sensor were fed into the TA Instrument computer–based thermal analysis controller. The data were stored and processed in this computer. It was noticed that the trend in the ionic conductivity variation with time was similar to that found in references [27] and [28], but the scale was different. The test was repeated on other raw materials and the same results were obtained. The data thus generated are presented later in this chapter. Before discussing the experimental results, computer simulation preparation is presented.

## 4.3 Simulation Model

To verify the experimental results, the simulation code was run on a curved laminate that is divided into $61 \times 21$ mesh [2] (shown in Figure 4.8) with time step taken equal to 1 second. Mesh sizes of $81 \times 31$ and $101 \times 31$ have been simulated and were found to give the same results. The boundary conditions imposed on the different surfaces were as follows:

[2] $m \times n$: m points in $\xi$ direction and n points in $\eta$ direction.

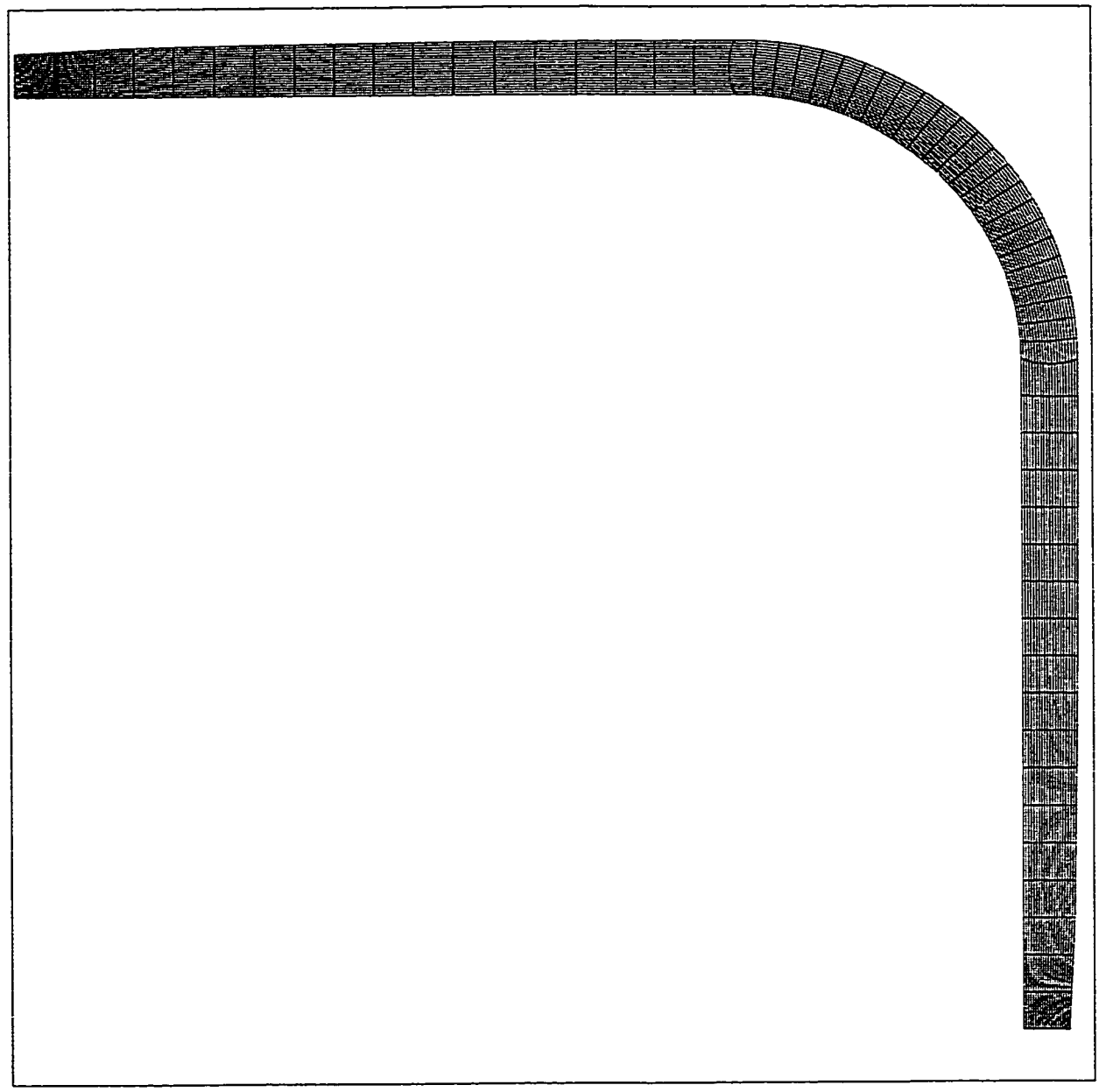

Figure 4.8: Angle–bend geometry mesh

1. Temperature:

   - Top surface: $(\frac{h}{k})_{eff} = 10m^{-1}$
   - Bottom surface: $T = T_a(t)$
   - Side surfaces: $T = T_a(t)$

   where $T_a(t)$ is the autoclave temperature (cure cycle). An experimental parametric study identified the effective heat transfer coefficient $(\frac{h}{k})_{eff}$ to be 10 (1/m) on the top surface of the laminate.

2. Pressure:

   - Top surface:

     $(F_c)_{eff} = 1000$ for 1 perforated release film,

     $(F_c)_{eff} = 100$ for 2 perforated release films.

   - Bottom surface: $\frac{\partial P}{\partial \eta} = 0$
   - Side surfaces: $\frac{\partial P}{\partial \eta} = 0$

   where the autoclave pressure was $P_a = 0.584\ MPa$ and the bag pressure was $P_g = 0\ Pa$. The value for the flow resistance coefficient was chosen based on an experimental parametric study.

## 4.4 Results

### 4.4.1 Experimental Results

The photo in Figure 4.9 shows the tool and some of the samples processed.

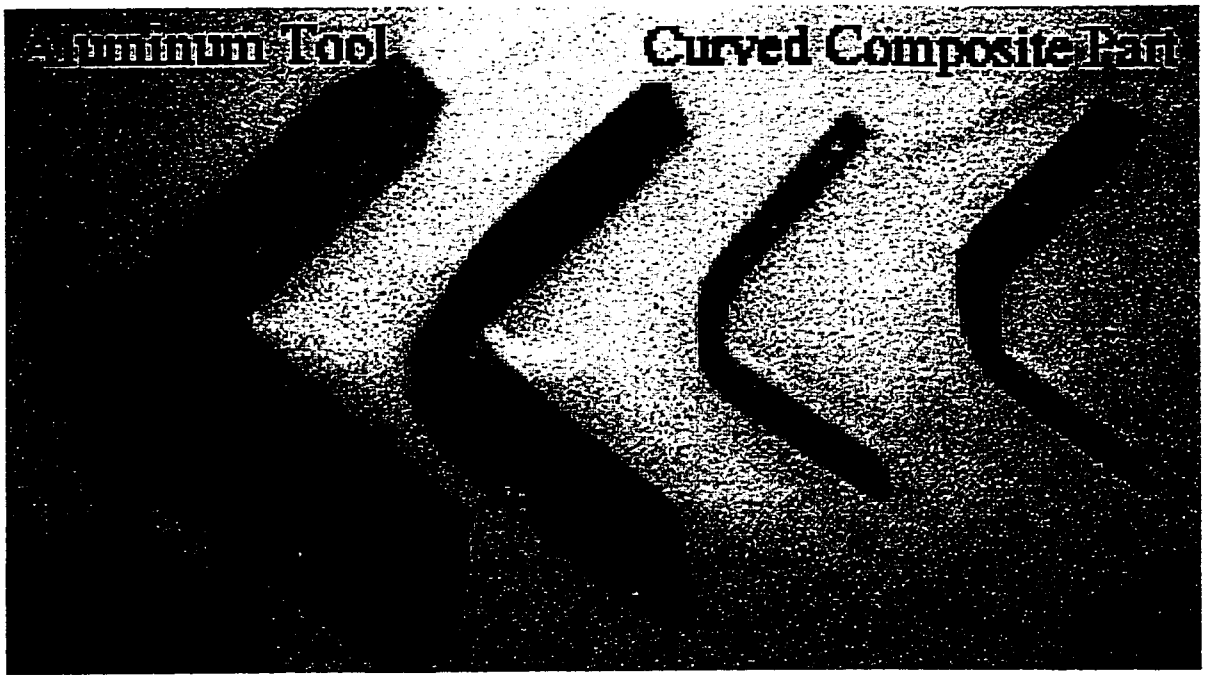


Figure 4.9: Tool and samples photo.

In Figure 4.10, the part thickness variation with the angle $\phi$ is shown for the four samples #2, #3, #4 and #5. Thickness values obtained from model were in good agreement with those obtained from experiment especially for samples #2 and #3. From the figure it is seen that thickness was nonuniform across the part length and this variation increased when the resin flow was restricted (2 perforated

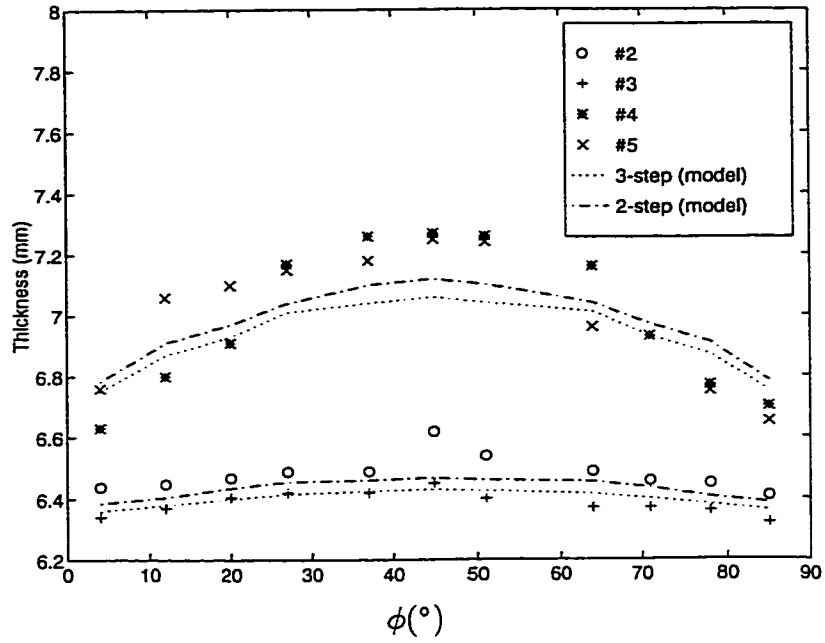


Figure 4.10: Experimental and simulation results for thickness variation at different sections.

release films instead of 1 on the top surface of the laminate). When there is a restriction on resin flow, both 2–step and 3–step cycles produced laminates with similar thicknesses. However, the difference in thickness was more pronounced when no restriction on resin flow is present. Finally, debulking the laminate or not did not seem to have a pronounced effect on the variations in laminate thickness.

These samples were cut length–wise and across–wise to examine the microscopic structure. Five cuts were made cross–wise in samples #4 and #5 to find the fiber volume fraction values. The sections were made at points 2, 4, 6, 4′ and 2′ shown in Figure 4.11. Laminates were polished using sandpaper (grades 320, 400, 600 and 800). The photos in Figure 4.12 show a length–wise microscopic view for

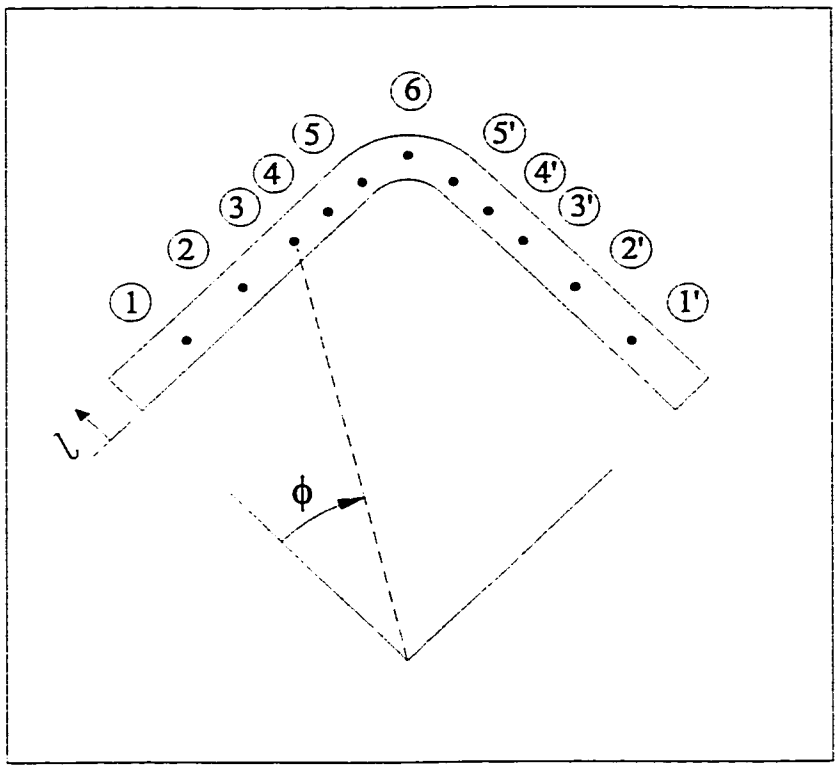


Figure 4.11: Sample geometry and sections numbers

the four samples at section 6 and $l$=1/2. All samples show a resin–rich layer especially between successive layers. The occurrence of this resin–rich layer was the least in sample #3, and was the most in sample #4. However, from Fig. 4.13, which shows the straight–section photomicrographs for all the samples, no resin–rich layers between successive layers were present and all samples look almost the same. Over the whole length, no wrinkling or waviness in fibers was noticed.

To show the cross–section structure, the cross–section photomicrographs at all the sections for sample #4 are shown in Figures 4.14 through 4.18 for $l$=1/2, and in Figures 4.19 through 4.23 for $l$=1 and $l$=0. (Similar photomicrographs were obtained for sample #5.) From these figures, the fiber volume fraction was calculated using $v_{fe} = \frac{A_f}{A}$, where $A_f$ is the total fiber area and $A$ is the area of the selected region of the micrograph. The results at $l$=1/2 are listed in Table 4.1 along with the numerical results $v_{fn}$.

| Section | $v_{fe}$ % | | $v_{fn}$ % | |
|---|---|---|---|---|
| | 2–step # 4 | 3–step # 5 | 2–step | 3–step |
| 2 | 64 | 62.8 | 65 | 66 |
| 4 | 61 | 62 | 63.5 | 64.5 |
| 6 | 58.5 | 60 | 61 | 63.3 |
| 4' | 60 | 63 | 63.5 | 64.5 |
| 2' | 63 | 64.5 | 65 | 66 |

Table 4.1: Experimental ($v_{fe}$) and Numerical ($v_{fn}$) fiber volume fraction values for different sections at $l$=1/2.

Also, Fig 4.24 shows how $v_f$ varies across the thickness for samples # 4 and # 5. It is clear that there is a variation in $v_f$ through the thickness and along the

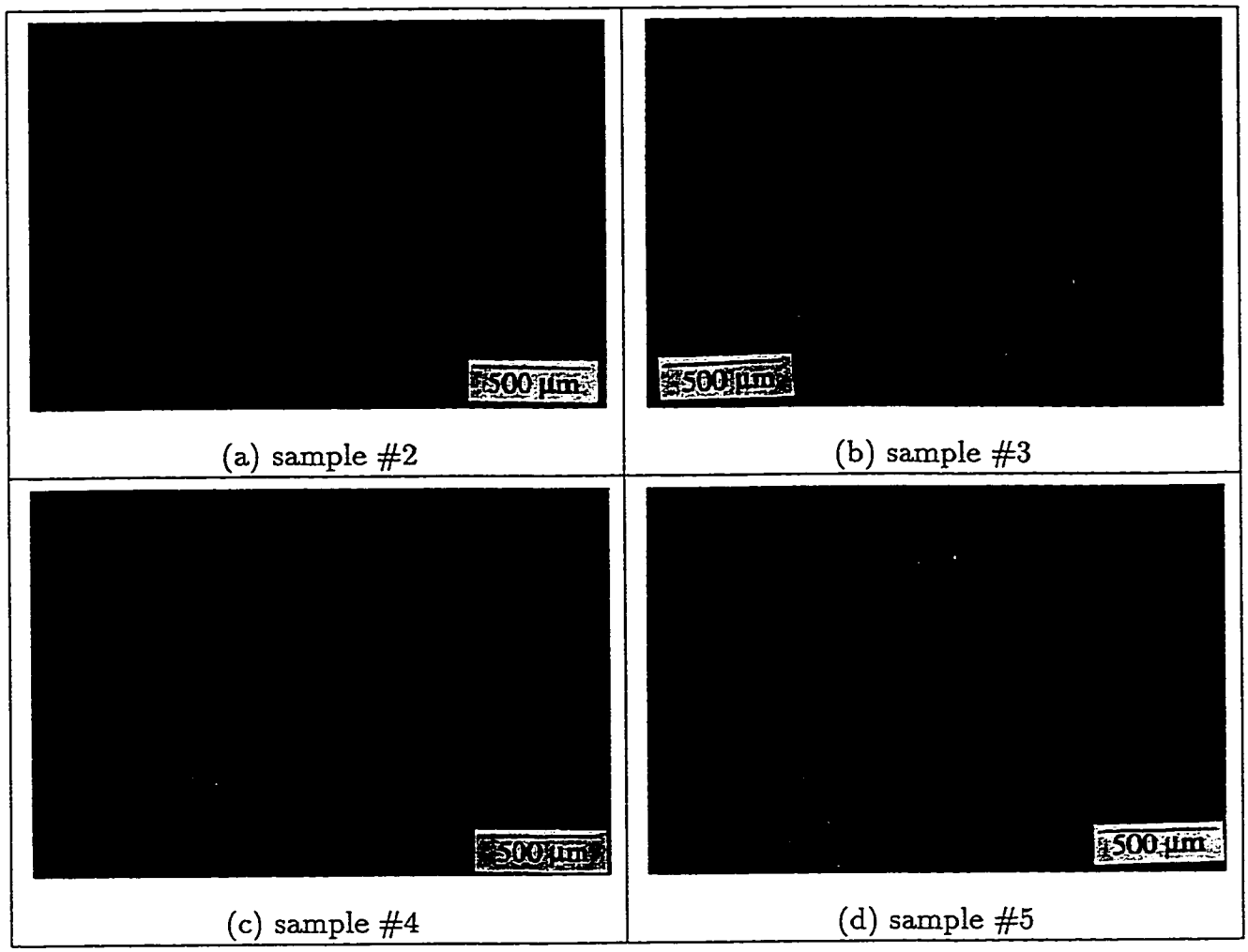


(a) sample #2 (b) sample #3

(c) sample #4 (d) sample #5

Figure 4.12: Length–wise photomicrographs ($50X$) at section 6 and $l$=1/2.

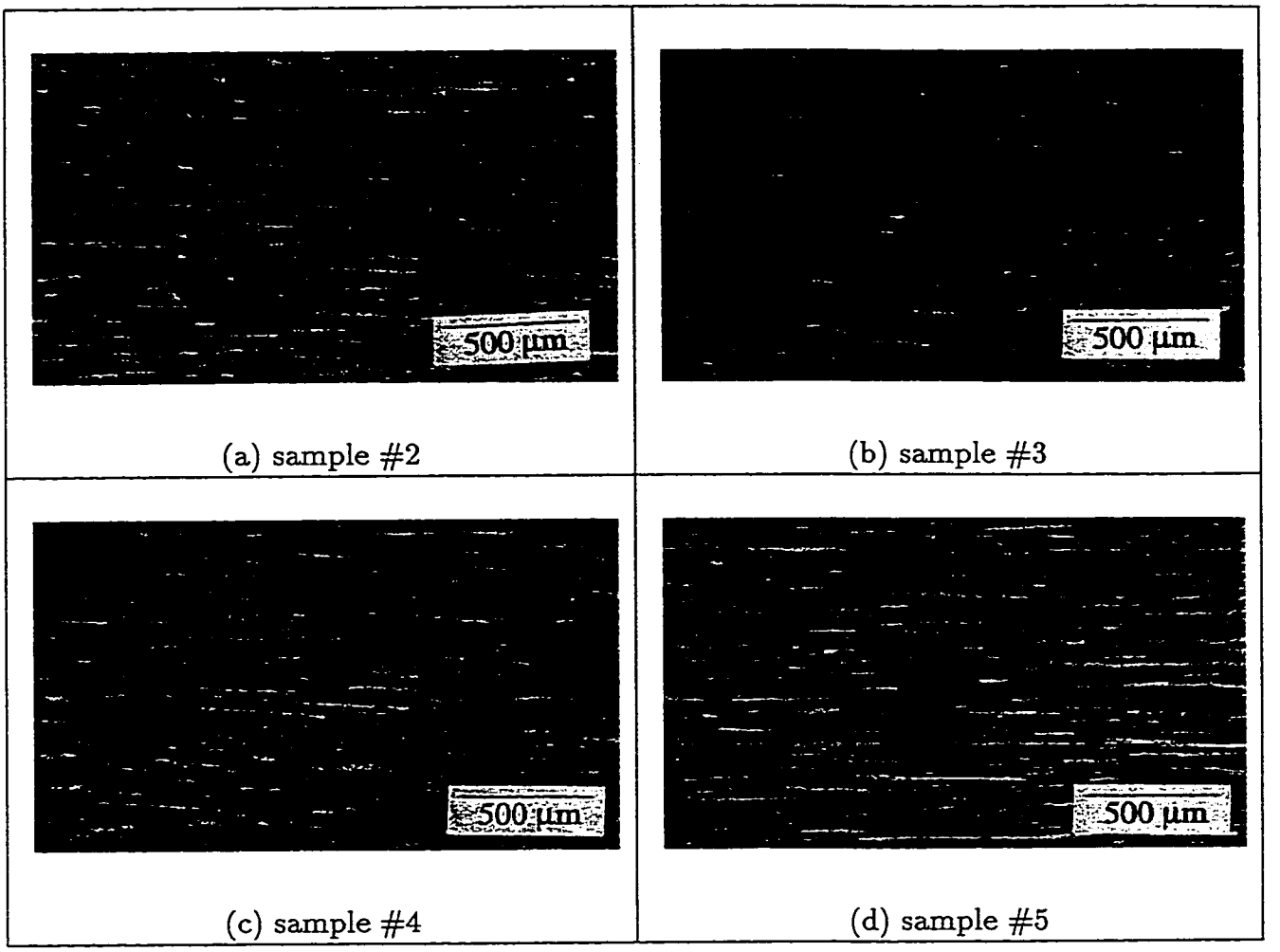


(a) sample #2 (b) sample #3

(c) sample #4 (d) sample #5

Figure 4.13: Length–wise photomicrographs ($50X$) at section 3 and $l$=1/2.

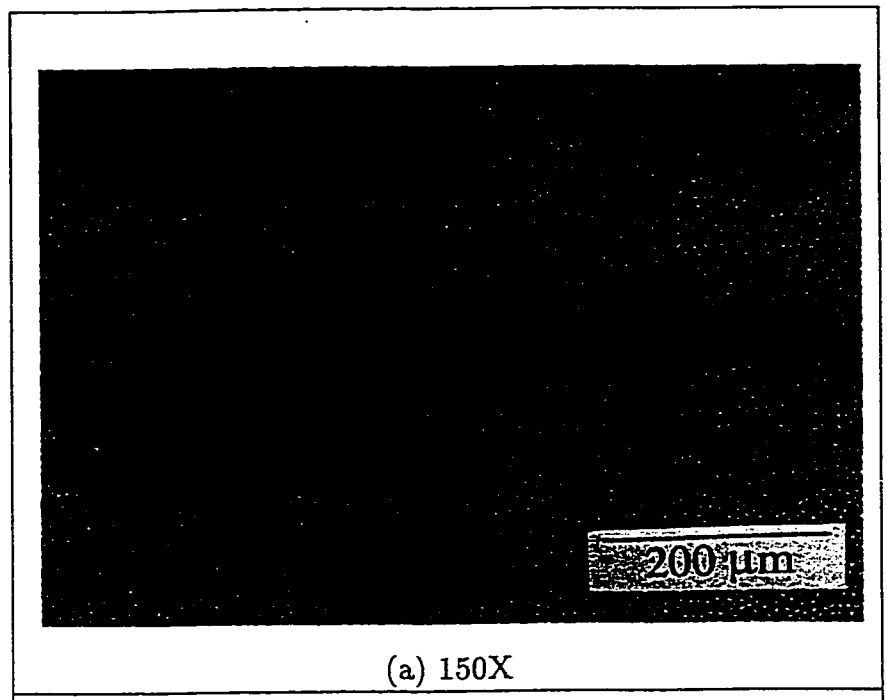


(a) 150X

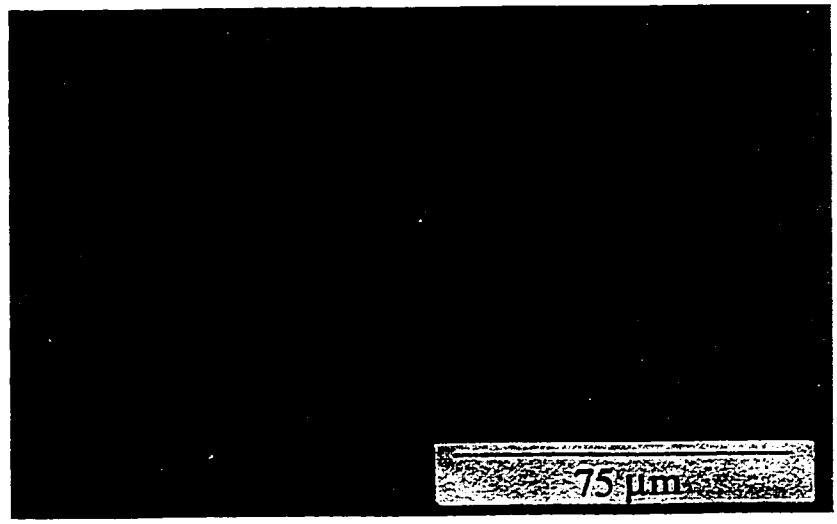


(b) 600X

Figure 4.14: Cross–section photomicrograph at section 2 and $l$=1/2 (sample # 4).

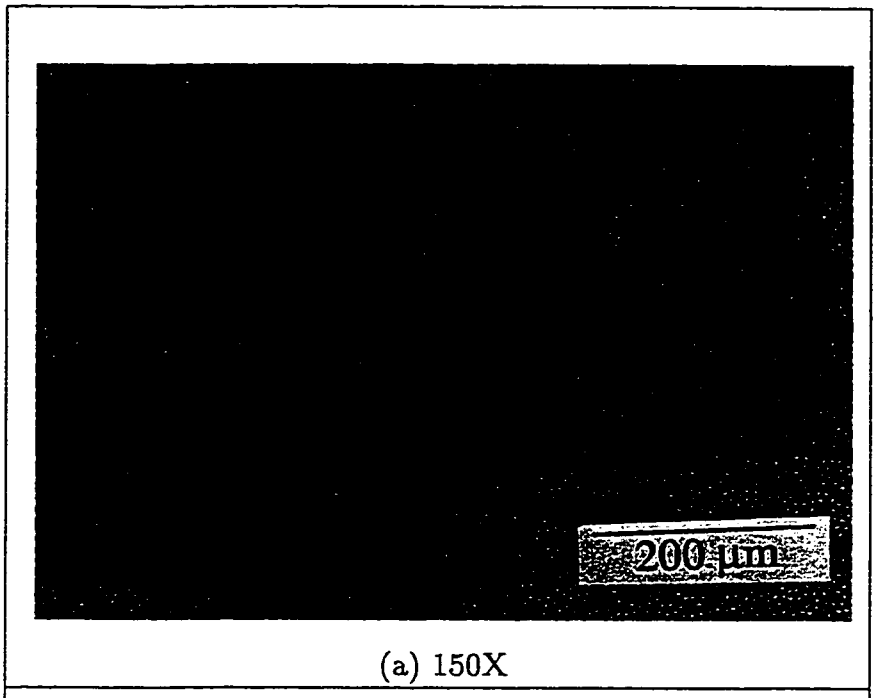


(a) 150X

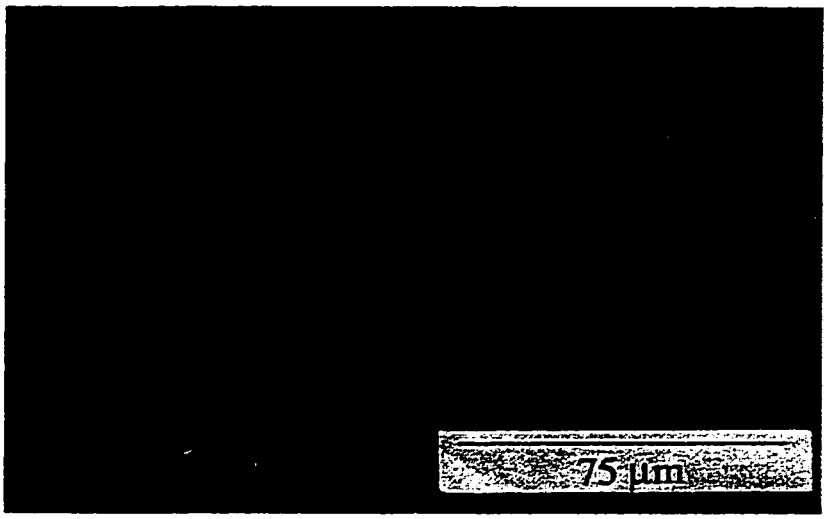


(b) 600X

Figure 4.15: Cross–section photomicrograph at section 4 and $l$=1/2 (sample # 4).

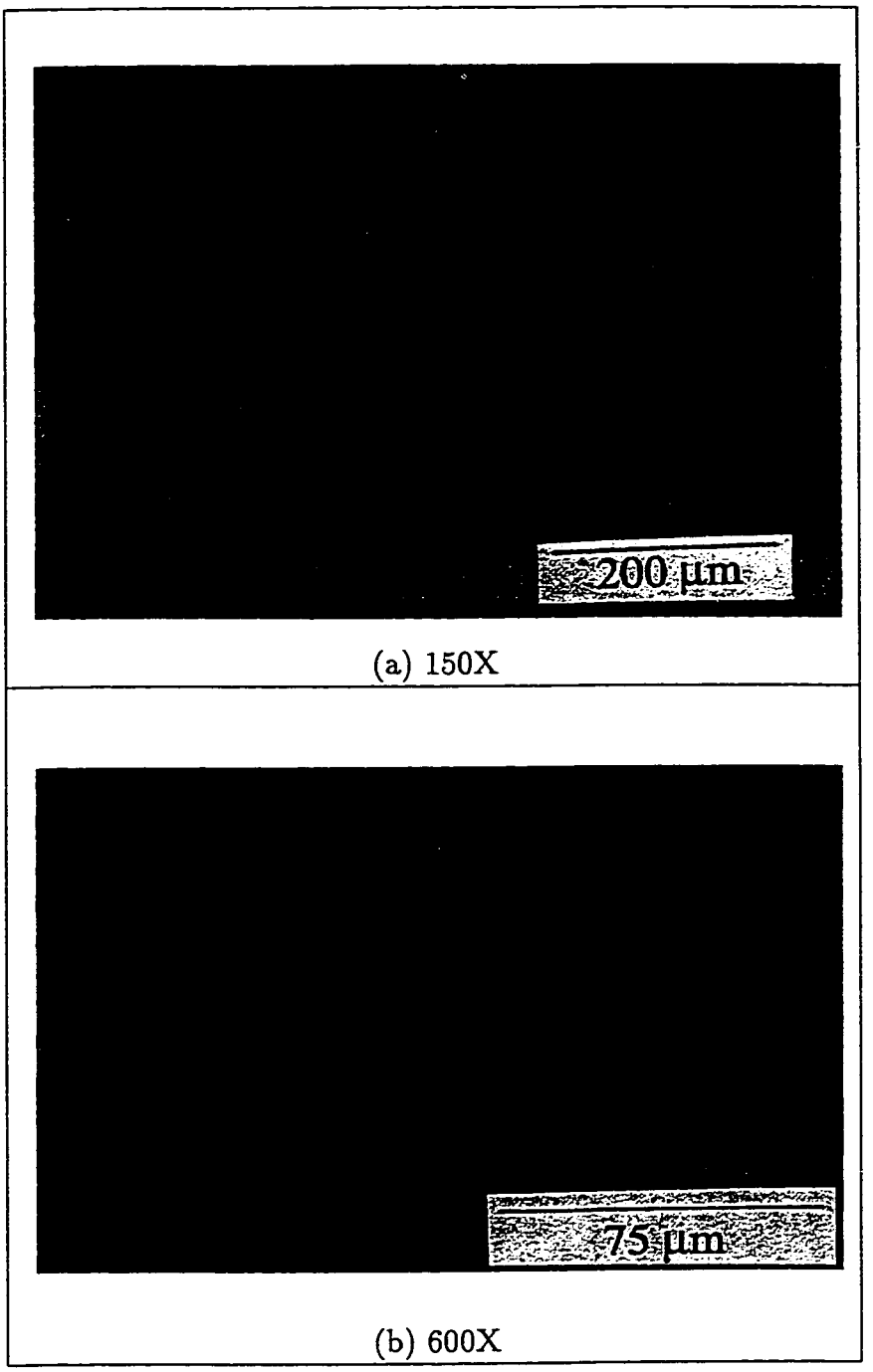


(a) 150X

(b) 600X

Figure 4.16: Cross–section photomicrograph at section 6 and $l$=1/2 (sample # 4).

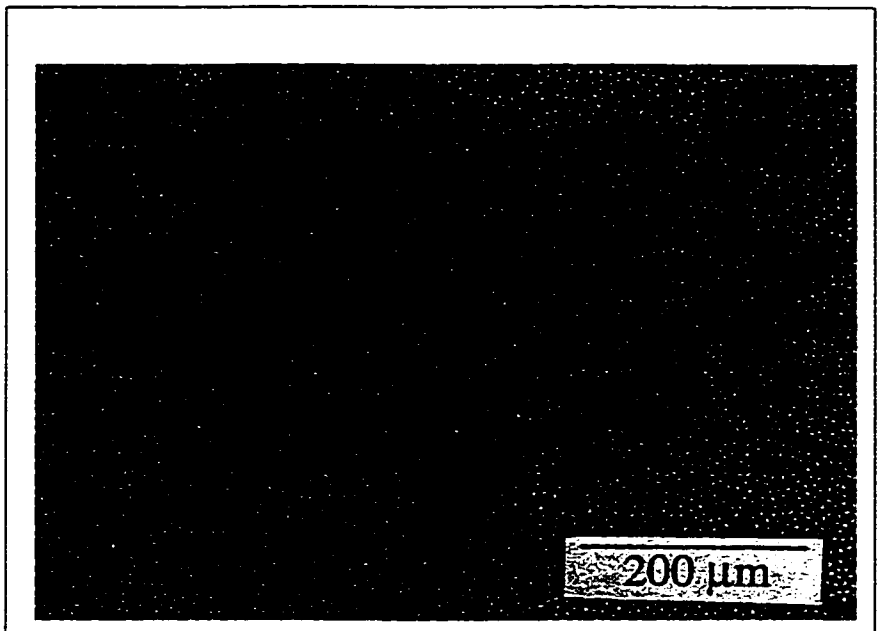


(a) 150X

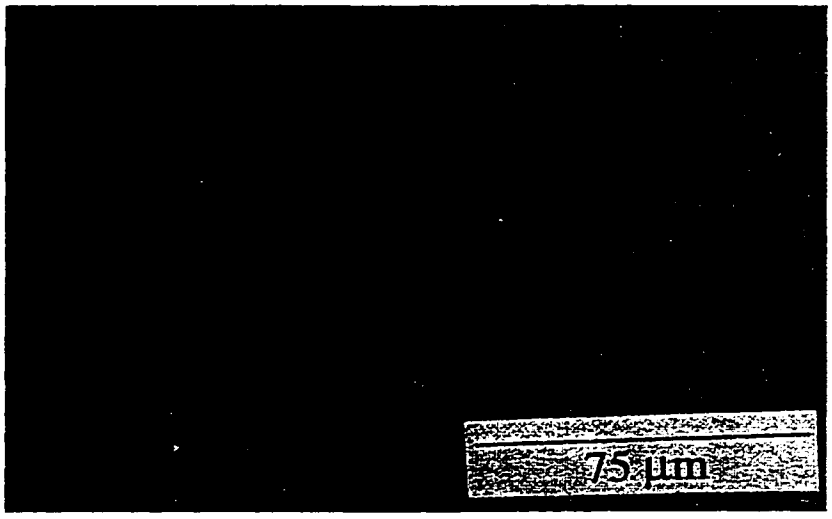


(b) 600X

Figure 4.17: Cross–section photomicrograph at section 4' and $L$=1/2 (sample # 4).

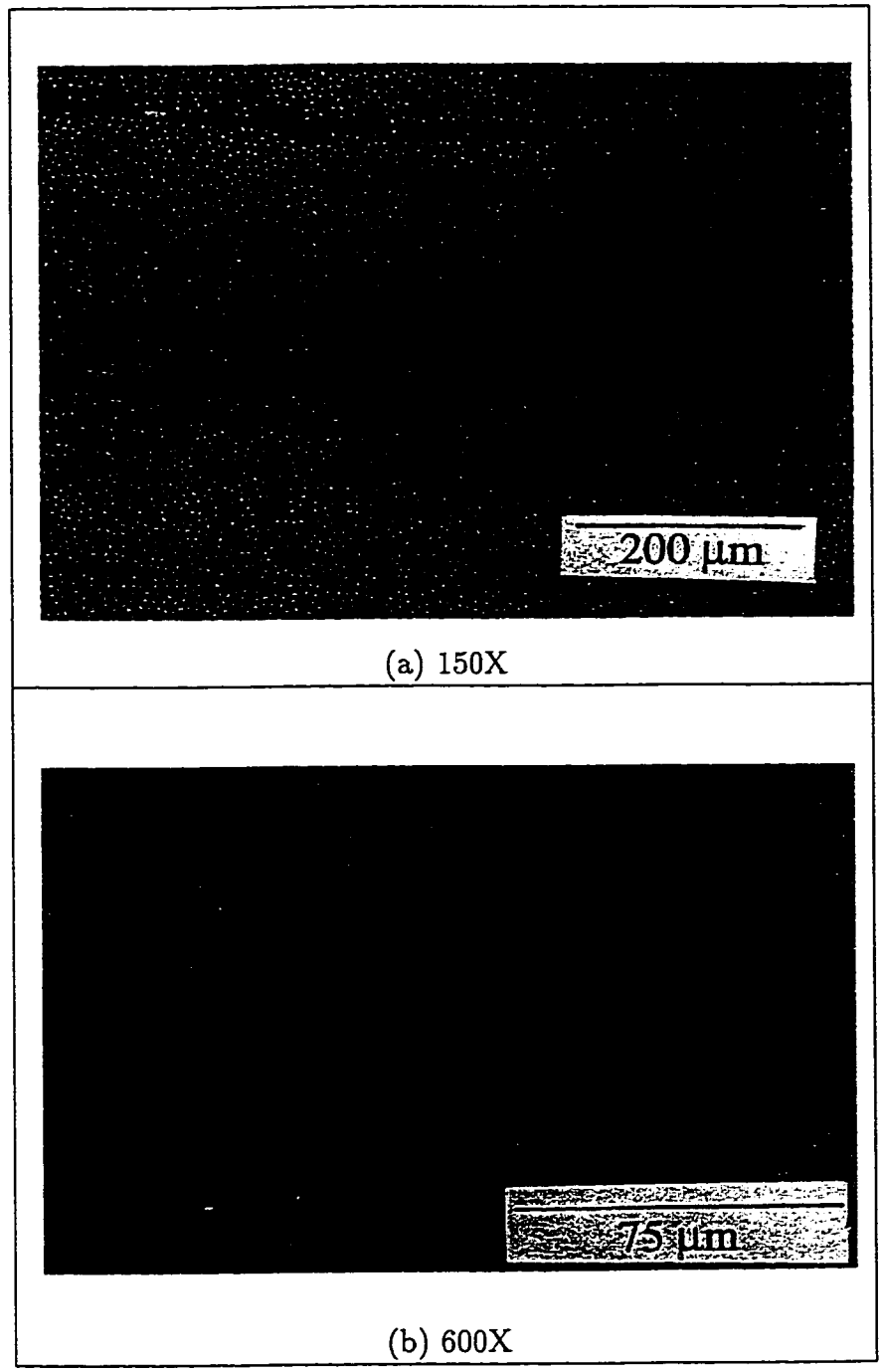


Figure 4.18: Cross–section photomicrograph at section 2' and $l$=1/2 (sample # 4).

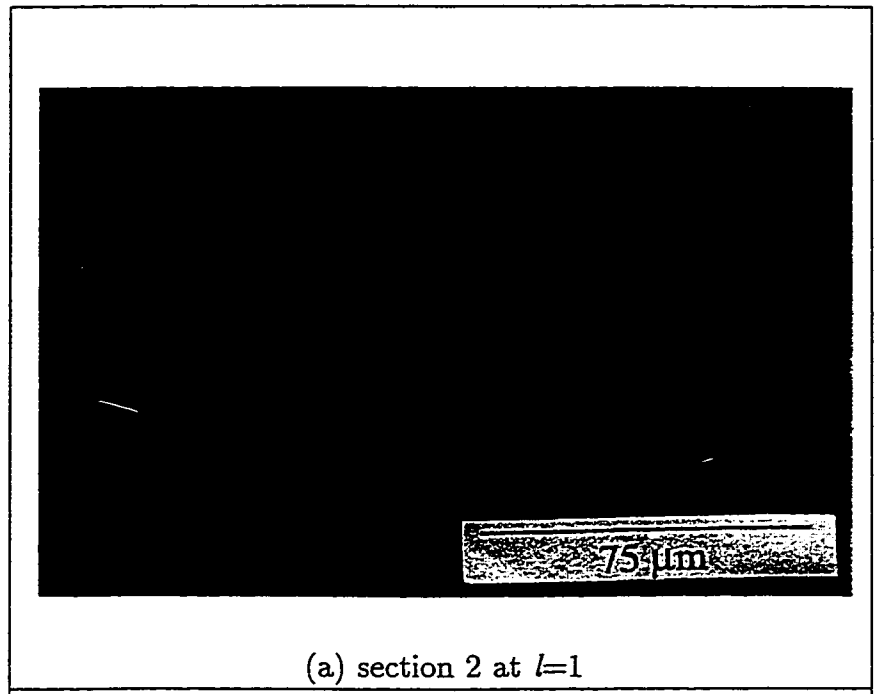


(a) section 2 at $l$=1

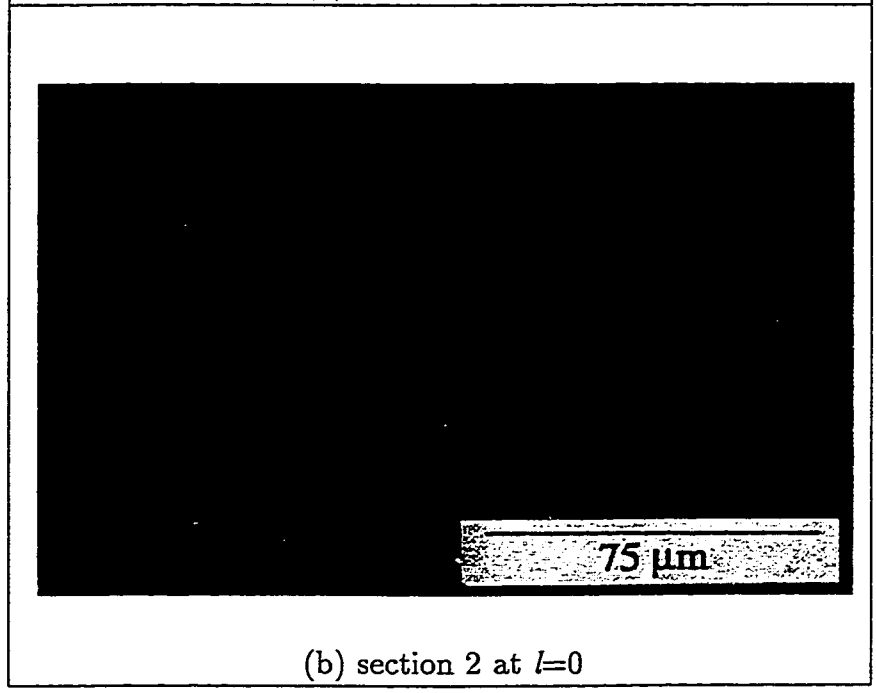


(b) section 2 at $l$=0

Figure 4.19: Cross–section photomicrograph ($600X$) at section 2 (sample # 4).

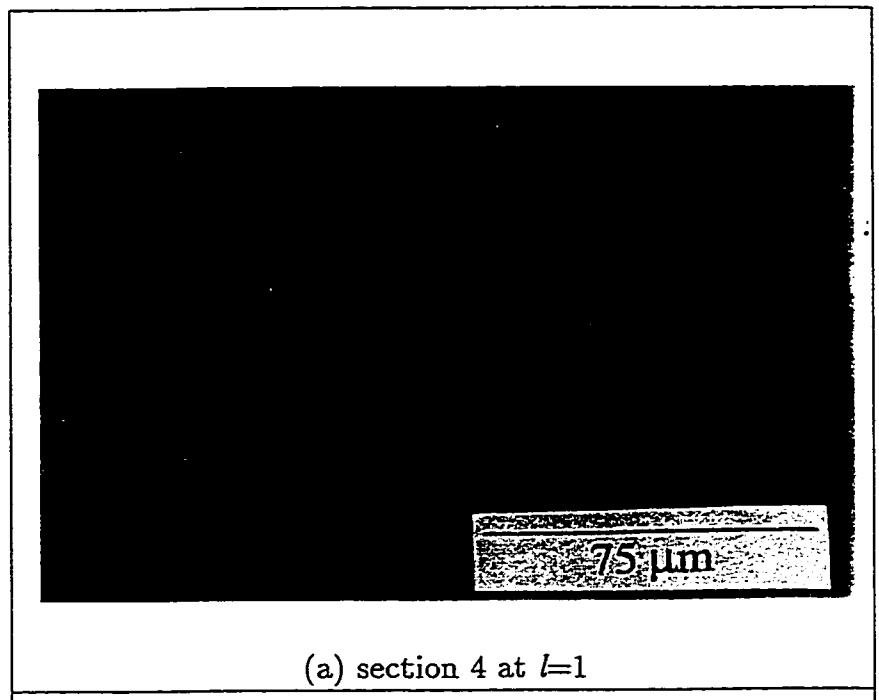


(a) section 4 at $l$=1

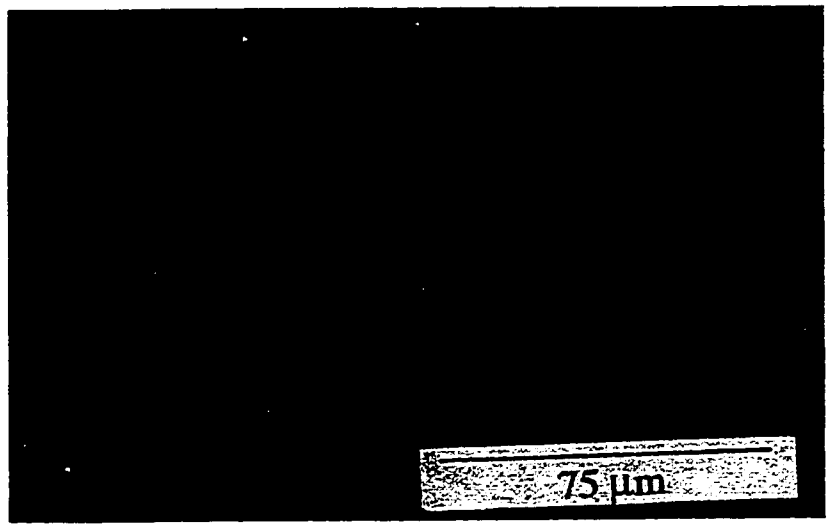


(b) section 4 at $l$=0

Figure 4.20: Cross–section photomicrograph ($600X$) at section 4 (sample # 4).

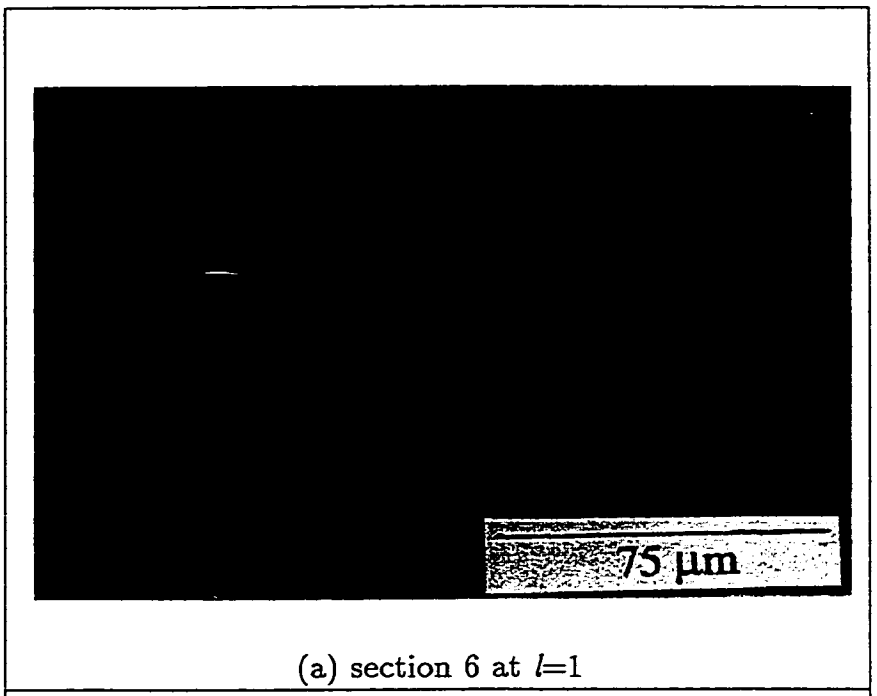


(a) section 6 at $l$=1

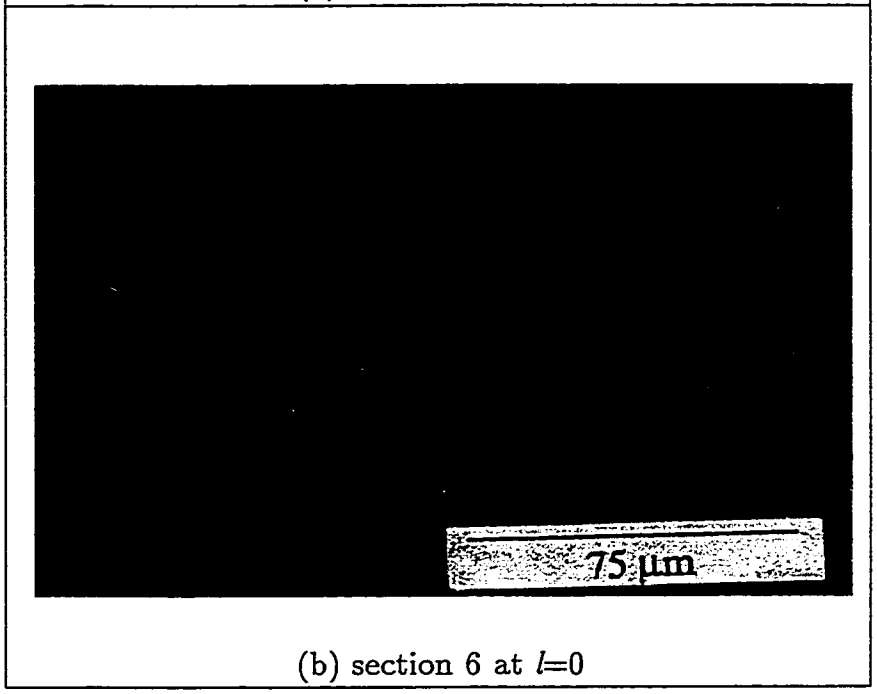


(b) section 6 at $l$=0

Figure 4.21: Cross–section photomicrograph ($600X$) at section 6 (sample # 4).

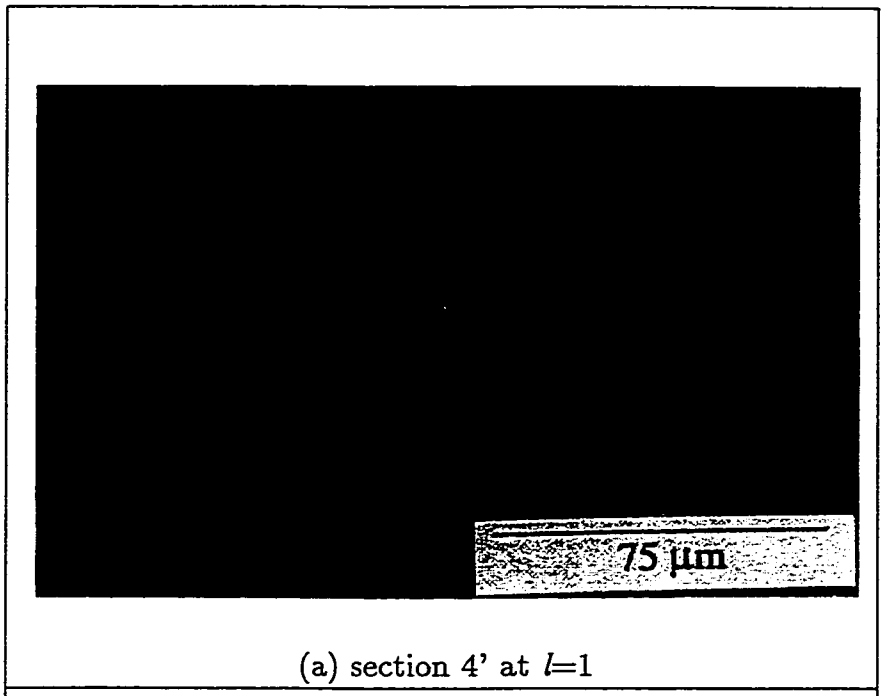


(a) section 4' at $l$=1

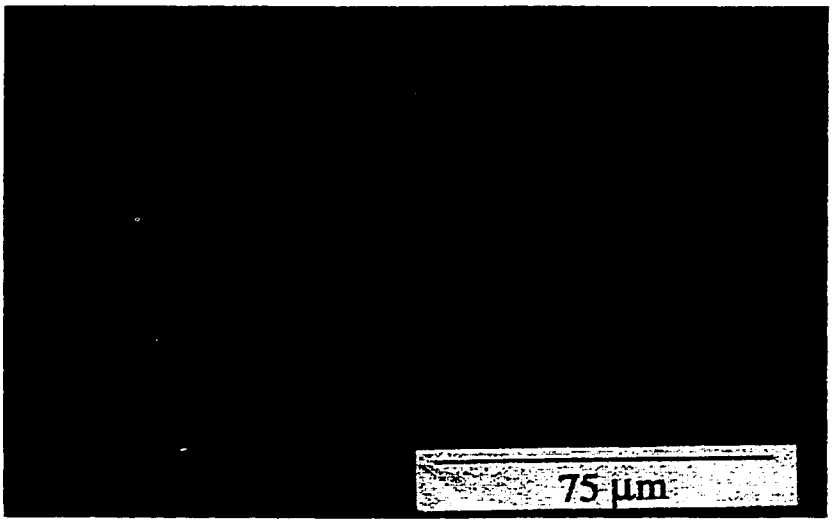


(b) section 4' at $l$=0

Figure 4.22: Cross–section photomicrograph ($600X$) at section 4' (sample # 4).

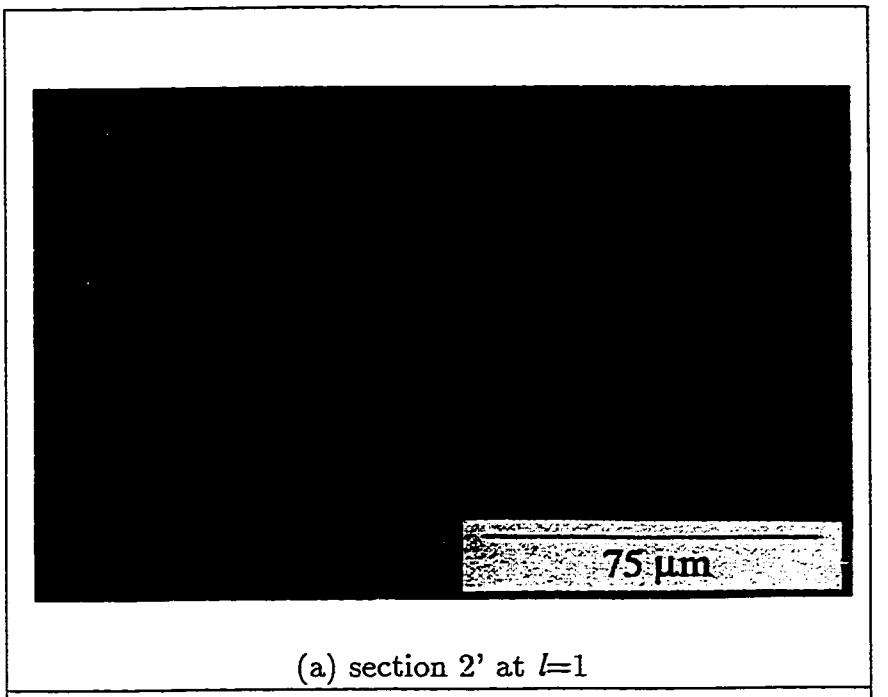


(a) section 2' at $l$=1

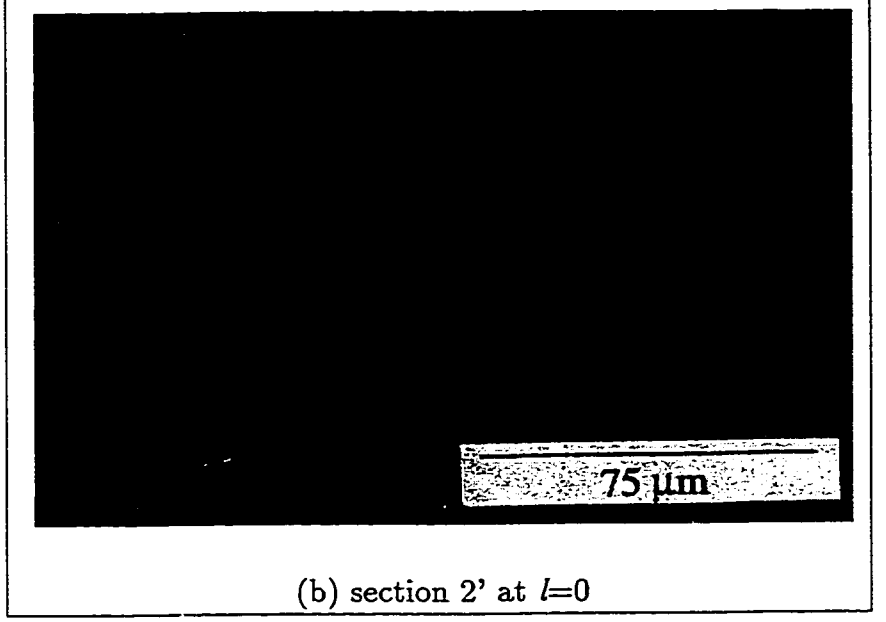


(b) section 2' at $l$=0

Figure 4.23: Cross–section photomicrograph ($600X$) at section 2' (sample # 4).

length. The high $v_f$ value at the top surface is due to the presence of the bleeder layer, and the low $v_f$ value at the bottom surface is due to the presence of the impermeable mold surface. This variation increases as we move from the straight sections to the curved bend.

Figure 4.25 shows the autoclave temperature and the temperatures obtained at points A and B from model and experiment.

Finally, the enclosed angle of the final part was measured with a profile projector measurement machine [3] to investigate the "Spring In" phenomenon. Table 4.2 lists the enclosed angle for the four samples. It is clear that small dimensional changes have occurred to the processed parts as a result of the mismatch between in–plane and out–of–plane thermal expansion coefficients.

| Part # | 2 | 3 | 4 | 5 |
|---|---|---|---|---|
| Enclosed angle (°) | 89.35 | 89.58 | 89.23 | 89.33 |

Table 4.2: Enclosed angle results

### 4.4.2 Numerical Results

In the simulation model, the 2–step curing cycle was applied to simulate processing of sample #4. The temperature and pressure boundary conditions are the same as explained in section 4.3 (with 2 perforated release films). Figure 4.26 shows the temperature, and viscosity variations during processing at points A and B. Also, thickness changes and degree of cure variations for the laminate at points A and B

[3] A product of Mitutoyo.

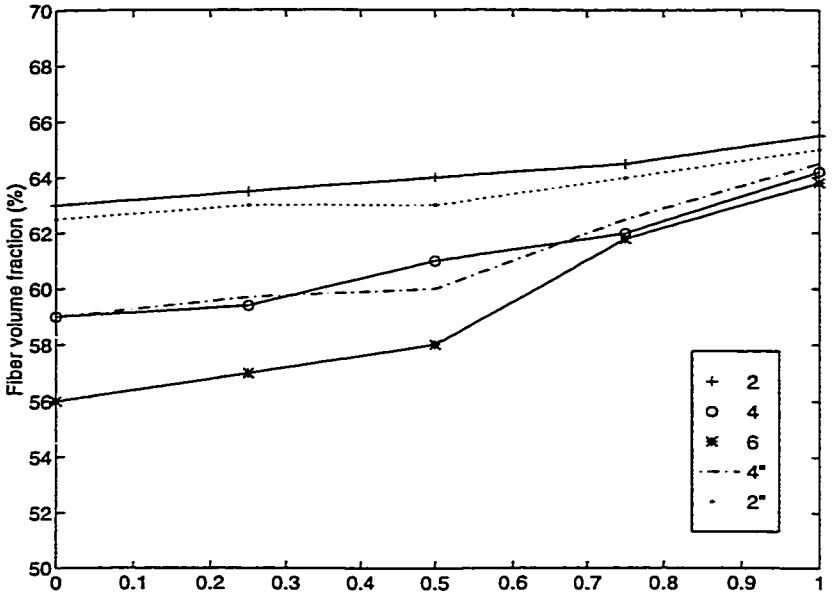


$l$

(a) Sample #4

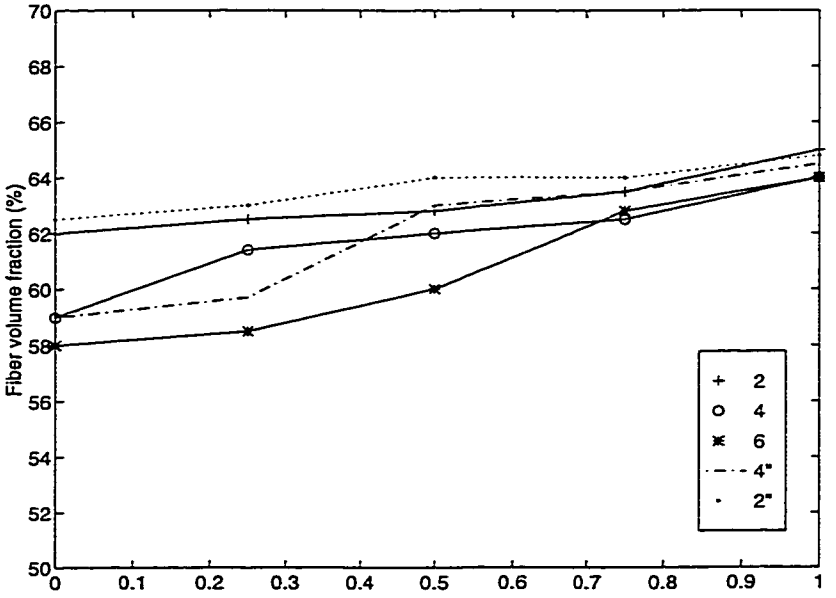


$l$

(b) Sample #5

Figure 4.24: $v_f$ variation across the thickness obtained from experiment for samples #4 and #5.

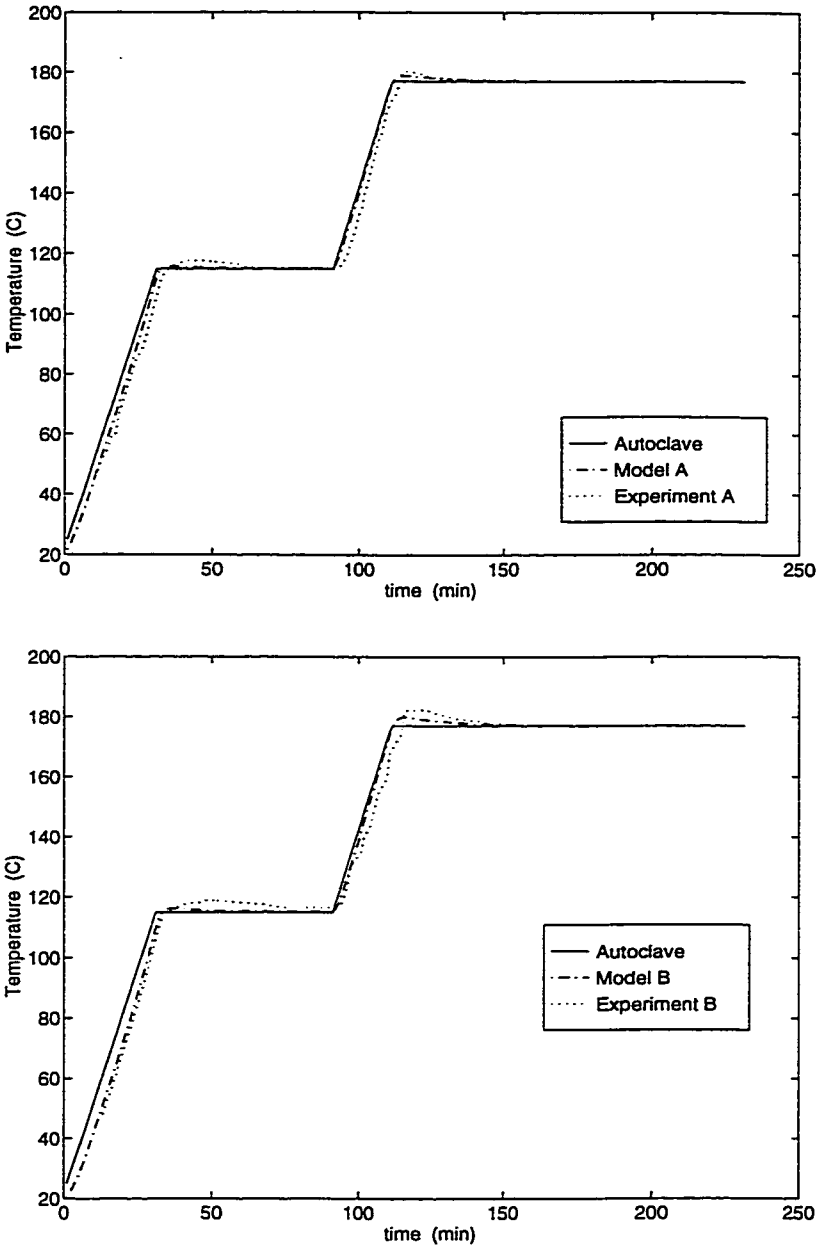


Figure 4.25: Experimental and model temperature variations obtained for thermocouple (A) and sensor (B).

are shown in Figure 4.27.

Figures 4.28 and 4.29 show the fiber volume fraction distribution obtained from simulation $v_{fn}$ for samples #4 and #5 using the 2–step and 3–step cycles, respectively. Again, as in the case for thickness variation, the $v_{fn}$ values obtained from experiment and simulation are in good agreement.

## 4.5 DEA Analysis

To calculate the degree of cure using the experimental data obtained from the DEA measurements for sample #1, Day's method was used [27]. In this method, a *Cure Index* that is comparable to the degree of cure was calculated. According to Maffezzoli et al. [39], high frequencies contribute more to ionic conductivity during polymerization (start of cure) while low frequencies contribute more as curing proceeds. The log(conductivity) variation with time is shown in Figure 4.30, and its variation with temperature is shown in Figure 4.31. The data shows that dielectric measurements are sensitive to the changes occurring within the medium. Ionic conductivity first starts to increase from point a to b because of epoxy resin softening. After that, from point b to c, the curve displays a decrease of ionic conductivity, i.e., a lowering of ionic mobility, which can be easily explained by an increase of viscosity in the medium. This decrease continues to the time when the second ramp (heating) starts (at point c), where ionic conductivity starts to increase due to the decrease in viscosity. The conductivity increases until the temperature reaches a

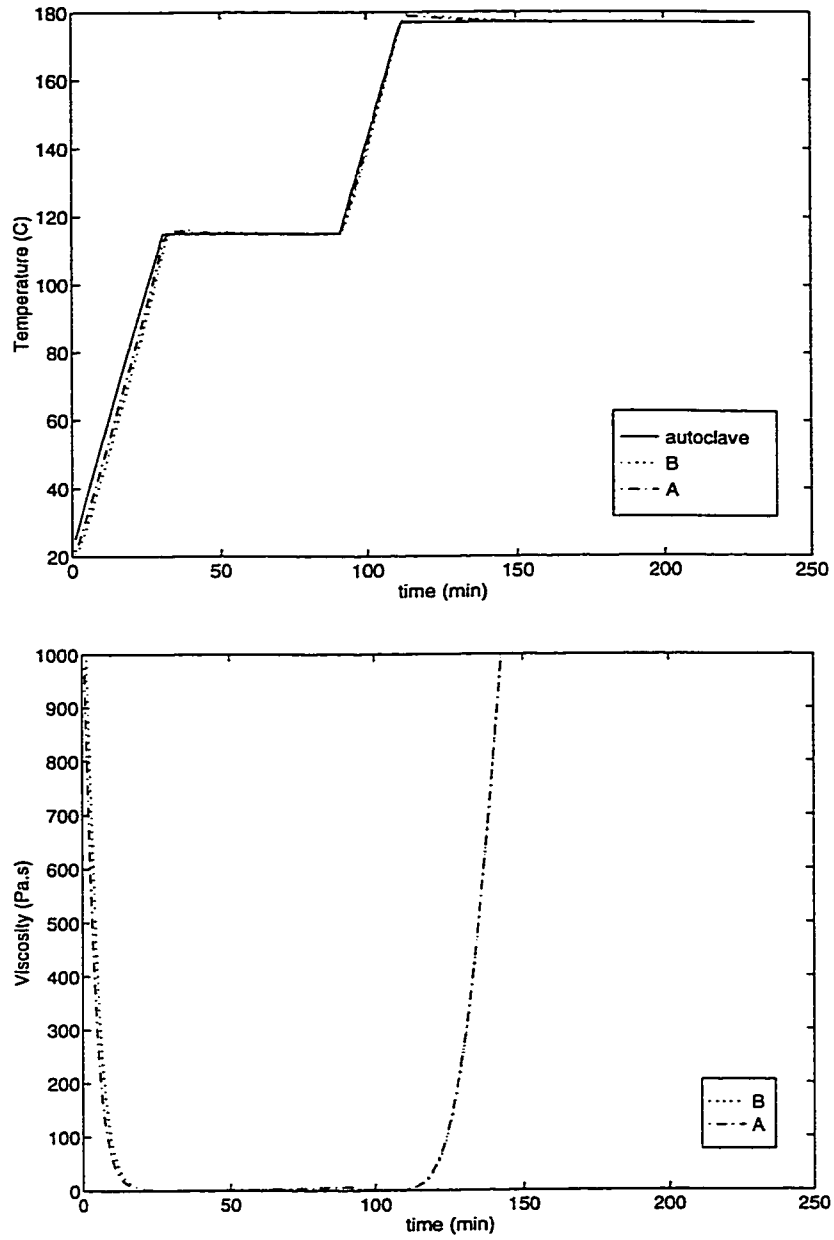


Figure 4.26: Simulation results for temperature and viscosity change for sample #4.

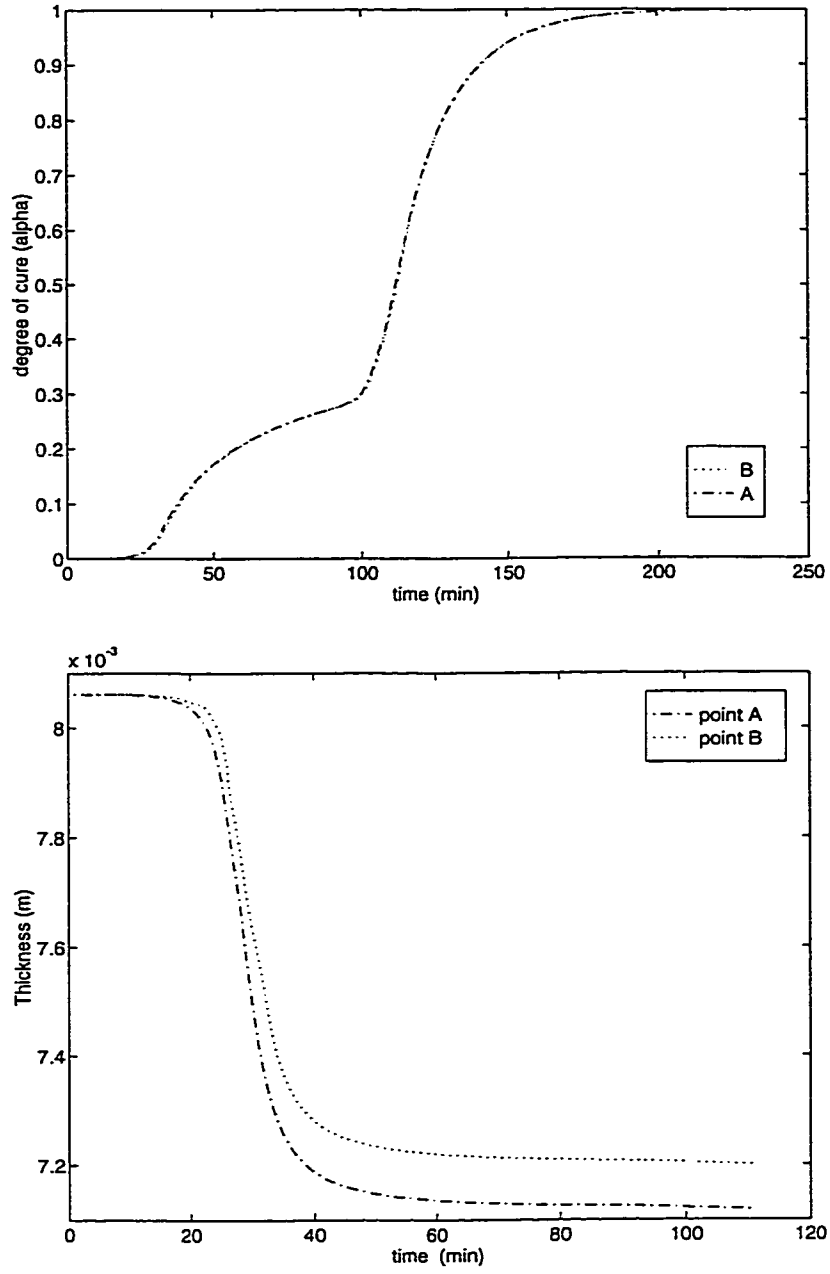


Figure 4.27: Simulation results for degree of cure and thickness change for sample #4.

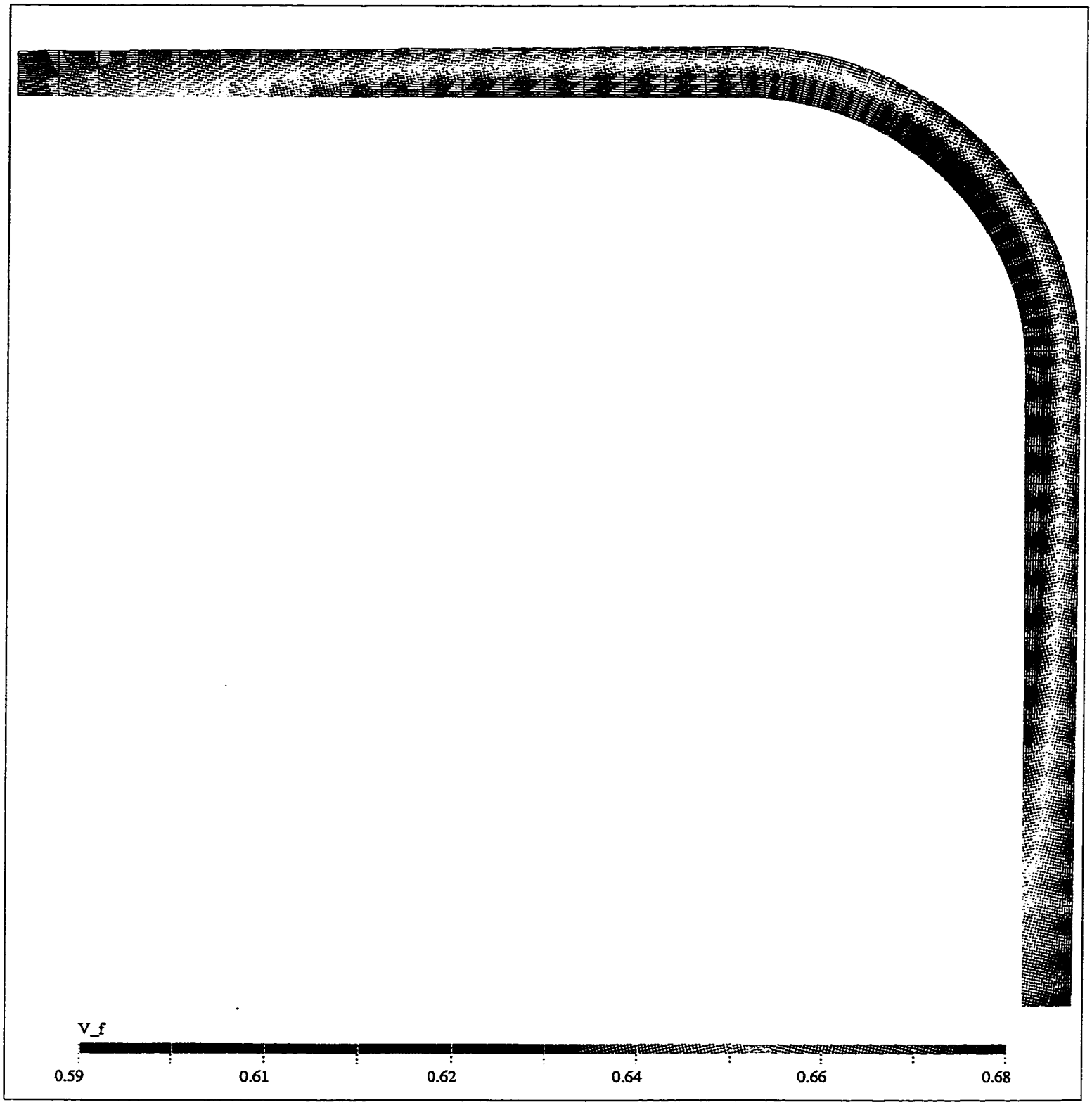


Figure 4.28: Fiber volume fraction distribution across the thickness obtained for the 2–step curing cycle (sample #4).

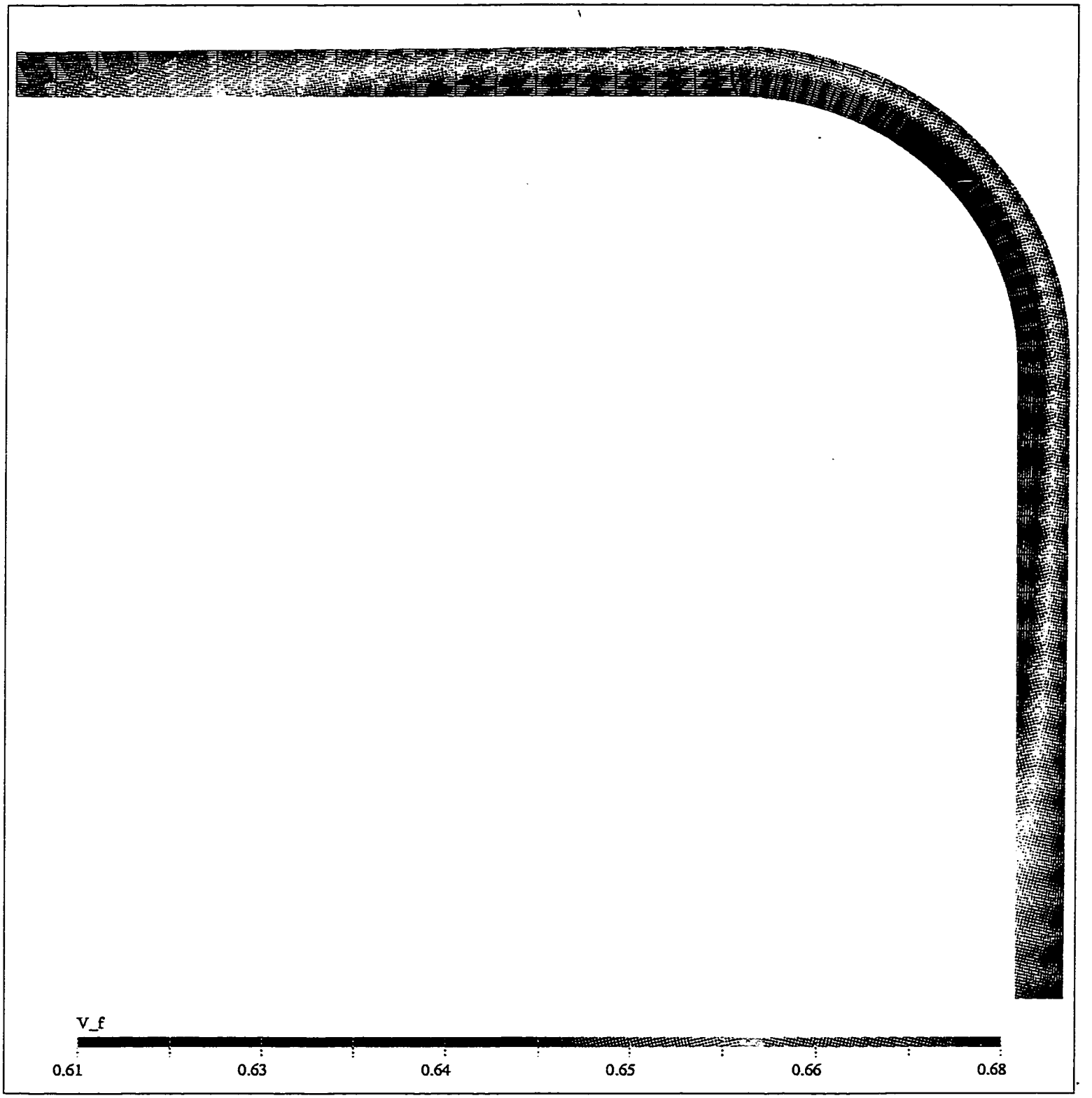


Figure 4.29: Fiber volume fraction distribution across the thickness obtained for the 3–step curing cycle (sample #5).

point at which the final cross–linking goes off (point d) and leads to a decrease in ionic mobility and consequently in the ionic conductivity (from point d to e).

To correlate the dielectric response during cure to the reaction kinetics, the un–cure (0%) and cure (100%) resin equations should be determined first. From the data, the following 0% and 100% temperature dependencies were estimated:

$$\begin{aligned} 0\%\ (\text{un}-\text{cured}): &\quad LC = 0.0728 * T - 1.8118 \\ 100\%\quad (\text{cured}): &\quad LC = 0.0210 * T - 2.3477 \end{aligned} \tag{4.1}$$

where $LC$ is log conductivity and $T$ is temperature in $^{\circ}C$ at a given instant. Then, the cure index can be calculated from:

$$\text{Cure Index} = \frac{LC \qquad -(0.0728 * T - 1.8118)}{(0.0210 * T - 2.3477) - (0.0728 * T - 1.8118)} \tag{4.2}$$

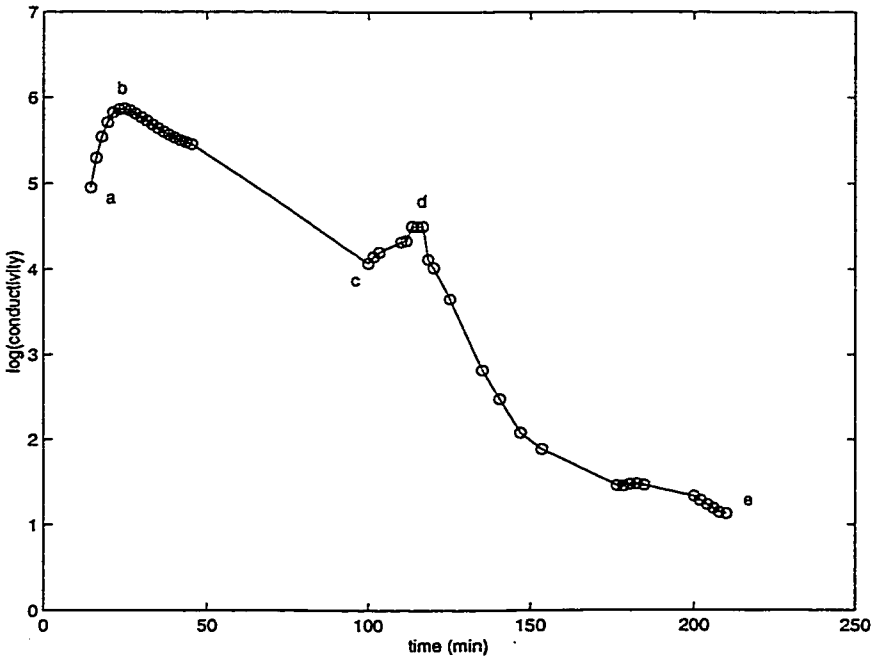


Figure 4.30: log(Conductivity) vs time obtained from experimental results for sample #1.

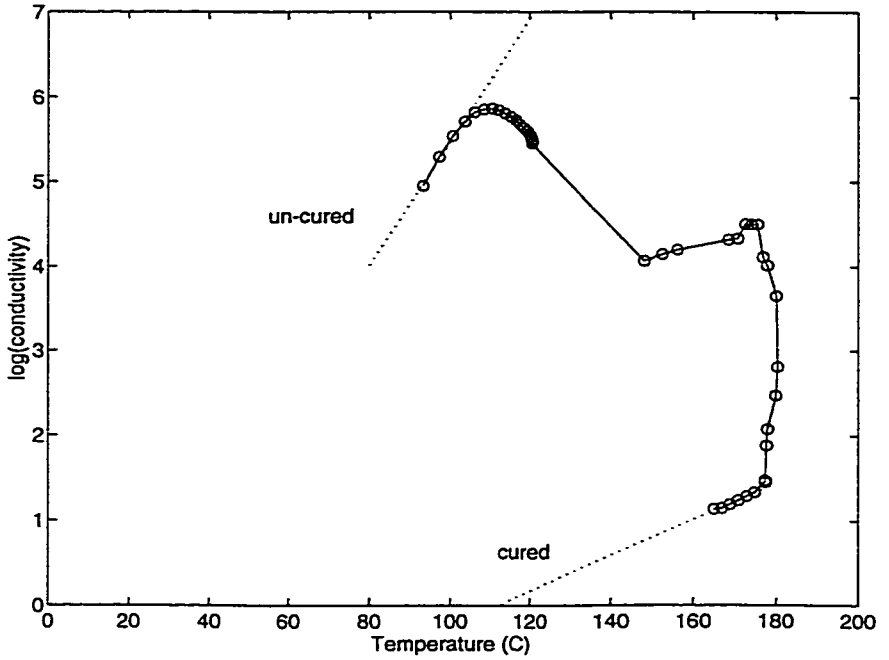


Figure 4.31: log(Conductivity) vs temperature obtained from experimental results for sample #1.

The comparison between the cure index and the degree of cure $\alpha$ obtained from simulation is shown in Figure 4.32. The cure index curve has a shape that is similar to the degree of cure. It exhibits a slow increase near the end of cure indicating slow but continuing reaction [27]. The experiment and simulation compare well at the start of cure but are slightly different at the end.

Also, in Figure 4.33(a), the modified ionic conductivity ($\frac{1}{log(cond)}$) is plotted against time. The modified ionic conductivity is used because it exhibits similar trends as the viscosity. In Figure 4.33(b), viscosity was re–plotted on a log scale for comparison. It is seen that the calculated viscosity reaches a minimum at about the same time as the measured modified ionic conductivity.

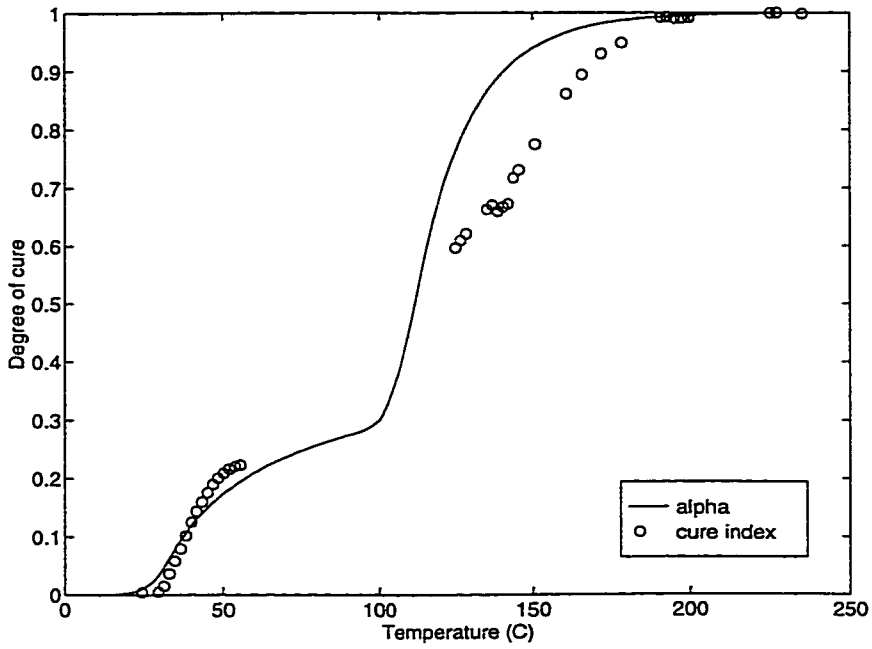


Figure 4.32: Degree of cure variation obtained from experiment and model.

## 4.6 Corner Strength Experiment

Four test specimens were prepared from the four cured samples in order to test their strength. Figure 4.34 shows the test specimen and the test setup. The specimens were pulled apart by force $F$ using a displacement rate–controlled MTS machine (rate $= 5mm/min$).

Figures 4.35 to 4.38 show the load–displacement curves for the four tested samples. The initiation of interlaminar tension failure can be seen by sudden drop in the load. For specimens #2 and #3, this initial–failure load was the maximum.

For specimen #4, the load dropped (70 N) and then increased but with a slightly lower slope than the initial one until the major crack (failure) occured. For specimen #5, however, the case was different where this load continues to increase

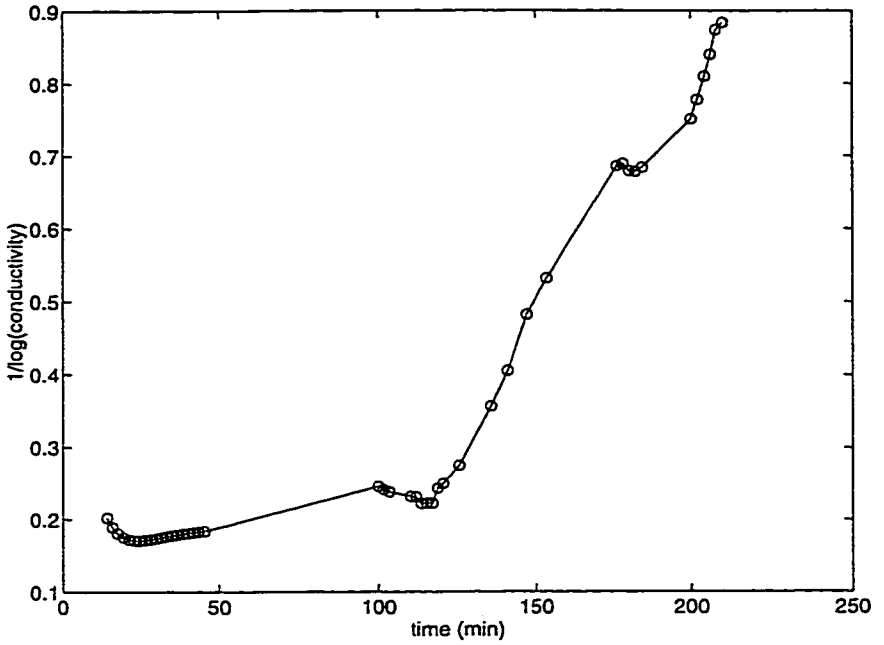


(a) Modified ionic conductivity versus time.

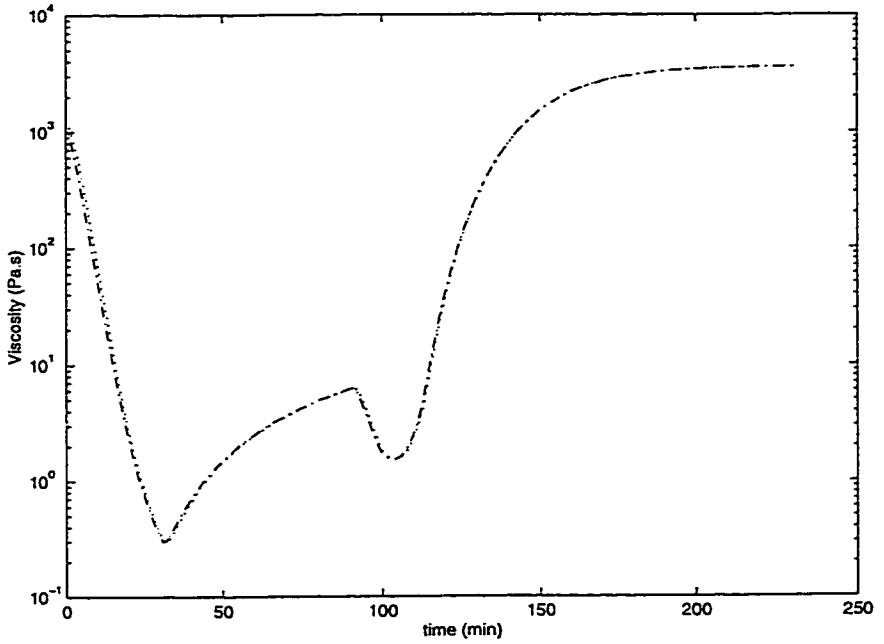


(b) Viscosity $\mu$ versus time.

Figure 4.33: The modified ionic conductivity and Viscosity versus time.

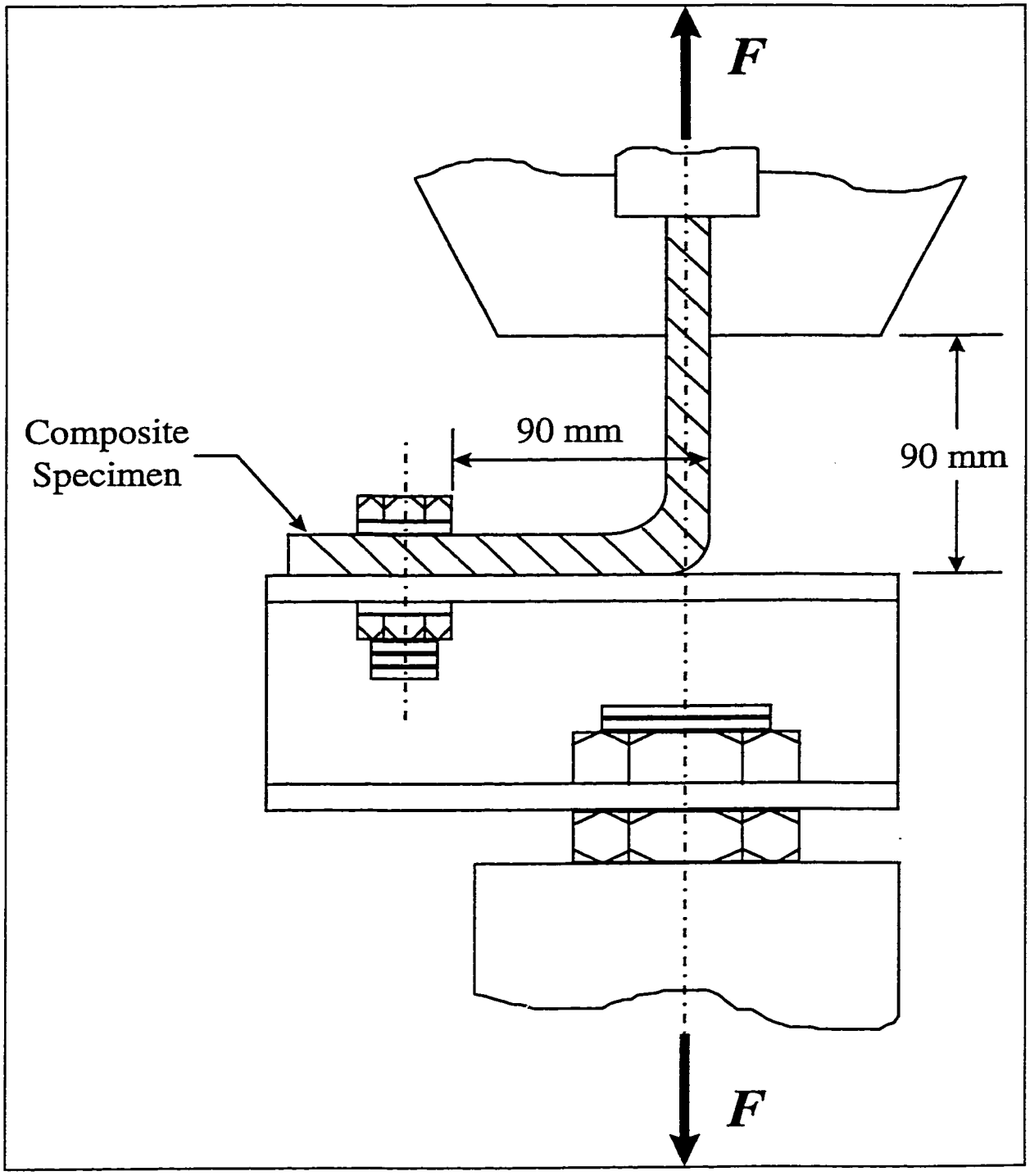


Figure 4.34: The test specimen and the test setup.

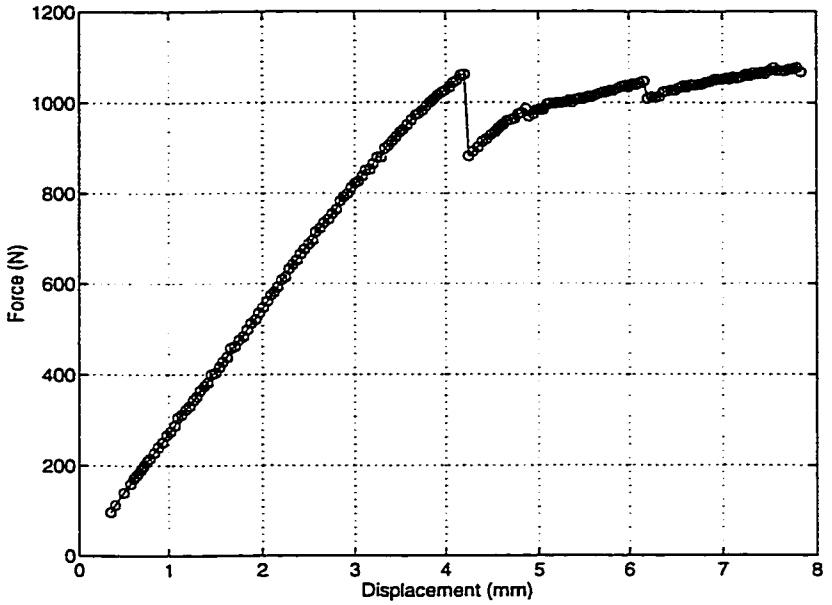


Figure 4.35: Load–displacement curve for sample #2.

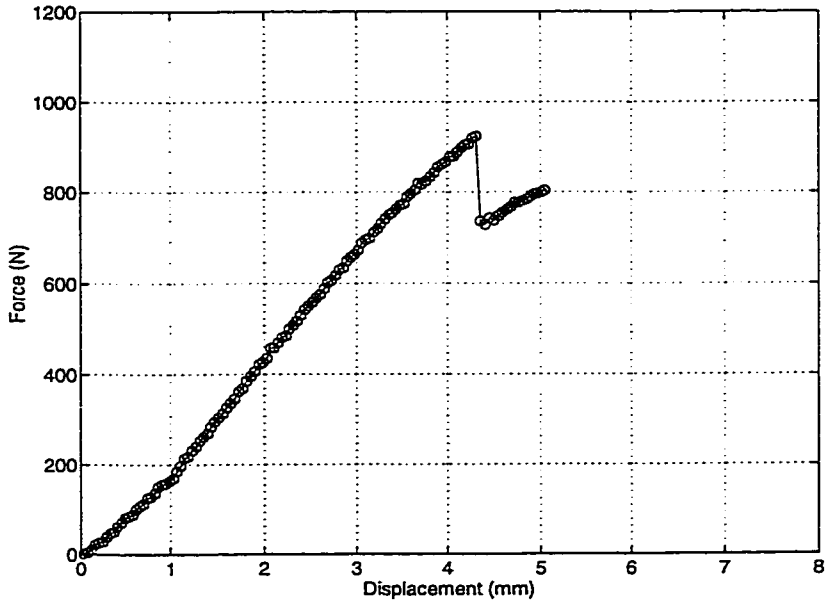


Figure 4.36: Load–displacement curve for sample #3.

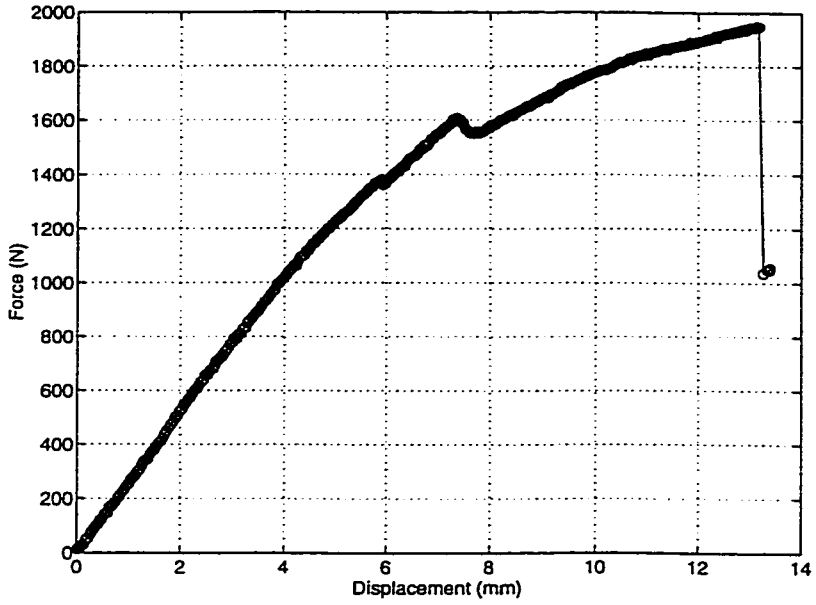


Figure 4.37: Load–displacement curve for sample #4.

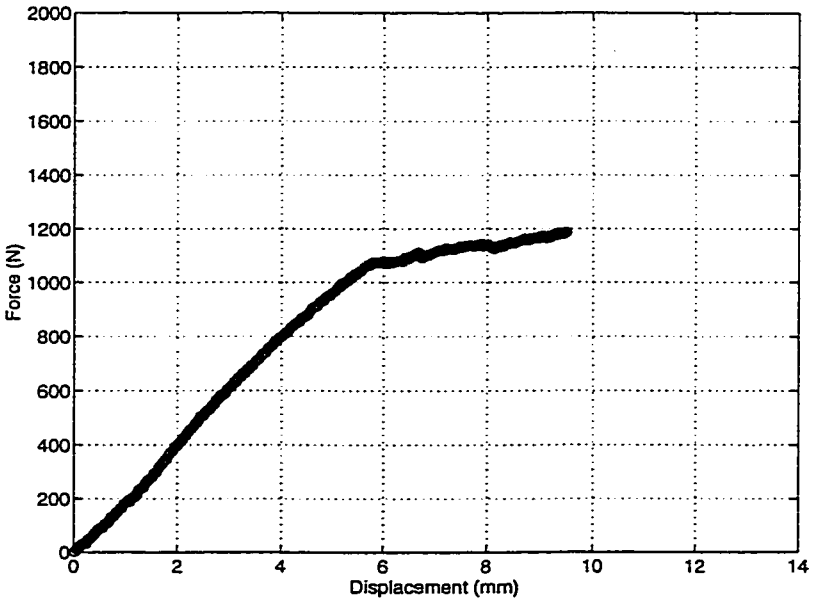


Figure 4.38: Load–displacement curve for sample #5.

| Sample # | $A$ $mm^2$ | $F$ (N) | $\sigma$ (N/$mm^2$) | Slope (N/mm) | $\delta$ (N) | d (mm) | $l_d$ |
|---|---|---|---|---|---|---|---|
| 2 | 173.4 | 1061 | 5.98 | 272 | 180 | 4.21 | 0.40 |
| 3 | 141.5 | 923 | 6.77 | 233 | 194 | 4.31 | 0.35 |
| 4 | 164.0 | 1600 | 9.76 | 254 | 49 | 7.28 | 0.65 |
| 5 | 139.5 | 1075 | 8.44 | 202 | – | 5.88 | 0.81 |

Table 4.3: Load–displacement results for all the samples.

at a very slow rate. Table 4.3 summarizes these results. The different parameters shown in the table are defined as follows:

$A$ = sample cross–sectional area at section 6,

$F$ = load at failure initiation,

$\sigma$ = stress at failure initiation ($F$ per area $A$),

Slope = slope of the linear portion before initial failure,

$\delta$ = amount of drop in force from initial failure,

d = displacement up to initial failure,

$l_d$ = location of delamination.

Examining the tested specimens showed that initial failure occurs by delamination along ply interfaces at the curved bend. This delamination then proceeds to the straight arms. Figure 4.39 shows the shape, path and location of delaminations that occurred in the specimens.

The distance between delamination site at initial failure and the inner surface of the curved part was found to be different from one sample to another. This site was closer to the inner surface for samples #2 and #3 than for samples #4 and #5, being the farthest for sample #5. Referring to Figure 4.24(a), the $v_f$ variation at section 6 shows a jump between $l$=0.5 and $l$=0.75, being more located near the middle. This jump can be related well to the location of delamination position at

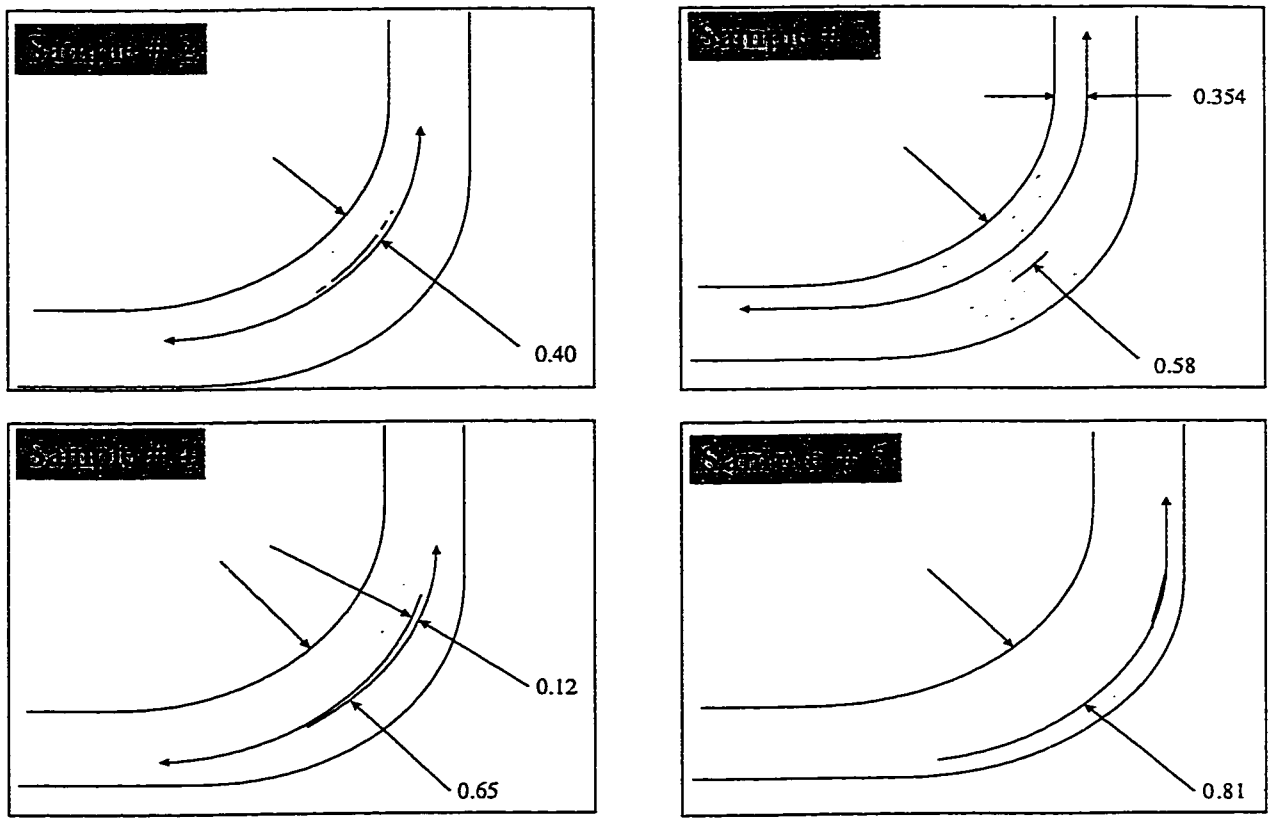


Figure 4.39: Schematic drawing showing delamination position for all the samples.

$l$=0.53 $\sim$ 0.65 for sample #4. Also, in Figure 4.24(b), the jump is noticed to be between $l$=0.5 and $l$=0.75, but more located near the outer surface which agrees well with the delamination position at $l$=0.81 for sample #5. Comparing samples #2 and #3, the number of micro–delaminations across the thickness was negligible for sample #2 compared to that for sample #3 which might be the reason that sample #3 has 13.2% more strength, 2.4% more displacement (up to the initial failure), and 7.8% more drop in load ($\delta$) than sample #2. For samples #4 and #5, the number of micro–delaminations was almost the same and negligible. Table 4.3 shows that sample #4 has 8.4% more strength and 23.7% more displacement than for sample #5.

## 4.7 Conclusions

In this chapter, thickness and fiber volume fraction variations were investigated for an L–shaped composite part. Both experiment and simulation show reasonable agreement in terms of thickness and fiber volume fraction values. They showed how the quality of the part is not consistent from section to section. Furthermore, they also demonstrated the need for a modified curing process that would produce uniform part thickness and fiber volume fraction across the length.

The enclosed angle measurements showed that in this particular case for AS4/3501–6 material, the 'spring in' was less than 1 degree. This can be referred to mainly two reasons: (1) The relatively thin laminate being processed, (2) The type

of releasing film used for the mold (Teflon). Johnston et al [35] showed that increasing part thickness and decreasing surface friction tends to decrease the 'spring in' angle.

The corner strength experiment showed that sample preparation, and processing parameters (curing cycle) have a strong effect on the mechanical properties of the final composite part which cannot be neglected.

The DEA analysis showed that *in–situ* monitoring of the curing process using dielectrometry can sense the end of the cure. The remote sensor used in collecting the data is not limited by thickness and is not susceptible to electro–magnetic interference and electrical insulation. Dielectrometry possesses a clear potential for further monitoring the structural integrity of the composite during part qualification and through its service life.

# Chapter 5

# Modified Curing Process

## 5.1 Introduction

Varying temperature, pressure, time and vacuum cycles in the autoclave leads to different curing processes which will end up with different final part quality: (1) The degree of cure and the fiber volume fraction affect the mechanical properties of the final composite part. (2) The pressure distribution affects the compaction of the laminate and the void formation. (3) Temperature gradients can introduce residual stresses and strains. (4) Finally, for cost–effective part, the duration of the processing cycle should be short. This problem has been addressed by many people especially in the manufacturing of thick parts.

The cure cycle (temperature and pressure) employed during autoclave processing of thermoset matrix composites may be selected by trial and error procedures or by the use of analytic models. Empirical methods may be acceptable for thin composites but are impractical for thick parts. For thin as well as thick composites

an appropriate way to establish the cure cycle is by models.

In this chapter, a modified curing process will be developed that minimizes the spatial variations in thickness and fiber volume fraction along with the gradients in temperature and degree of cure. Furthermore, the temperature overshoot experienced in the processing of thick composite parts will be minimized. 2–step and 3–step curing cycles will be implemented theoretically to study the variations in thickness and fiber volume fraction of an angle–bend structure made from 50 layers of graphite/epoxy Hercules AS4/3501–6 prepreg.

## 5.2 Parametric Study

A parametric study was conducted to obtain the modified curing cycle for a 50 layers angle–bend part that was shown in Figure 4.2. Firstly, a two step curing cycle was used, and the temperature and viscosity distributions were obtained for different hold temperatures $T_1$ and $T_2$ and hold times $t_1$ and $t_2$ (the ramp rate was kept constant at $2.5°C/min$). Secondly, a three step curing cycle was applied with different hold temperatures $T_1$, $T_2$ and $T_3$ and times $t_1$, $t_2$ and $t_3$. Results were obtained for temperature, viscosity and thickness variations. Schematics of the 2–step and 3–step cycles were shown in Figure 4.3.

The simulation model was used to predict the temperature, degree of cure ($\alpha$), viscosity ($\mu$) and fiber volume fraction ($v_f$) distribution throughout the laminate. Temperature and pressure boundary conditions are the same as discussed before.

Results discussed below are at section 6 and $l$=1/2 obtained for different 2–step and 3–step cycles. (Refer to Figure 4.11.)

### 5.2.1 The 2–step cure cycle

1. Effect of $T_1$:

   In Figure 5.1 the $t_1$, $t_2$ and $T_2$ values were kept constant with $T_1$ value changing. This figure, which is for $t_1 = 60$ min, shows that increasing $T_1$ from $90°C$ to $115°C$ causes the amount of temperature overshoot at $T_2$ to decrease by 0.21%. This means that increasing the holding temperature at $T_1$ leads to a decrease in temperature overshoot at $T_2$. The second part of this figure shows the viscosity variation with curing time. Viscosity plays a significant role in consolidation. The application of pressure should be while the viscosity is low enough to facilitate processing. Additionally, the resin flow determines the fiber volume fraction which, in turn, will modify all composite properties besides the thickness. Hence, for the particular cycle shown in Figure 5.1, autoclave pressure application should begin 20 minutes after the start of cure cycle and should last for about 100 minutes.

   The effect of $T_1$ on the degree of cure ($\alpha$) variation during cure is shown in Figure 5.2. It is clear that increasing the first hold temperature will initiate the cure faster relative to the lower $T_1$. However, the laminate cures completely at the same time.

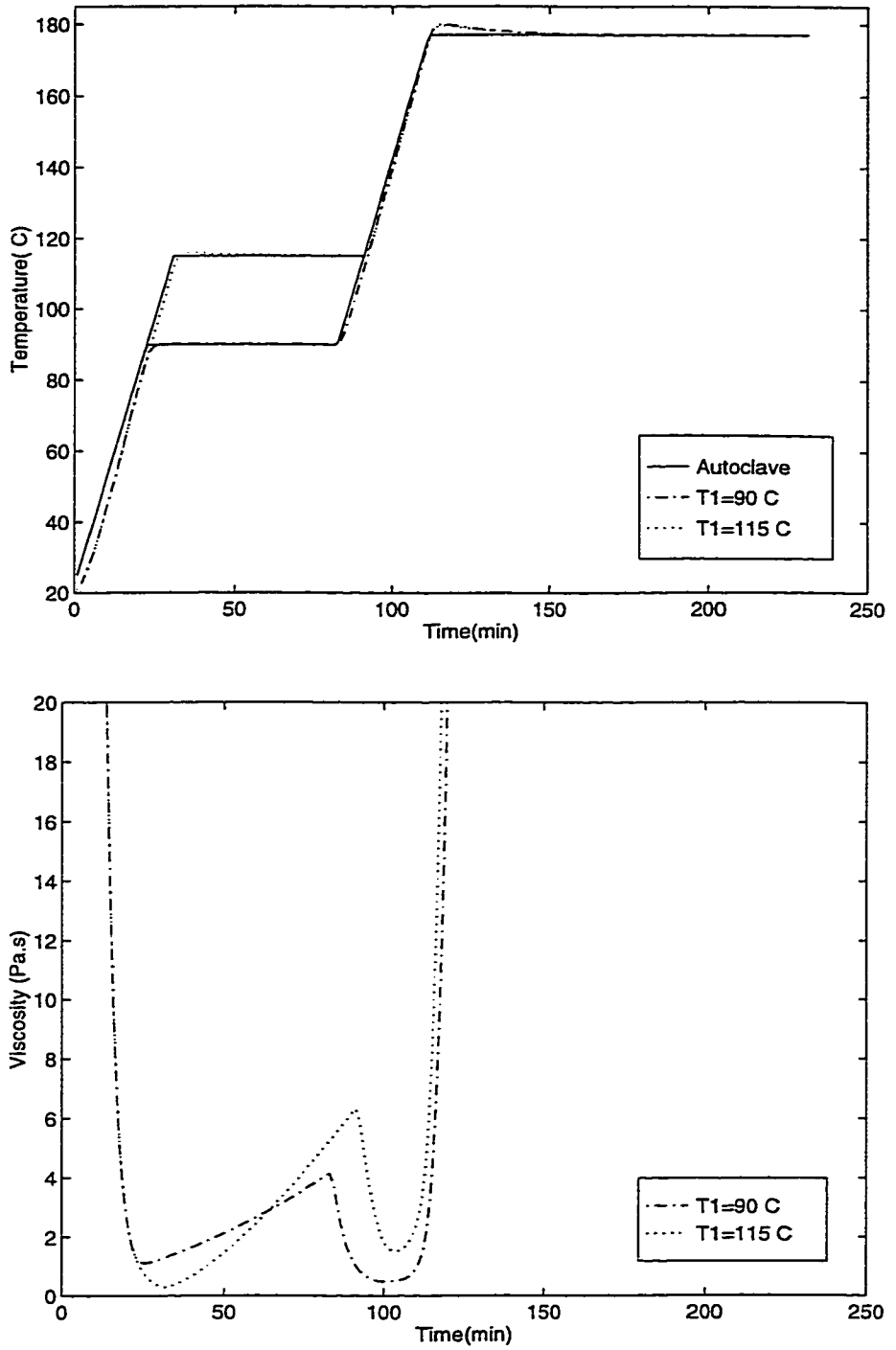


Figure 5.1: The effect of temperature $T_1$ on temperature overshoot and viscosity for 2–step cycles. Figures are for $t_1 = 60$ min

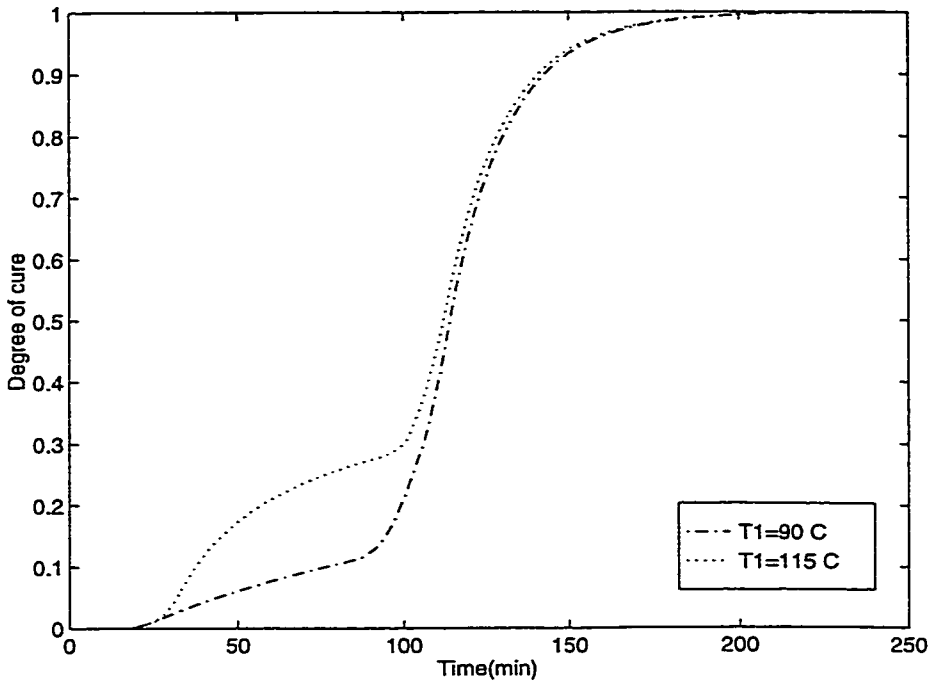


Figure 5.2: The effect of temperature $T_1$ on degree of cure variation for 2–step cycles.

2. Effect of $t_1$:

   In Figure 5.3, it is seen that increasing $t_1$ from 60 to 90 minutes did not result in a significant change in the amount of temperature overshoot at $T_2$ (-0.03%). However, this increase in $t_1$ results in an increase in the period of low viscosity ($\mu$) equivalent to 30 minutes (the difference between 60 and 90 minutes). Furthermore, comparing the degree of cure ($\alpha$) variation during cure between the two times, Figure 5.4 shows that the laminate cures in a shorter total time when the intermediate holding time $t_1$ is shorter.

3. Effect of $T_2$:

   Figure 5.5 shows the variation in temperature and viscosity when $t_1$, $t_2$ and

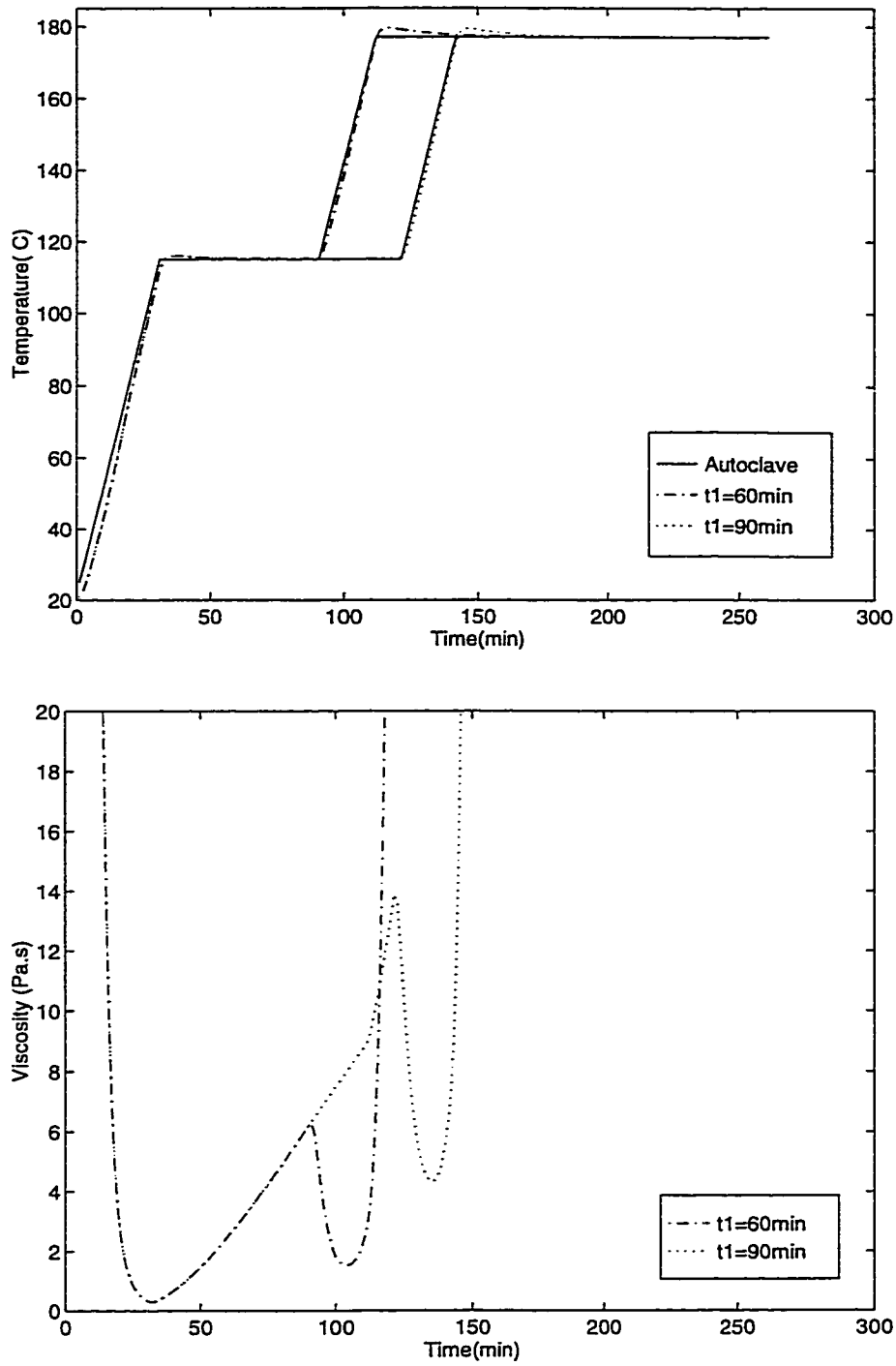


Figure 5.3: The effect of time $t_1$ on temperature overshoot and viscosity for 2–step cycles. Figures are for $T_1 = 115°C$.

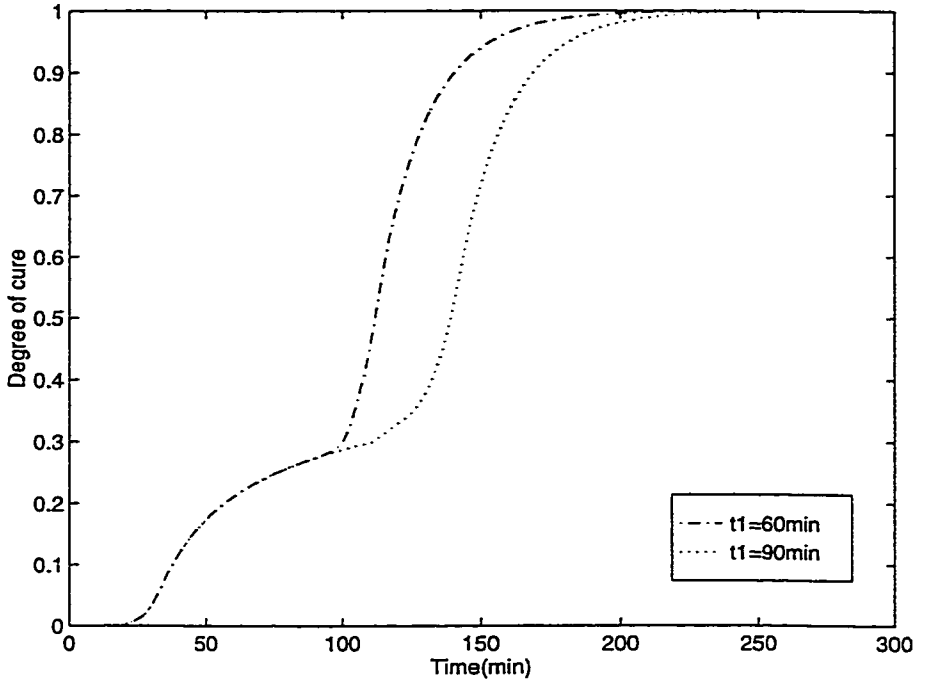


Figure 5.4: The effect of time $t_1$ on degree of cure variation for 2–step cycles.

$T_1$ values were kept constant and $T_2$ was varied between $165°C$ and $177°C$. It is shown that increasing $T_2$ causes the amount of temperature overshoot to increase by 0.5%. However, the value of $T_2$ has no significant effect on the viscosity values. On the other hand, comparing the degree of cure variation $\alpha$ with cure time, shown in Figure 5.6, shows that increasing $T_2$ shortens the time to achieve a completely cured laminate.

4. Effect of $t_2$:

From the degree of cure results for the different 2–step cycles discussed above (Figures 5.2, 5.4 and 5.6), it is clear that the time $t_2$ should be long enough to give a completely cured laminate ($\alpha = 1$). Longer times might be necessary

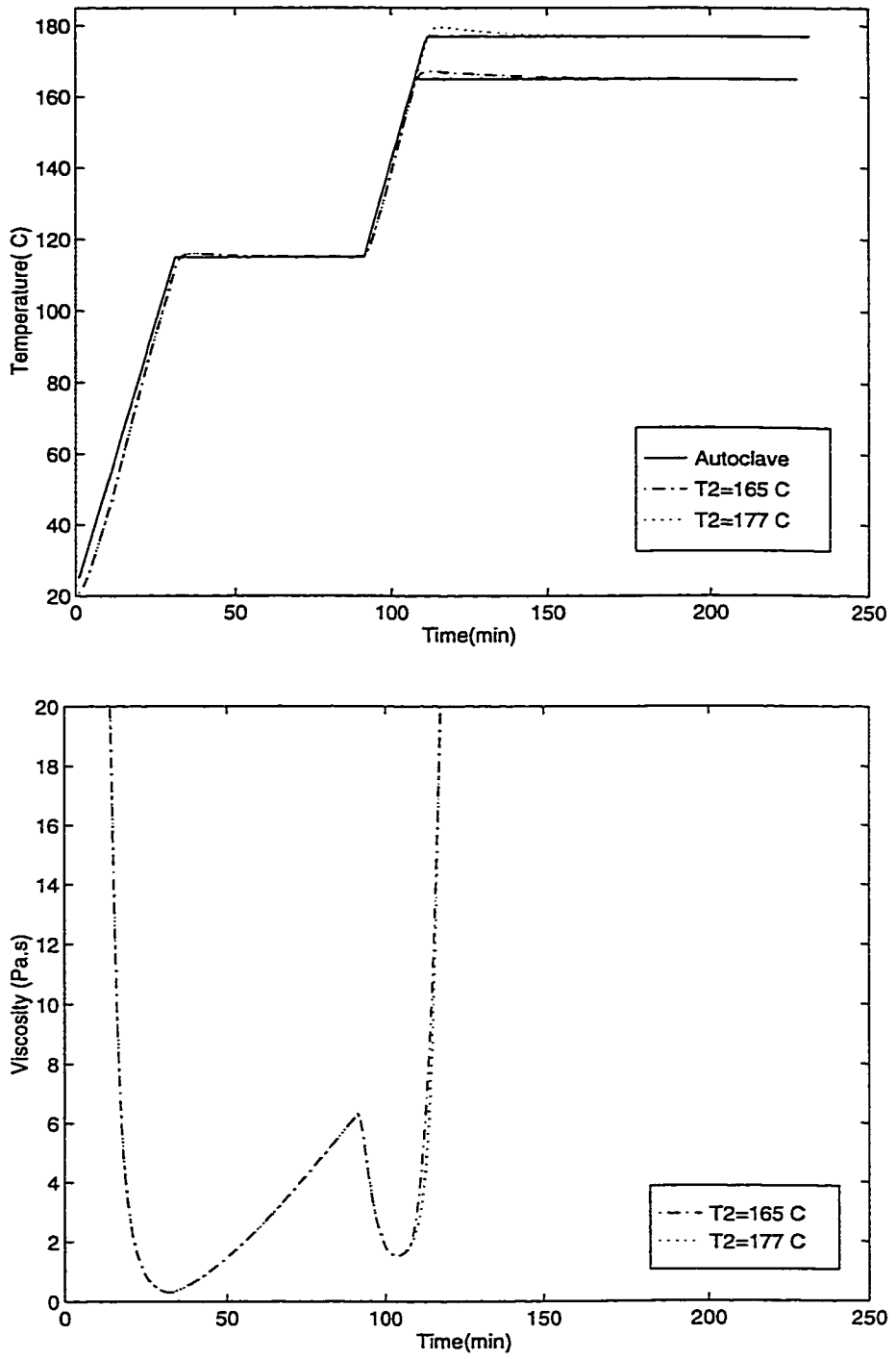


Figure 5.5: The effect of temperature $T_2$ on temperature overshoot and viscosity for 2–step cycles. Figures are for $T_1 = 115°C$.

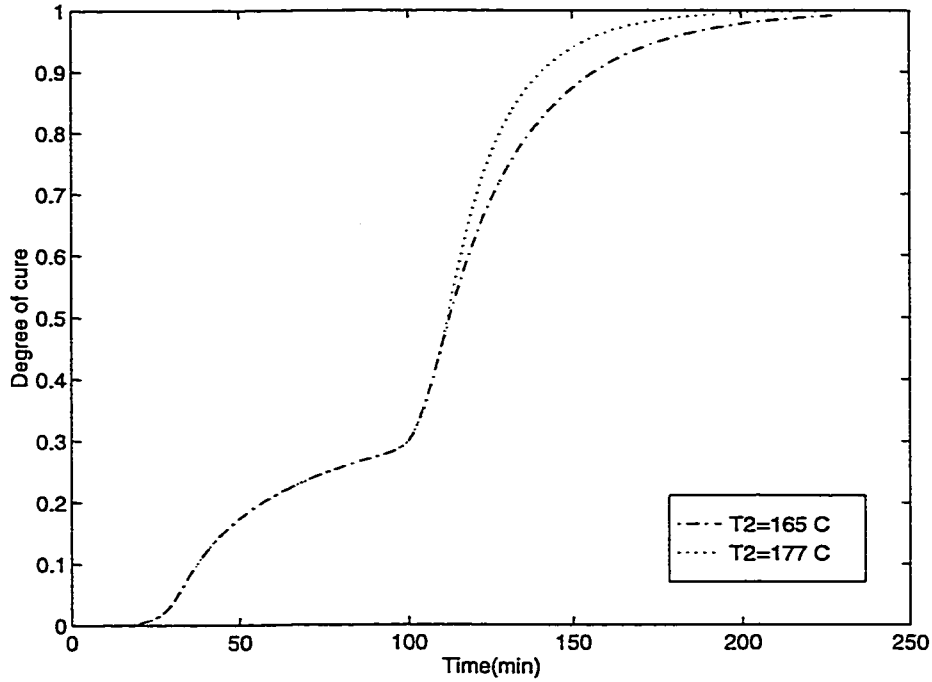


Figure 5.6: The effect of temperature $T_2$ on degree of cure variation for 2–step cycles.

when higher operating–temperature part is required [2].

### 5.2.2 The 3–step cycle

1. Effect of $T_1$:

   Figure 5.7 show 3–step curing cycles that have the same holding times ($t_1$, $t_2$, and $t_3$) and temperatures $T_2$ and $T_3$, but with different $T_1$ values. The figure shows that increasing $T_1$ from $80°C$ to $115°C$ causes the amount of temperature overshoot at $T_2$ to decrease (0.25%) while no significant decrease in this amount is noticed at $T_3$ (0.055%). As for viscosity, different behavior is noticed for different $T_1$. The period of low viscosity decreased when $T_1$ has increased.

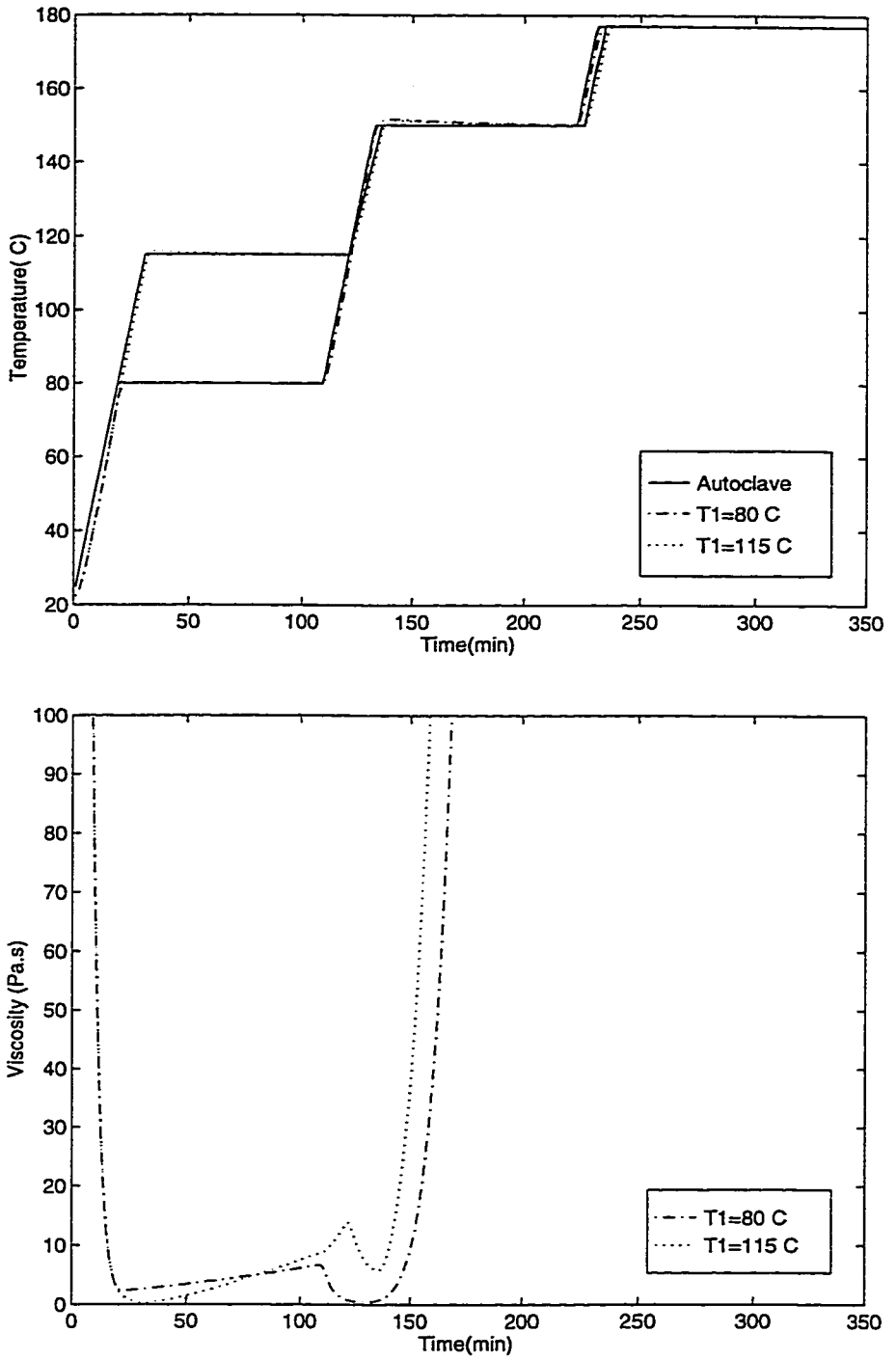


Figure 5.7: The effect of temperature $T_1$ on temperature overshoot and viscosity for 3–step cycles. Figures are for $t_1 = 90$ min.

The effect of $T_1$ on $\alpha$ can be seen in Figure 5.8. It is clear that increasing the first hold temperature did not affect total curing time based on the extent of cure behavior.

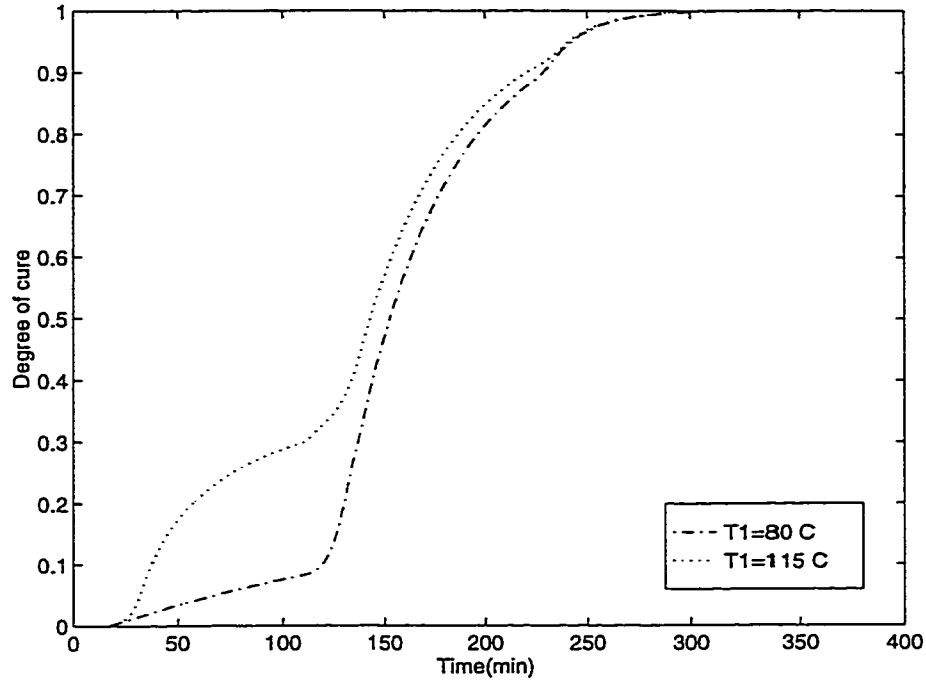


Figure 5.8: The effect of temperature $T_1$ on degree of cure variation for 3–step cycles.

2. Effect of $t_1$:

Increasing $t_1$ from 60 to 90 minutes can be seen to have no significant decrease on temperature overshoot at $T_3$ as shown in Figure 5.9 (0.015%). However, its effect on viscosity is the increase in the period of low $\mu$ by 30 minutes (as the case in 2–step cure cycles). Also, in Figure 5.10 is shown the effect of $t_1$ on $\alpha$ where increasing $t_1$ increases the processing time to get a completely cured laminate.

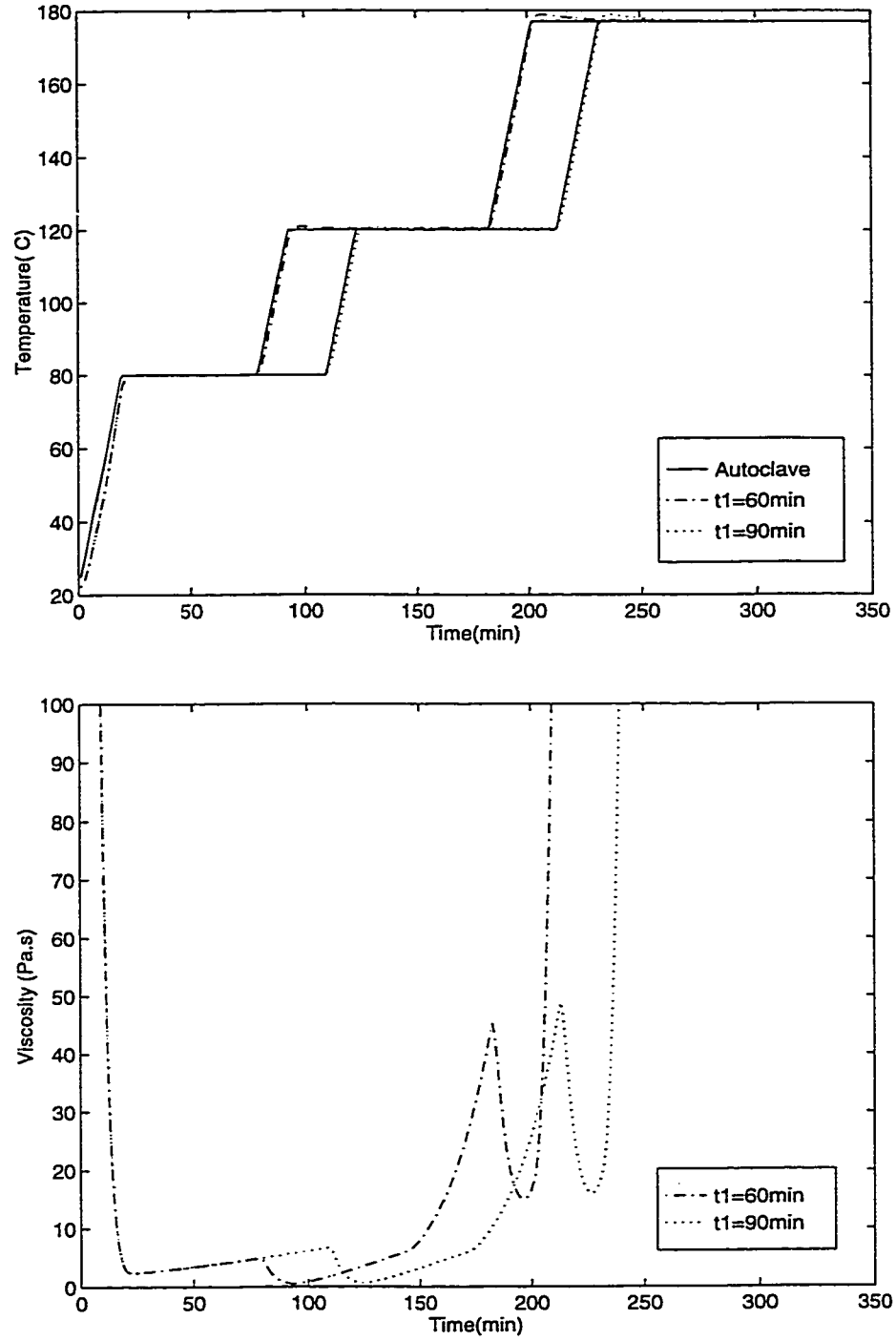


Figure 5.9: The effect of time $t_1$ on temperature overshoot and viscosity for 3–step cycles. Figures are for $t_2 = 90$ min.

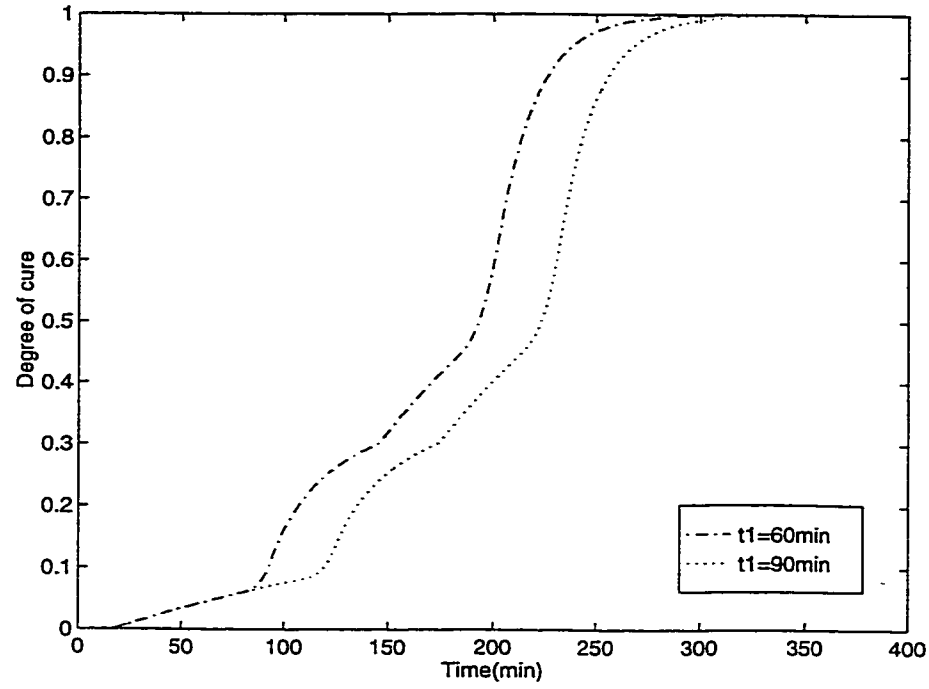


Figure 5.10: The effect of time $t_1$ on degree of cure variation for 3–step cycles.

3. Effect of $T_2$:

   In Figure 5.11, it is shown that increasing $T_2$ from 120°$C$ to 150°$C$, while keeping everything else unchanged, leads to a decrease in temperature overshoot at $T_3$ by 0.85 %. Also, this increase causes a decrease in the period of low $\mu$ by about 100 minutes. The effect on $\alpha$ is shown in Figure 5.12. Clearly, increasing $T_2$ will shorten the processing time to have $\alpha$=1.

4. Effect of $t_2$:

   Figure 5.13 shows that increasing $t_2$ for 3–step cycles from 60 to 90 minutes decreases the amount of overshoot in $T_3$ by 0.24%. Its effect on viscosity was to increase the period of low $\mu$ by 30 minutes. The resulted $\alpha$ variation is

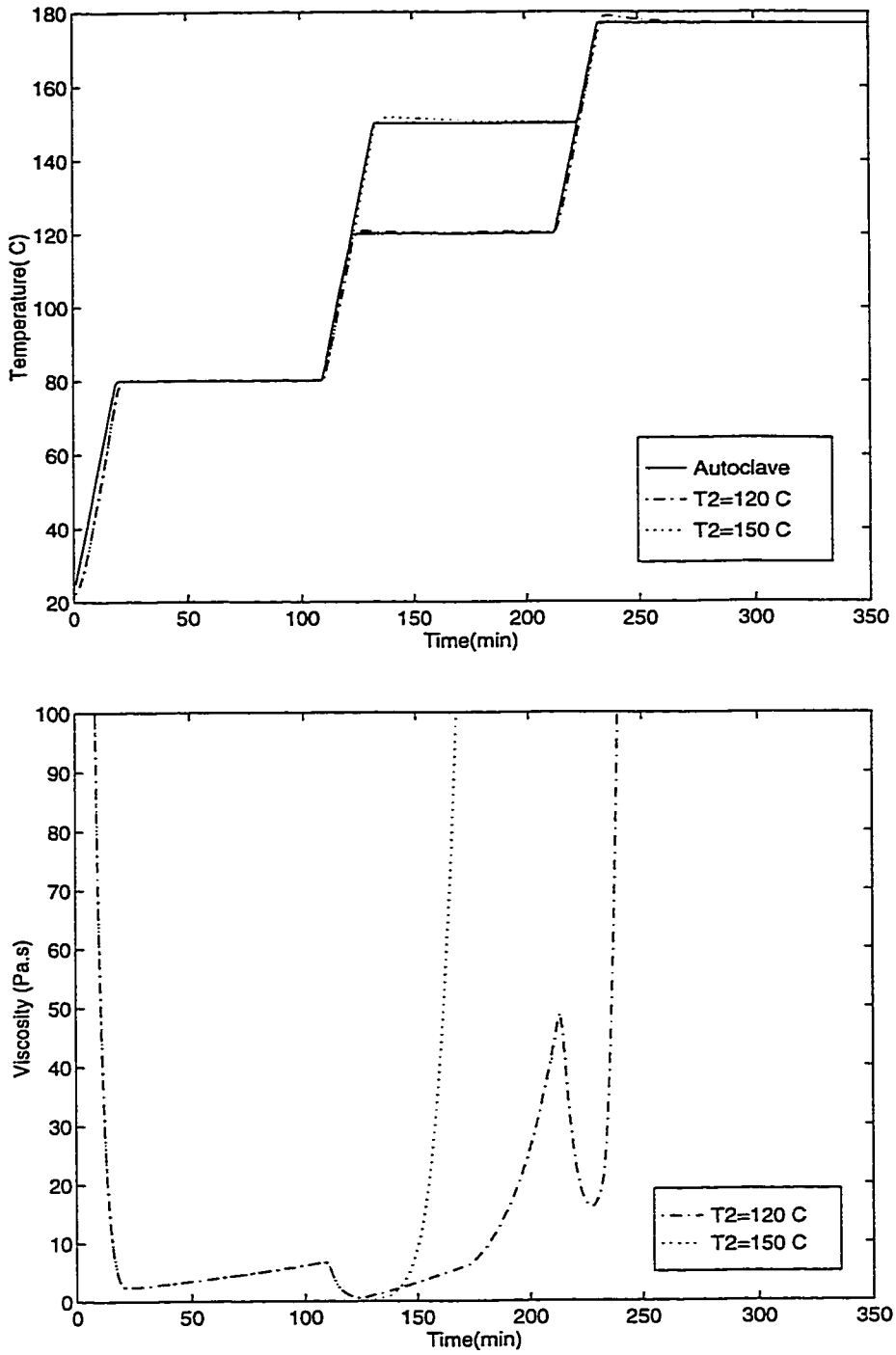


Figure 5.11: The effect of temperature $T_2$ on temperature overshoot and viscosity for 3–step cycles. Figures are for $t_1 = 90$ min.

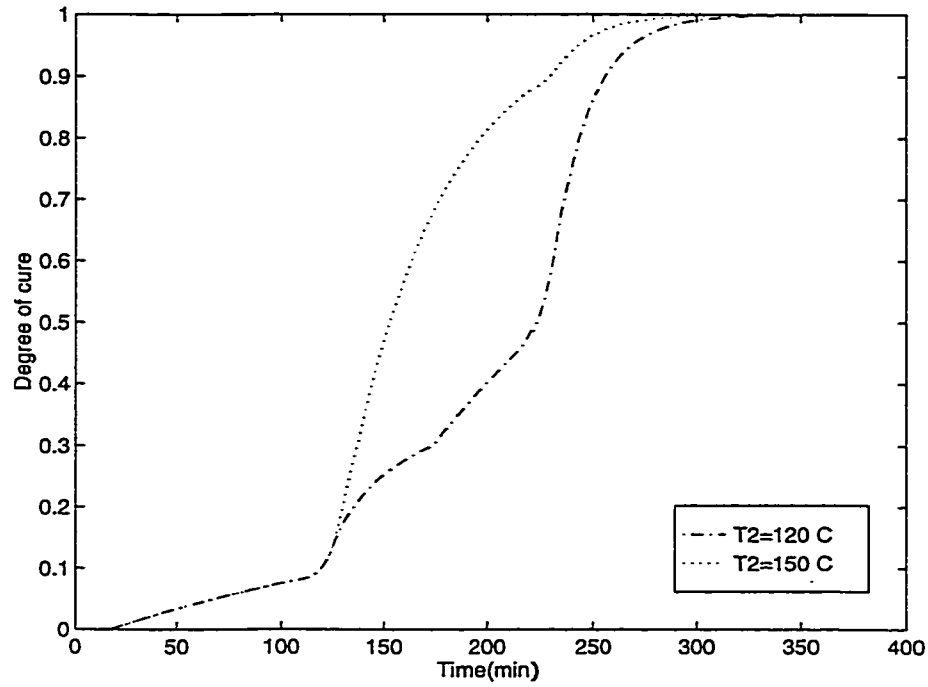


Figure 5.12: The effect of temperature $T_2$ on degree of cure variation for 3–step cycles.

shown in Figure 5.14 where increasing $t_2$ increases the processing time.

5. Effect of $T_3$:

   Similar to the 2–step curing cycle, Figure 5.15 shows that increasing $T_3$ (the last hold temperature) from $165°C$ to $177°C$ increases the amount of overshoot by 0.17%. However, this does not affect the period of minimum $\mu$ where no difference in the viscosity variation is present as shown in Figure 5.16. As for the processing time, $\alpha$ reached the value 1 faster when $T_3$ was raised.

### 5.2.3 Summary

To summarize the above results, we can say that:

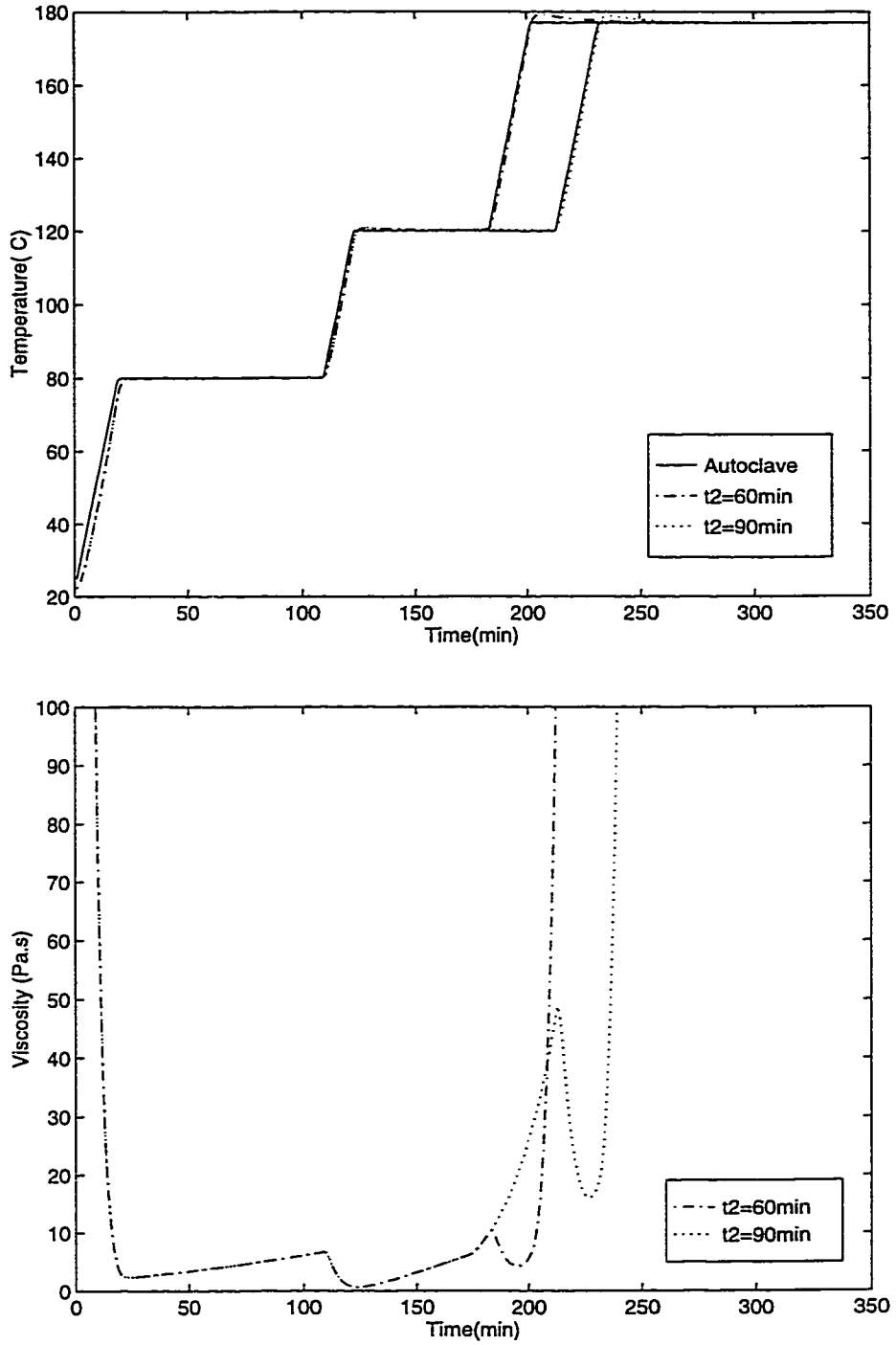


Figure 5.13: The effect of time $t_2$ on temperature overshoot and viscosity for 3–step cycles. Figures are for $t_1 = 90$ min.

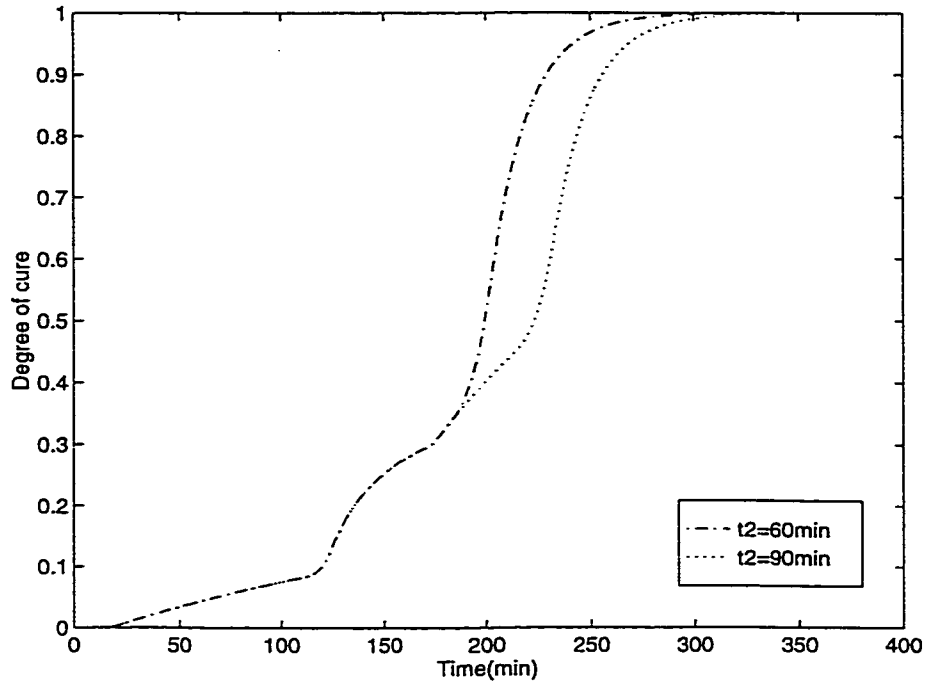


Figure 5.14: The effect of time $t_2$ on degree of cure variation for 3–step cycles.

- Increasing the first holding time in any cycle will result in an increase in the period of low $\mu$. This will permit the consolidation of the fibers and the elimination of excess resin early in the curing process. On the other hand, increasing successive holding times will prolong the consolidation process.

- Decreasing the difference between any two successive holding temperatures decreases the amount of temperature overshoot in the subsequent hold and hence eliminates the risk of matrix degradation.

- It was noted that the last holding time ($t_2$ for 2–step cycle and $t_3$ for 3–step cycle) has no effect on the final part thickness, although it has a significant effect on the temperature overshoot and the duration to completion of the

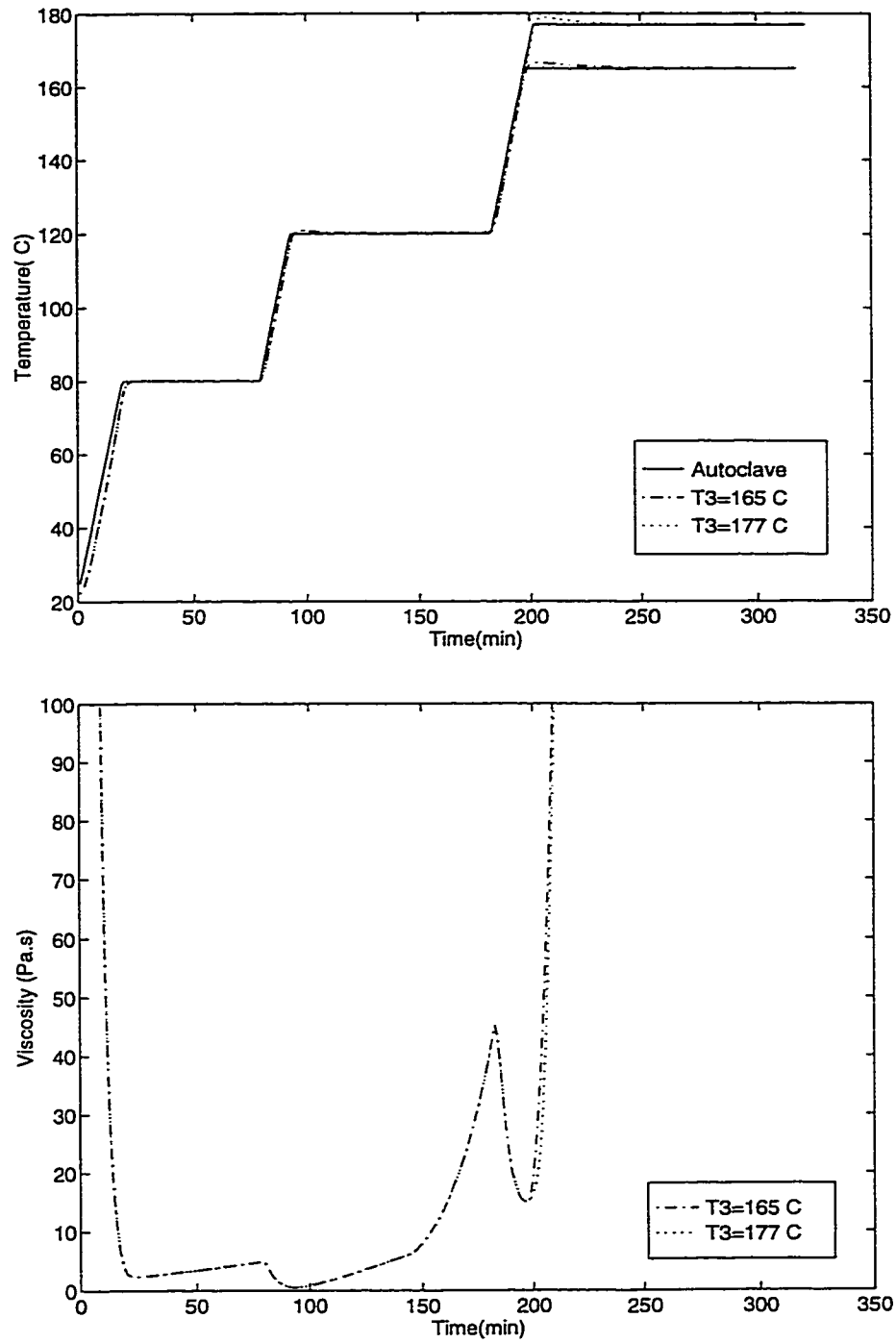


Figure 5.15: The effect of temperature $T_3$ on temperature overshoot and viscosity for 3–step cycles. Figures are for $t_2 = 90$ min.

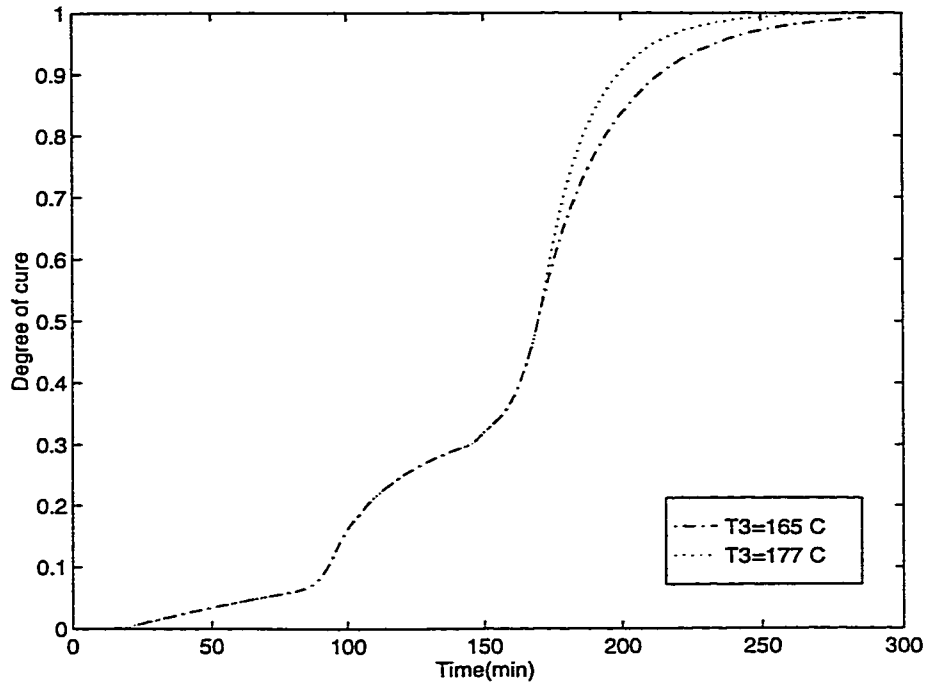


Figure 5.16: The effect of temperature $T_3$ on degree of cure variation for 3–step cycles.

chemical reaction ($\alpha = 1$).

## 5.3 Modifications on The Curing Process

Following the 2–step and 3–step *recommended* curing cycles was shown to result in a fiber volume fraction and thickness variation along the part length (previous chapter). Also, the results outlined above show that following the recommended curing cycle for thick angle–bend composites leads to spatial variations in fiber volume fraction and thickness, and hence affects the final quality of the part. Furthermore, the temperature overshoots experienced here could lead to matrix degradation if the maximum temperature exceeds a certain limit ($180°C$ by Loos and Springer [4]).

### 5.3.1 Temperature overshoot

Following the procedure outlined by Kim and Lee [33], temperature overshoot can be reduced through steps of cooling and reheating. Setting a maximum temperature limit for temperature overshoot, the cooling step can start before the time at which this temperature is reached. Once the laminate temperature decreases to the holding one, then cooling step ends and reheating starts up until the end of the holding time. However, the resulting cure cycle will differ from one part to another depending on the composite thickness. Alternatively, since the last holding temperature, in our case, is below $180°C$ which is the maximum temperature arbitrarily chosen by Loos and Springer [4] for AS4/3501–6 composites, then after holding the part at temperature $T_1$ (in the 2–step cycle) or $T_2$ (in the 3–step cycle) the part temperature can be increased to T‘ (just below the maximum temperature, for example $177°C$)

after which it is decreased at the same rate ($2 \sim 2.5$ o $C/min$) to the last holding temperature and kept there until the end of cure. The final modified cycle looks like the cycles shown in Figure 5.17 for both 2–step and 3–step cycles.

In Figures 5.18 and 5.19, the simulation results obtained by applying the modified 2– and 3–step cycles to thick angle–bend composite processing are presented. It is clear that the temperature overshoot was controlled and did not exceed the maximum one.

### 5.3.2 Thickness and fiber volume fraction variation

To get a final part that has a consistent quality in terms of thickness and $v_f$ distribution, the curing process itself should be altered. Reference [72] was the only one that mentioned how they controlled the fabrication conditions to achieve "uniform nominal thickness" in the corner of a flange–web. The material was AS4/5250-3 (graphite/BMI) biwoven cloth. When laminates were manufactured with a female tool and pressure bagged on the inner radius, high level of "manufacturing and processing" porosity was detected in their corner. When the specimens were manufactured using hard tools on both sides, uniform thickness in the corner was obtained and controlled conditions allowed no porosity in the corner. Although this method may be able of producing uniform thickness, nothing was mentioned about the quality in terms of uniform $v_f$ and no fiber wrinkling or waveness. Also, introducing a hard tool on the both laminate sides affects the heat transfer process and hence the temperature distribution during cure.

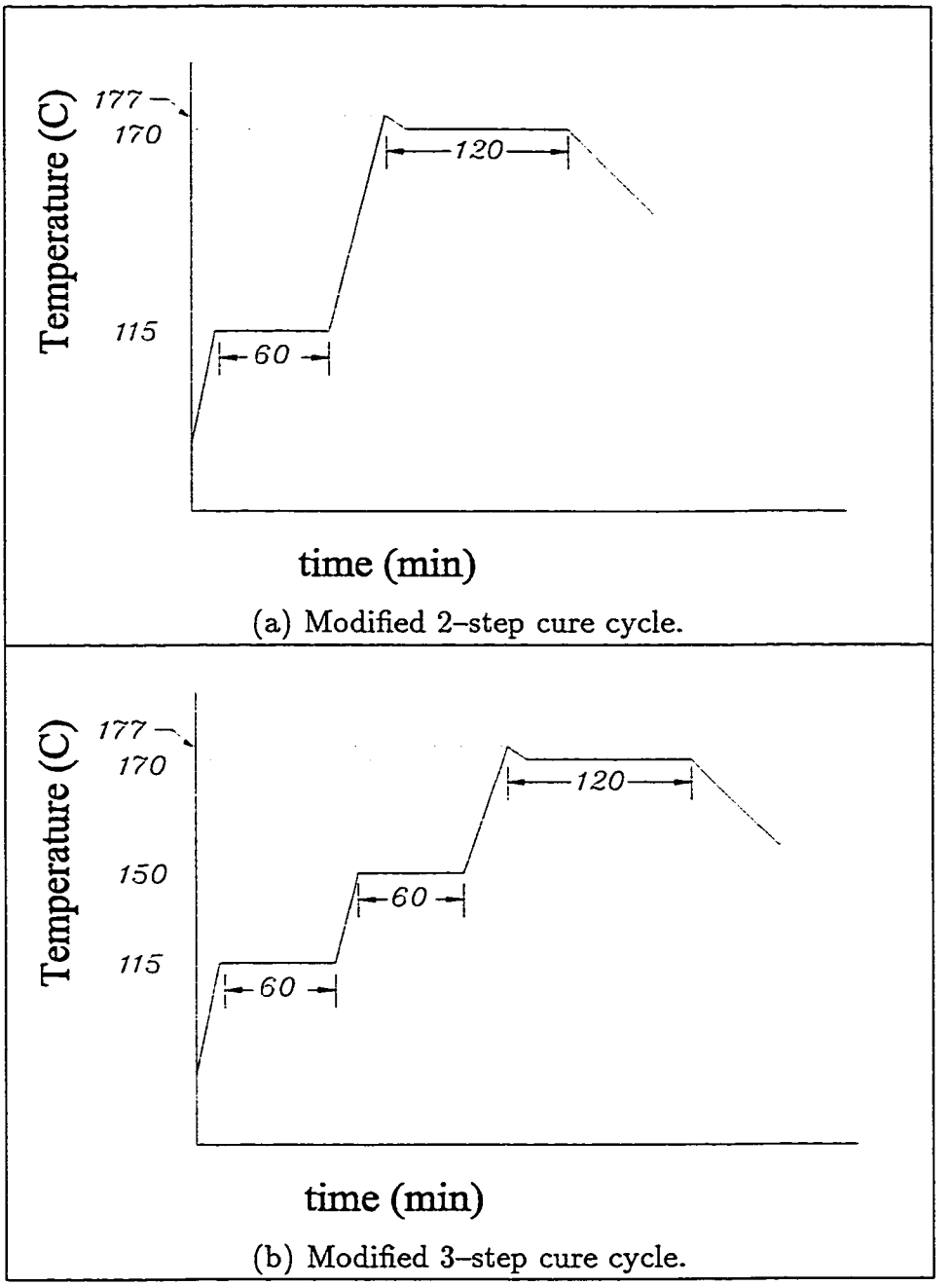


(a) Modified 2–step cure cycle.

(b) Modified 3–step cure cycle.

Figure 5.17: The modified cure cycle for L–shaped laminates

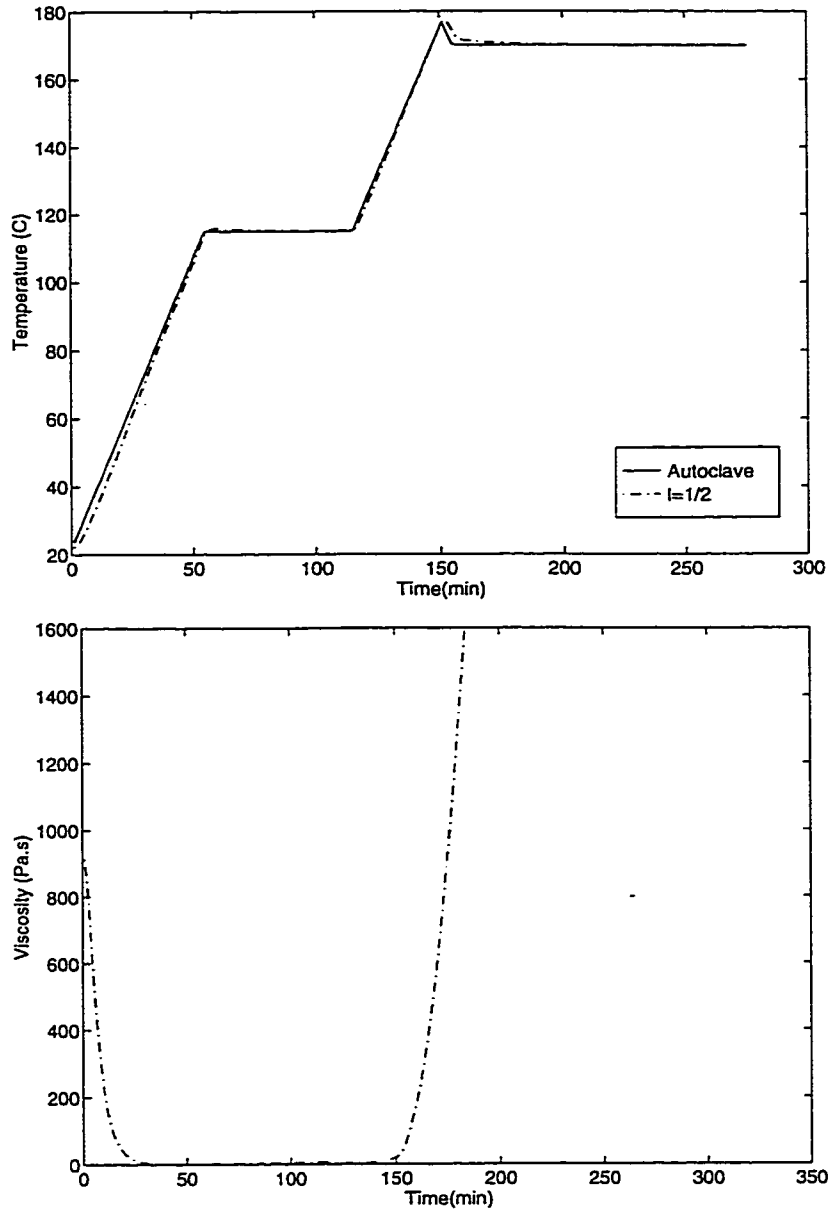


Figure 5.18: Temperature and viscosity variation obtained for the modified 2–step cure cycle.

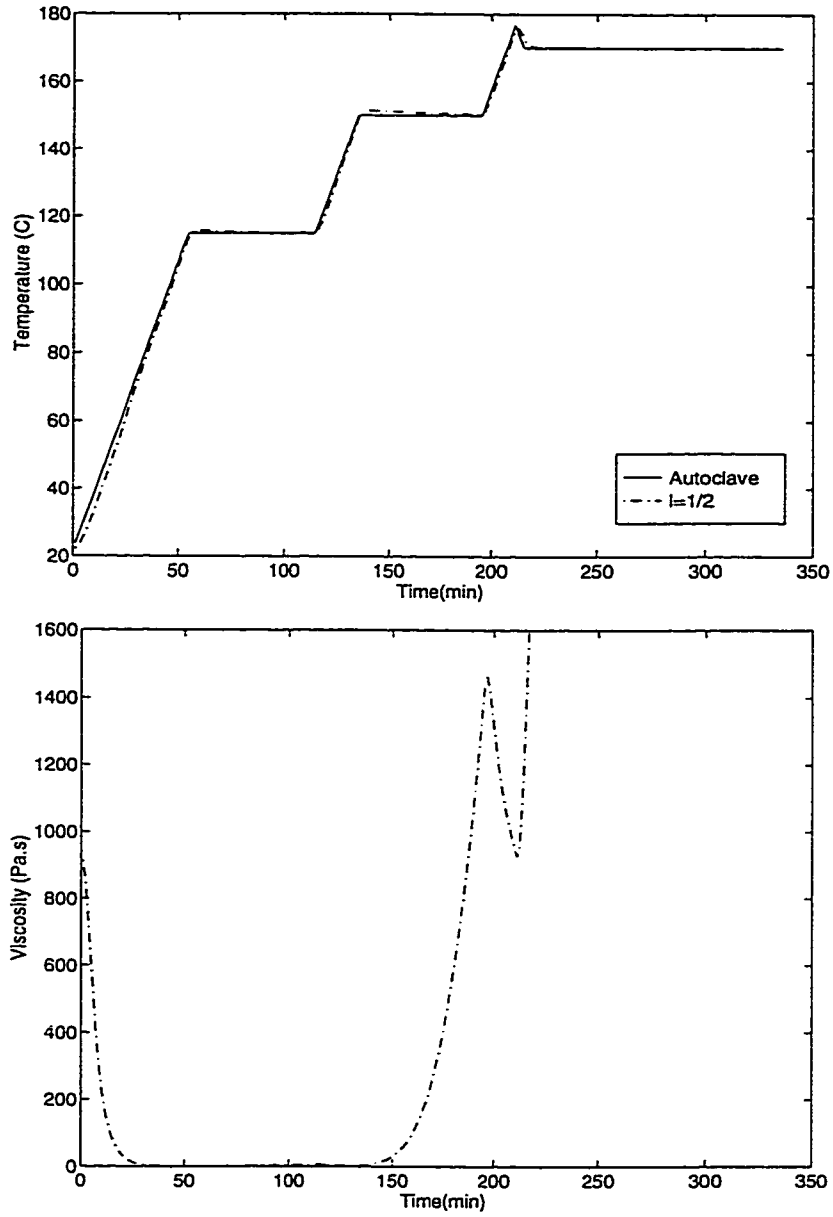


Figure 5.19: Temperature and viscosity variation obtained for the modified 3–step cure cycle.

In our case, since the lowest $v_f$ value is present at the curved bend adjacent to the mold surface, then inserting a bleeder layer between the mold and the composite part prior to processing will allow resin to escape at that surface and hence increase the $v_f$ value. Consequently, this will result into a lower variation in thickness from section to section. (This case will be referred to as Case(I).)

Alternatively, referring to the results of processing curved parts obtained in the previous chapter (shown again in Figure 5.20), adjusting the number of perforated release films on the upper surface will allow controlling the amount of resin flow out of the part. (This case will be referred to as Case(II).) This will produce a uniform thickness but will not give a uniform $v_f$ distribution. (This case will be referred to as Case(II).)

To simulate the presence of the lower bleeder layers, $(F_c)_{eff}$ was set equal to 0.1 instead of letting $\frac{\partial P}{\partial \eta} = 0$. Figure 5.21 shows the model results of applying this pressure boundary on the bottom surface Case(I). As shown, the thickness variation was controlled and kept to a negligible value. Also, as anticipated, the $v_f$ variation was zero for Case(I) ($v_f \approx 68\%$) as shown in Figure 5.22.

### 5.3.3 Limitations

The computer code was tested for laminates that are more than 50 layers in thickness and that are processed using the modified curing process Case (I). The results for temperature variation are shown in Figure 5.23 and those for thickness variation are shown in Figure 5.24 (both are for the 2–step curing process). Manufacturing a 100

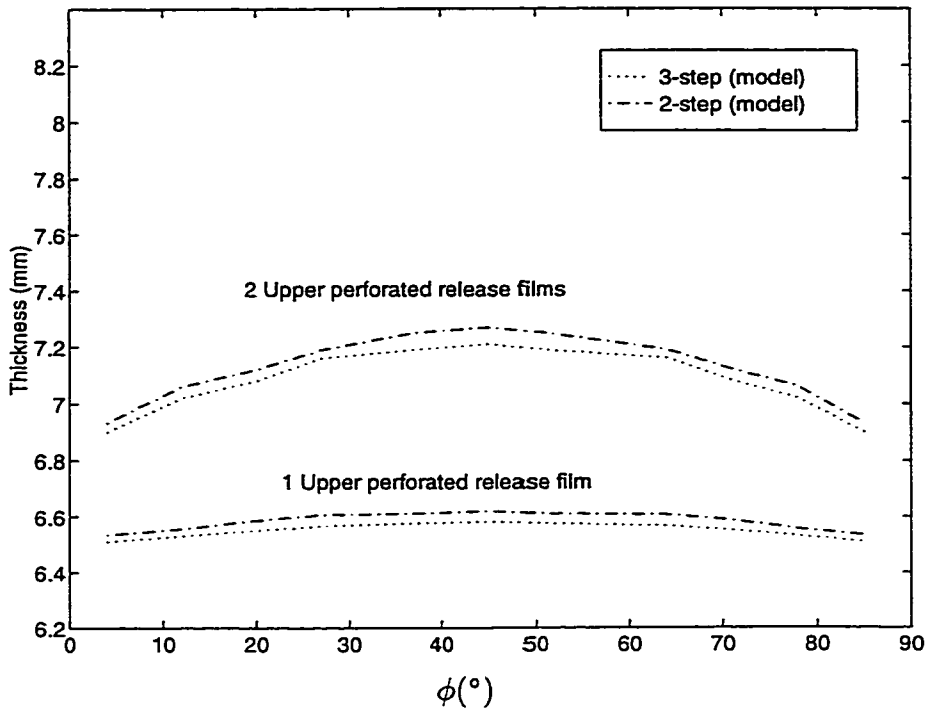


Figure 5.20: Thickness variation along curved parts processed with the recommended 2–step and 3–step cure cycles.

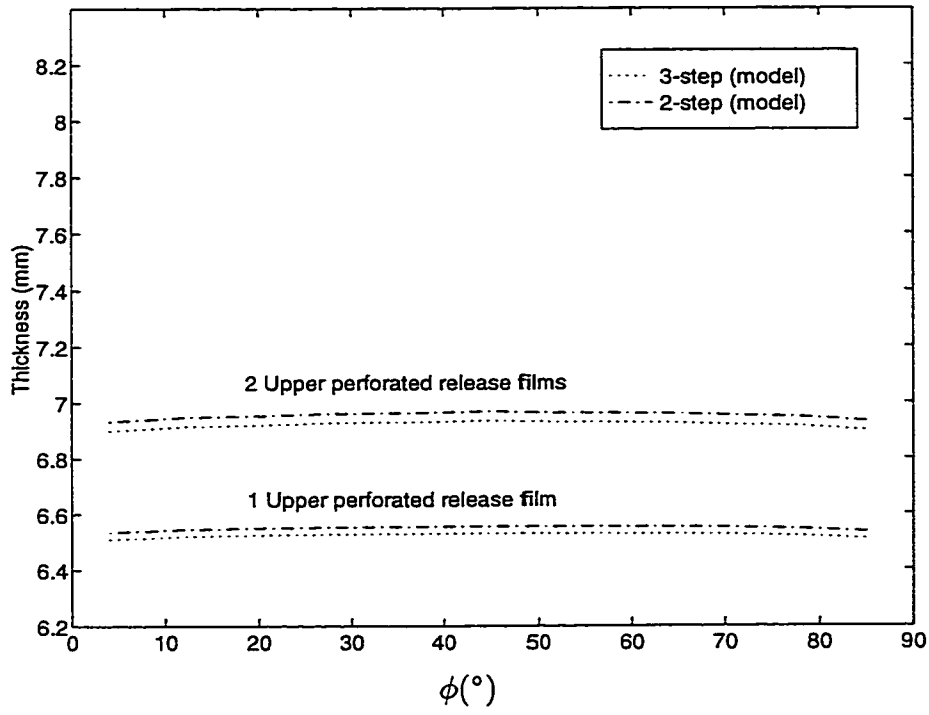


Figure 5.21: Thickness variation along the curved part for Case (I).

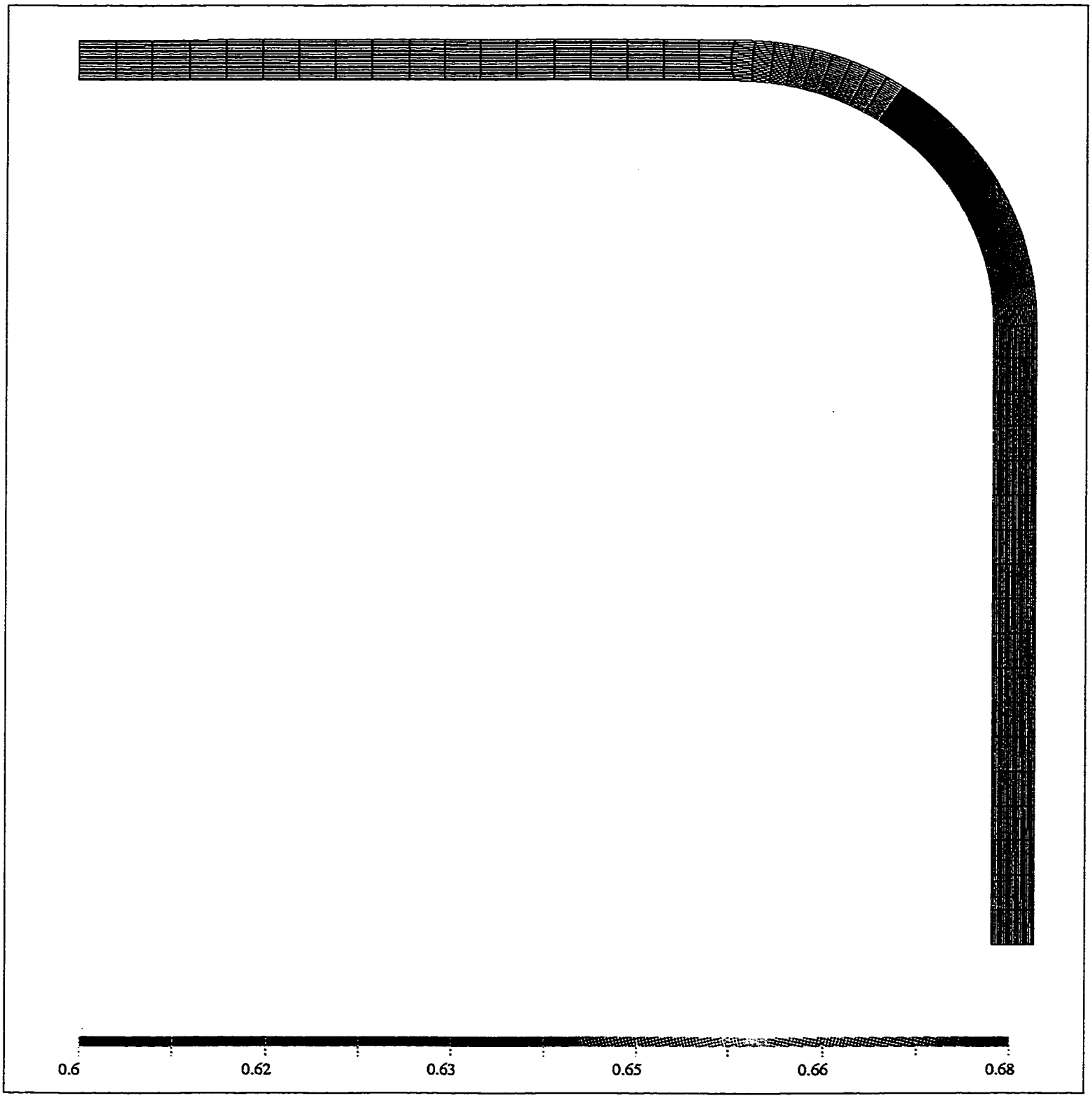


Figure 5.22: Fiber volume fraction distribution across the thickness obtained for the modified 2–step curing process, Case(I).

layers thick laminate was noted to result in 2.7% temperature overshoot and 2.1% variation in final laminate thickness. These results show the limitations of using the modified curing process for processing thicker laminates where higher temperature overshoots are encountered and larger thickness variations are faced.

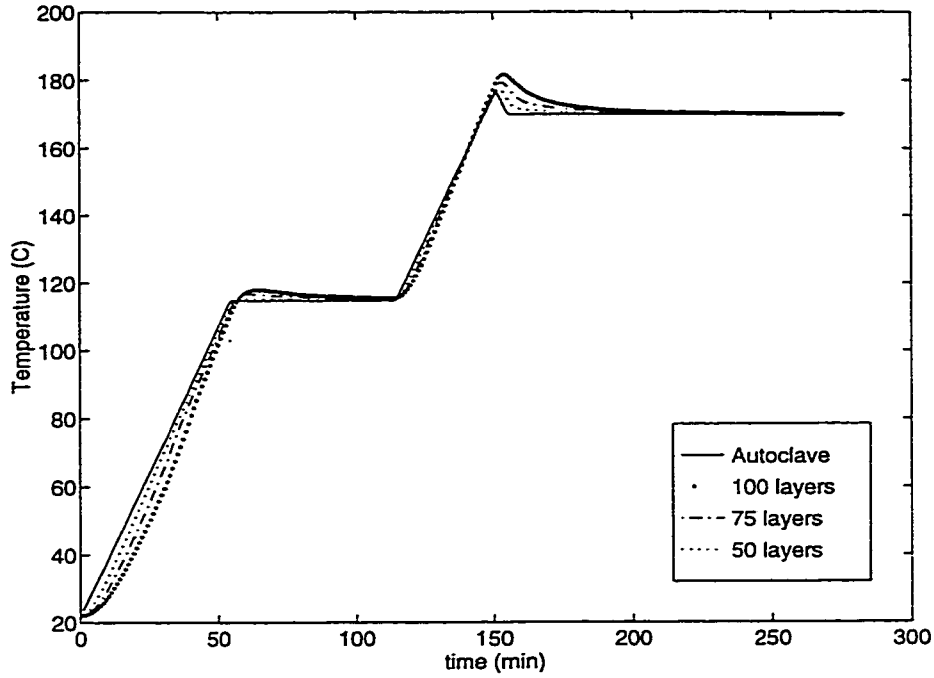


Figure 5.23: Temperature variation for laminates of different thicknesses processed with the modified cure process Case(I).

## 5.4 Comparison with Experiment

Experiments were done in order to investigate the modified cure process suggested above. A 50 layers sample was prepared from Hercules AS4/3501-6 prepreg and cured using the 2–step modified curing process. Two (2) perforated release films were laid at the top surface of the laminate. Two bleeder layers were laid at the

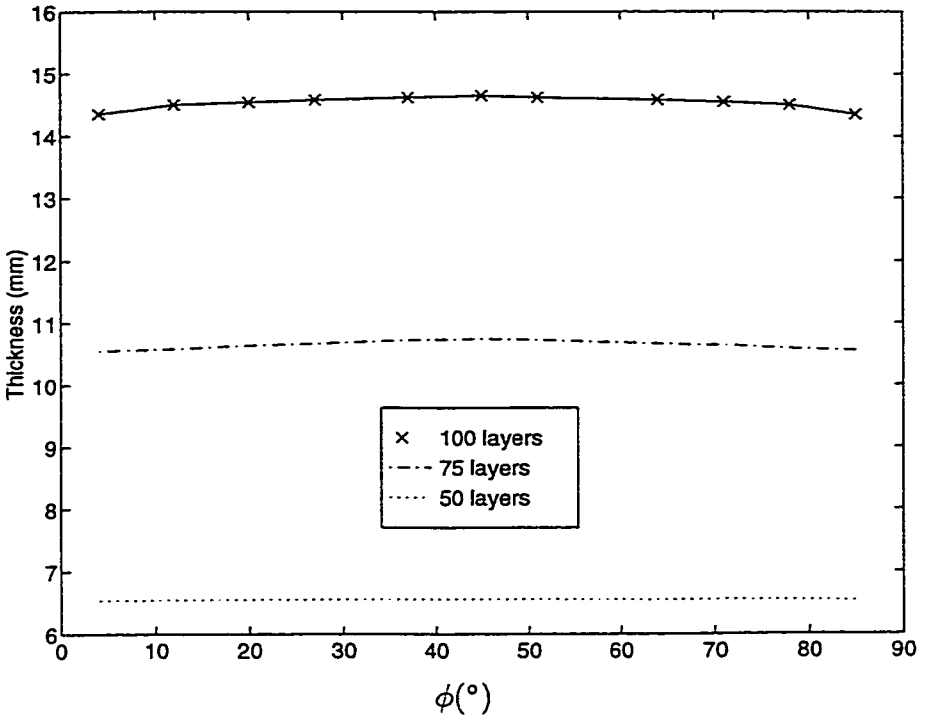


Figure 5.24: Thickness variation for laminates of different thicknesses processed with the modified cure process Case(I).

top surface of the mold (under the laminate) as shown in Figure 5.25. One covers the mold surface from $\phi = 20o$ to $\phi = 70o$, and the other one covers the whole mold surface. Two sensors (one is a thermocouple and the other is a DEA sensor) were embedded in the laminate at the curved bend at $l$=1 and $l$=1/2 (also shown in Figure 5.25). The sensor at $l$=1/2 was attached to a DEA Instrument to monitor the electrical behavior of the laminate with time. A photo of the part is shown in Figure 5.26.

Model and experimental results for temperature measurements at top ($l$=1) and middle ($l$=1/2) points are shown in Figure 5.27. The predicted temperatures are in good agreement with measured ones with higher differences at the start of the first hold period. The peak temperatures at second hold period are almost the same for both model and experiment.

The final thickness after curing was $7mm$ as shown in Figure 5.28 (maximum 1% difference). The laminate was cut and prepared for microscopic inspection. The photomicrographs at different sections and locations across the thickness are shown in Figures 5.29 and 5.30. From the cross-section examination (and as seen in these photos), fibers were uniformly distributed throughout the thickness. Using area method, the fiber volume fraction $v_f$ was measured and found to be in the range between 64.0% and 65.3% all over the laminate. In Figure 5.31, $v_f$ at different sections is plotted against $l$.

It was noted that the surface finish of the bottom surface obtained using this modified process has a different appearance than that obtained without utilizing

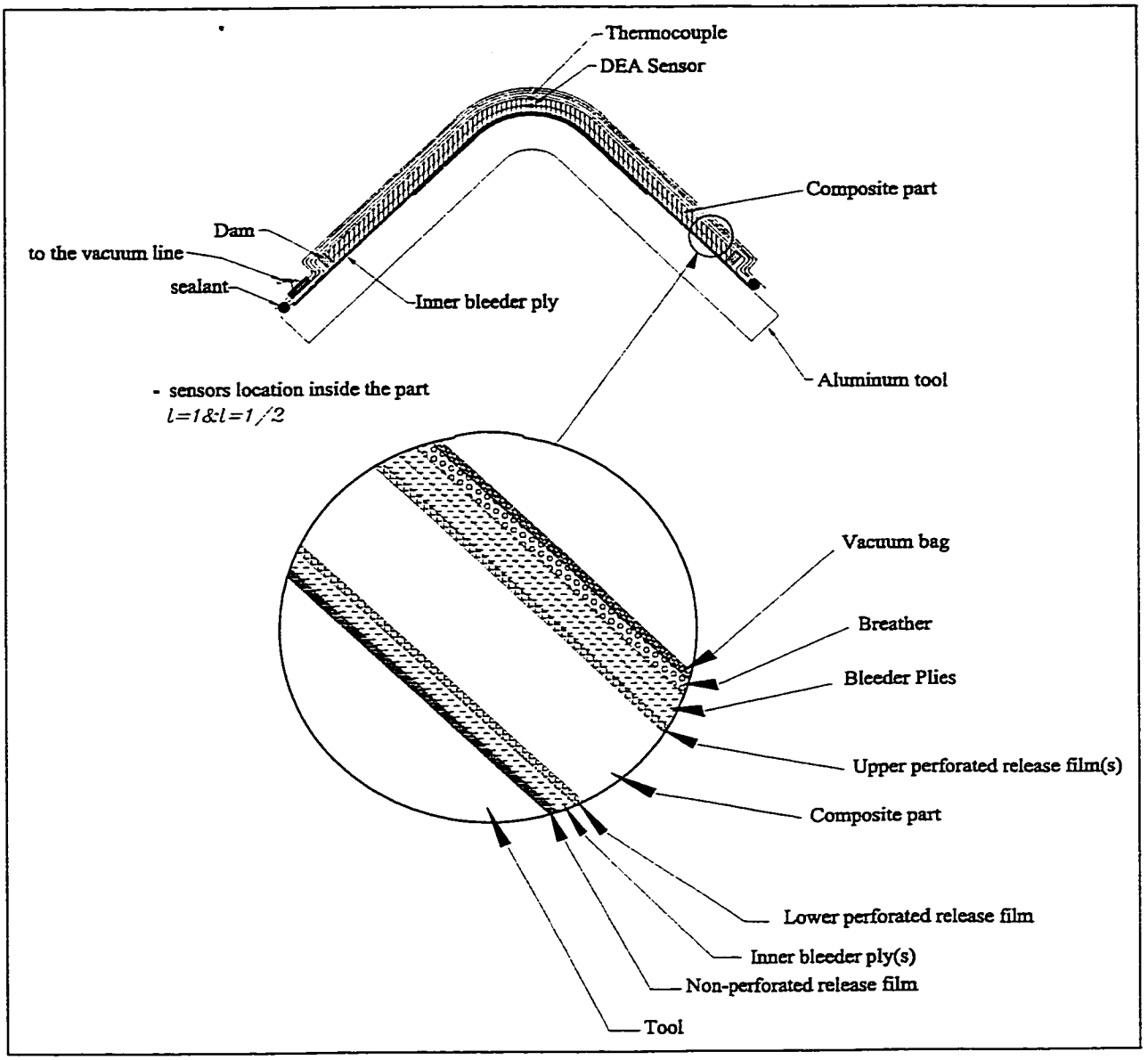


Figure 5.25: Schematic drawing showing the location of the temperature and DEA sensors used in the experiment.

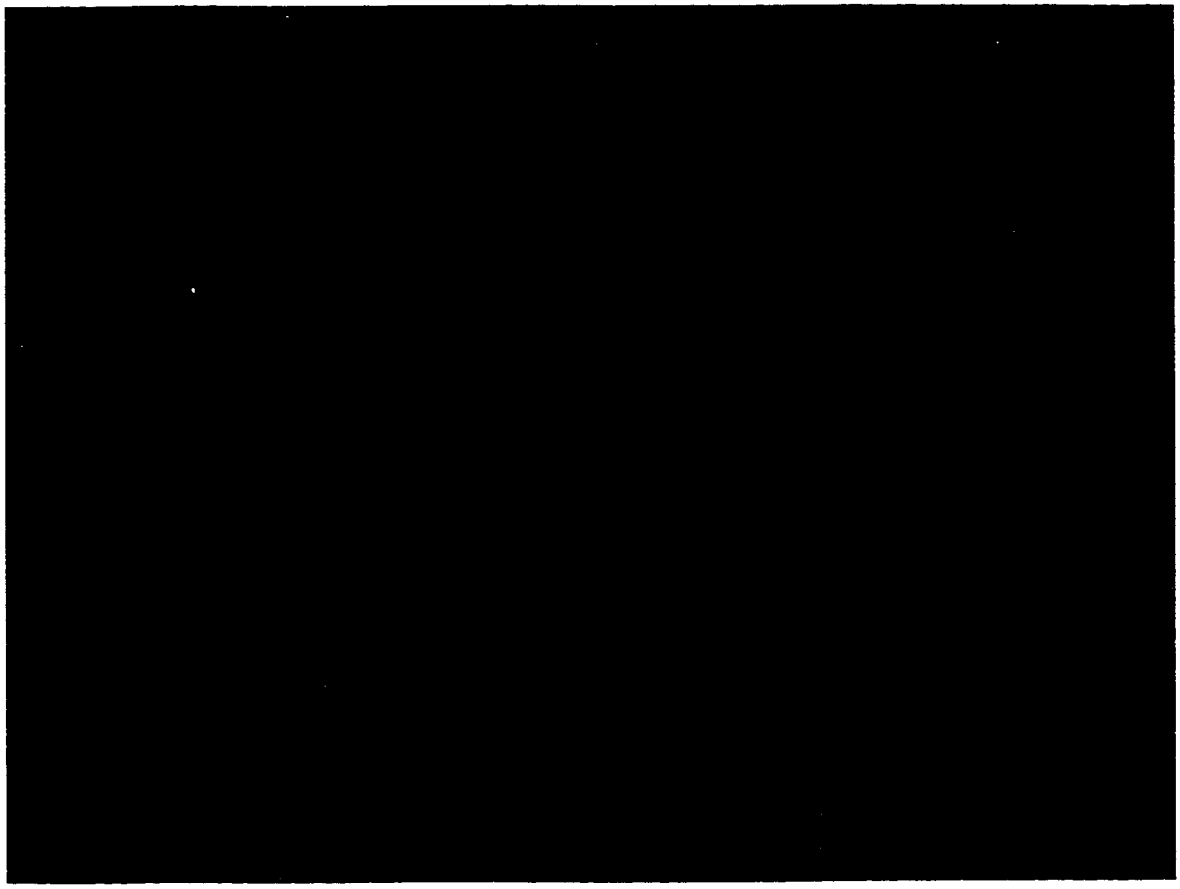

Figure 5.26: Photo shows the part processed with the 2–step modified process.

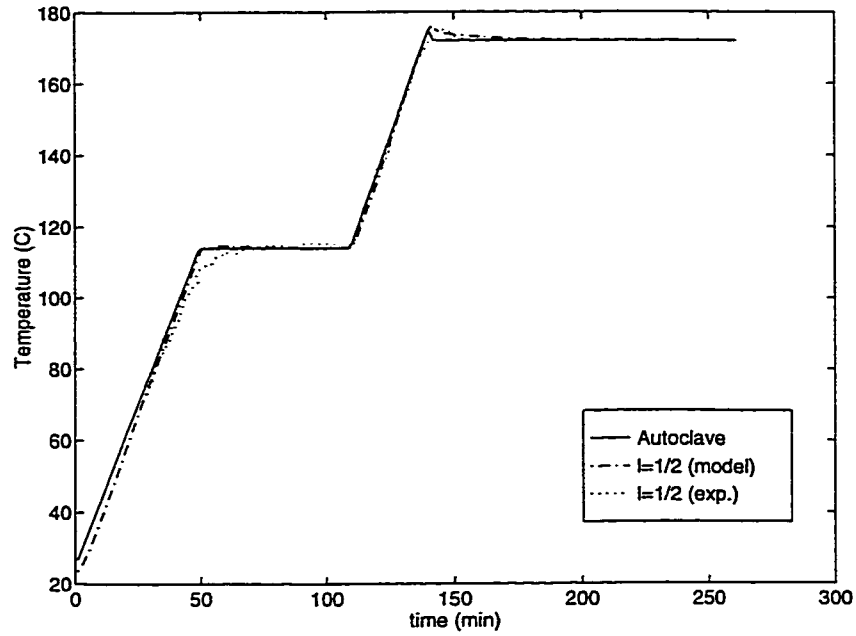


(a) at $l$=1/2

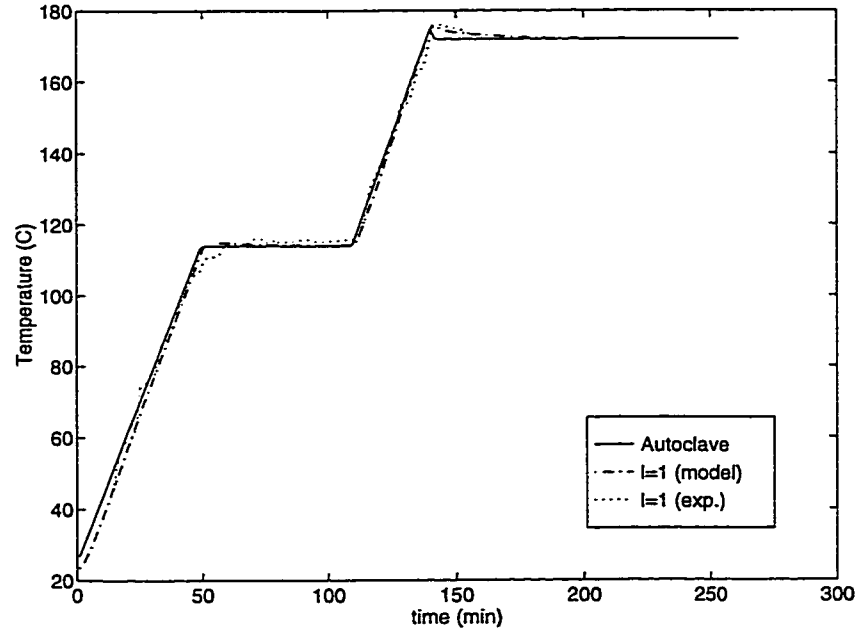


(b) at $l$=1

Figure 5.27: Temperature variation with time obtained from experiment and model for section 6.

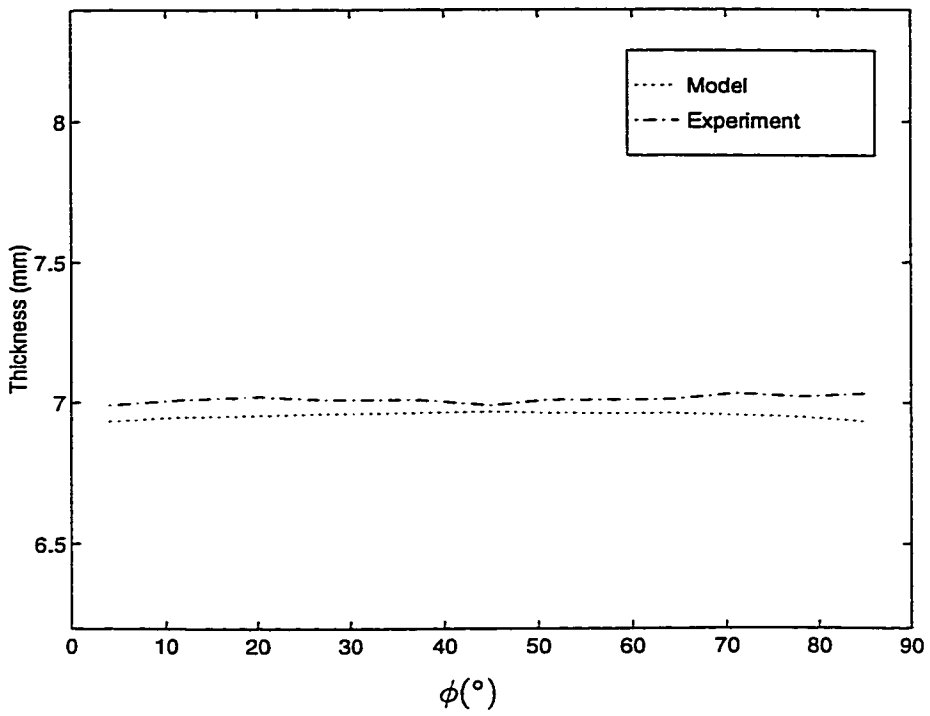


Figure 5.28: Thickness variation along the laminate length obtained from the 2–step modified cure process Case(I).

a bleeder layer at the mold surface. The surface with inner bleeder layer was not smooth and shiny as shown in the photo shown in Figure 5.32. Hence, on one hand, incorporating a bleeder layer at the lower surface of the laminate would produce a high quality part in terms of uniform thickness and fiber volume fraction distribution. On the other hand, a sacrifice is made on the appearance of the surface finish of the bottom surface.

## 5.5 Corner Strength

The same setup shown in Figure 4.34 was used to measure the corner strength in terms of opening it. In Figure 5.33, the load displacement curve for the sample

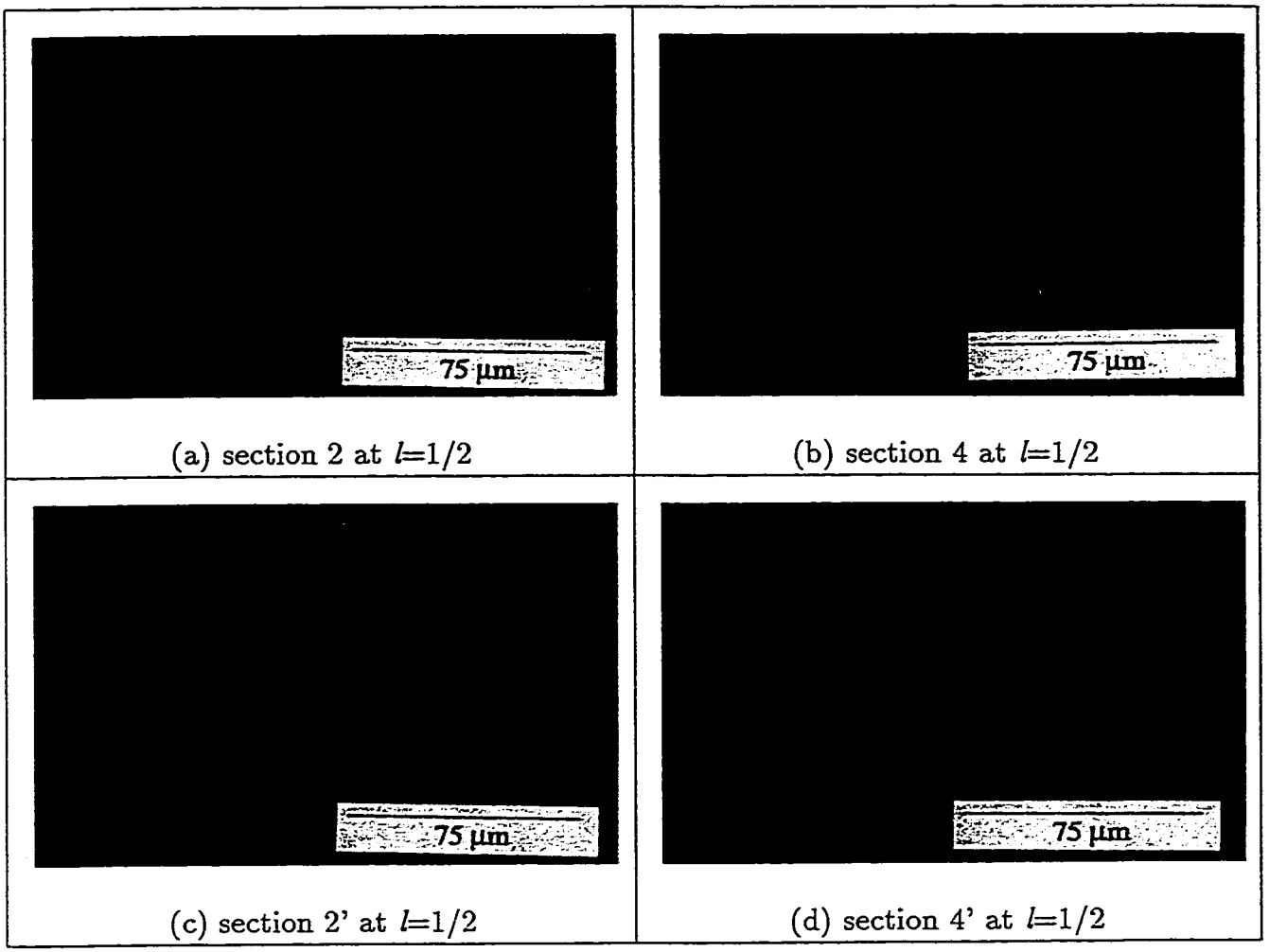


(a) section 2 at $l$=1/2 (b) section 4 at $l$=1/2

(c) section 2' at $l$=1/2 (d) section 4' at $l$=1/2

Figure 5.29: Cross–section photomicrographs ($600X$) obtained for the sample cured with the 2–step modified curing process.

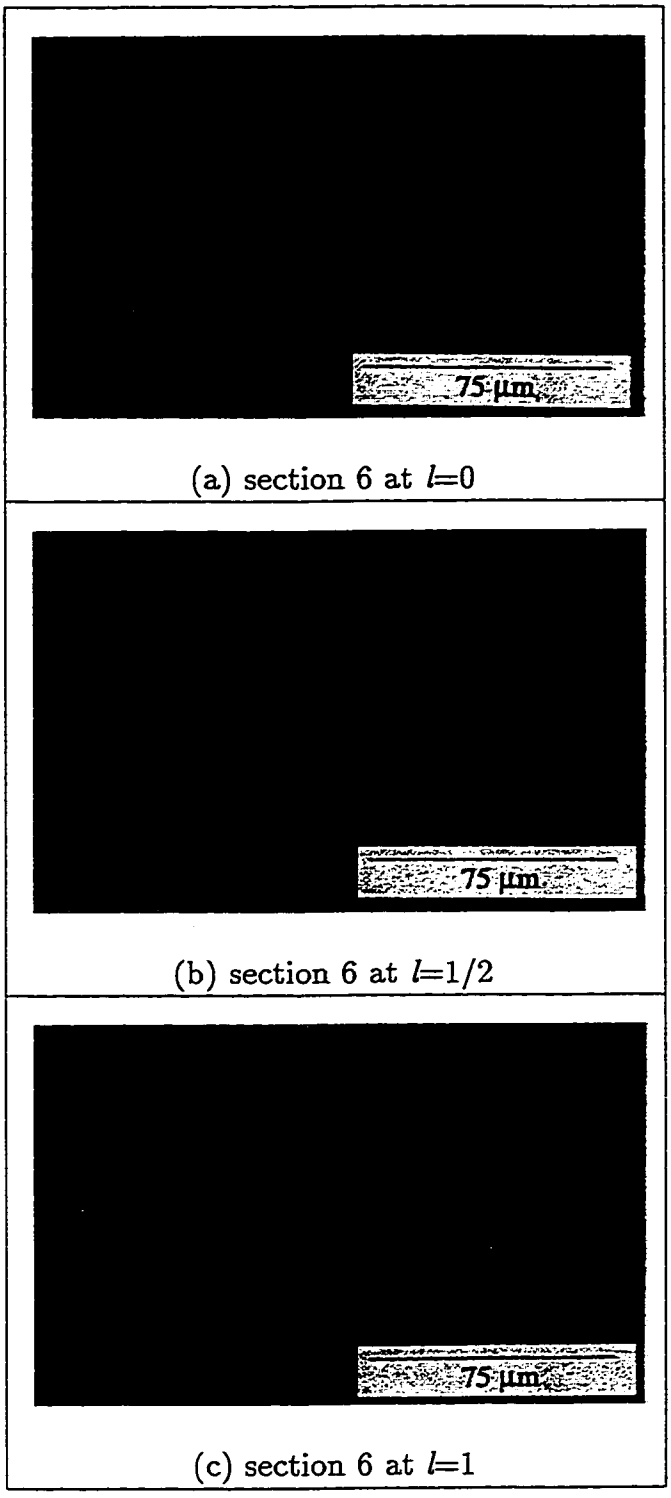


(a) section 6 at $l$=0

(b) section 6 at $l$=1/2

(c) section 6 at $l$=1

Figure 5.30: More cross–section photomicrographs ($600X$) obtained for the sample cured with the 2–step modified curing process.

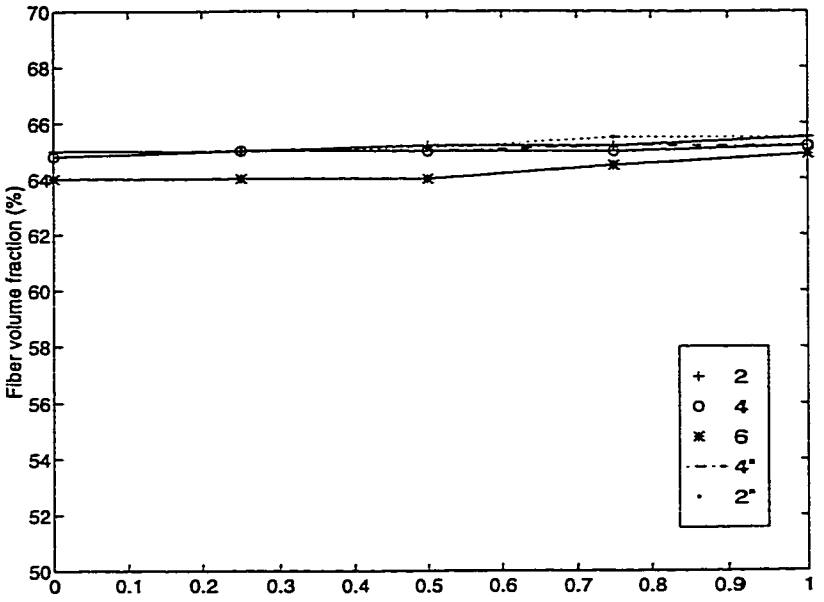


$\phi(°)$

Figure 5.31: $v_f$ variation across the thickness obtained from experiment for the 2–step modified process.

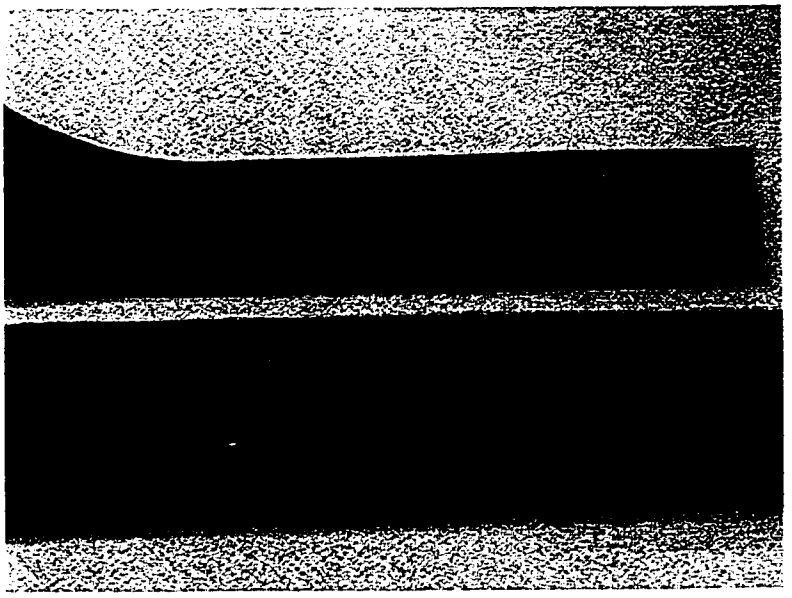

Figure 5.32: Photo shows the difference in surface texture obtained utilizing the conventional processing method (upper part) and utilizing the modified curing process (lower part).

shows a linear increase in load up to a point where it continues to increase but at a lower rate. Also, Figure 5.34 shows the location of the initial crack. Table 5.1 lists

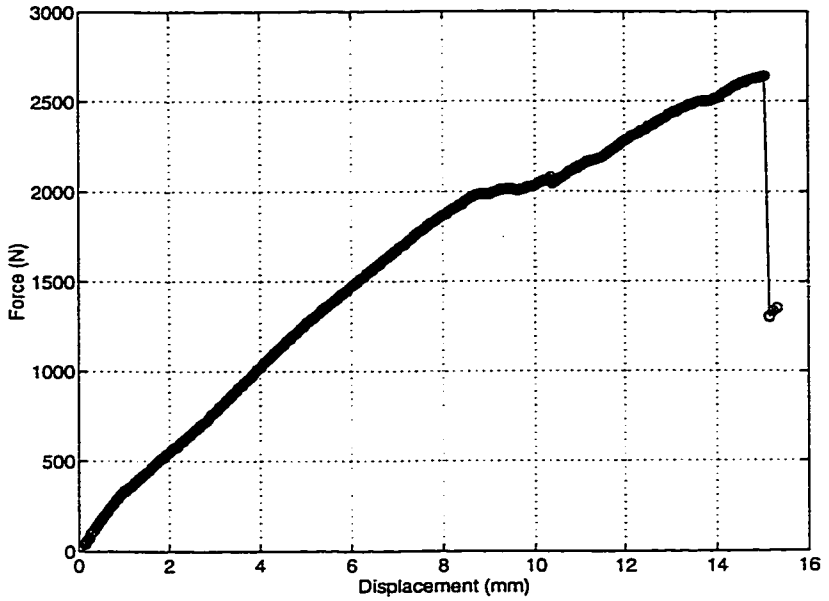


Figure 5.33: Load–Displacement curve for the sample manufactured using the modified curing process.

the data obtained from this experiment and previous experiments.

| Sample # | $A$ $mm^2$ | $F$ (N) | $\sigma$ (N/$mm^2$) | Slope (N/mm) | $\delta$ (N) | d (mm) | $l_d$ |
|---|---|---|---|---|---|---|---|
| 2 | 173.4 | 1061 | 5.98 | 272 | 180 | 4.21 | 0.40 |
| 3 | 141.5 | 923 | 6.77 | 233 | 194 | 4.31 | 0.35 |
| 4 | 164.0 | 1600 | 9.76 | 254 | 49 | 7.28 | 0.65 |
| 5 | 139.5 | 1075 | 8.44 | 202 | – | 5.88 | 0.81 |
| **Modified** | **129.5** | **2640** | **20.38** | **226** | **1335** | **15.0** | **0.44** |

Table 5.1: Load–displacement results for the sample processed using the modified curing process and samples processed using the recommended curing cycles.

Results for the sample processed using the modified one show enhanced properties in terms of load and displacement at failure. These high values of maximum

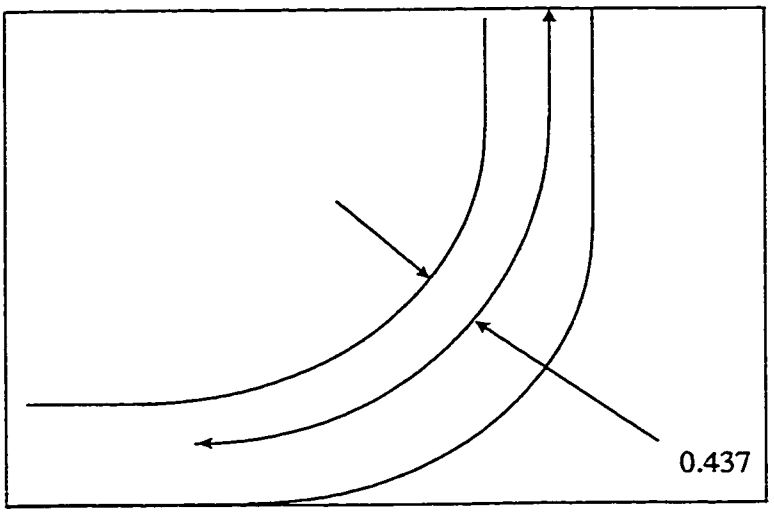


Figure 5.34: Location of fracture initiation in the strength experiment.

load and displacement up to initial failure were obtained as a result of not having any premature crack before the major delamination initiation site that was shown in Figure 5.34. After this point, the load dropped dramatically (compared to other samples) with large $\delta$ value. For the other samples, there were matrix premature failures at resin–rich areas before the major one occurred. This behavior for the modified sample was expected since the modified process produced a part that has a uniform thickness and fiber volume fraction.

## 5.6 Degree of Cure

Following the same proceedure as was done in section 4.5, the *cure index* was generated and compared to $\alpha$. The log(conductivity) variation with time is shown in Figure 5.35, and its variation with temperature is shown in Figure 5.36. As mentioned before, the ionic conductivity is a direct measure of the mobility of particles

in the medium. Figure 5.35 shows a similar behavior as that disscussed in section 4.5. From these data, the following 0% and 100% temperature dependencies were estimated:

$$\begin{aligned} 0\% \quad (\text{un}-\text{cured}): \quad & LC = 0.0284 * T + 3.1767 \\ 100\% \quad (\text{cured}): \quad & LC = 0.094 * T - 0.9801 \end{aligned} \tag{5.1}$$

Hence, the cure index can be calculated from:

$$\text{Cure Index} = \frac{LC - (0.0284 * T + 3.1767)}{(0.094 * T - 0.9801) - (0.0284 * T + 3.1767)} \tag{5.2}$$

Figure 5.37 shows the cure index and the degree of cure obtained from simulation. It shows that experiment and simulation compare well at the start of cure but are different at the end.

## 5.7 Conclusions

This chapter demonstrated modification of the curing process to get a good quality part. This includes control of the temperature peak exotherm, uniform thickness distribution and uniform $v_f$ distribution. Temperature exotherm was controlled by modifying the curing process through decreasing the last hold temperature after the maximum temperature has been reached. Furthermore, thickness variations over the part length were negligible and a uniform thickness was obtained. This was possible through modifying the curing process by incorporating bleeder layers at the lower surface between the mold and the sample. This extra layer was able to

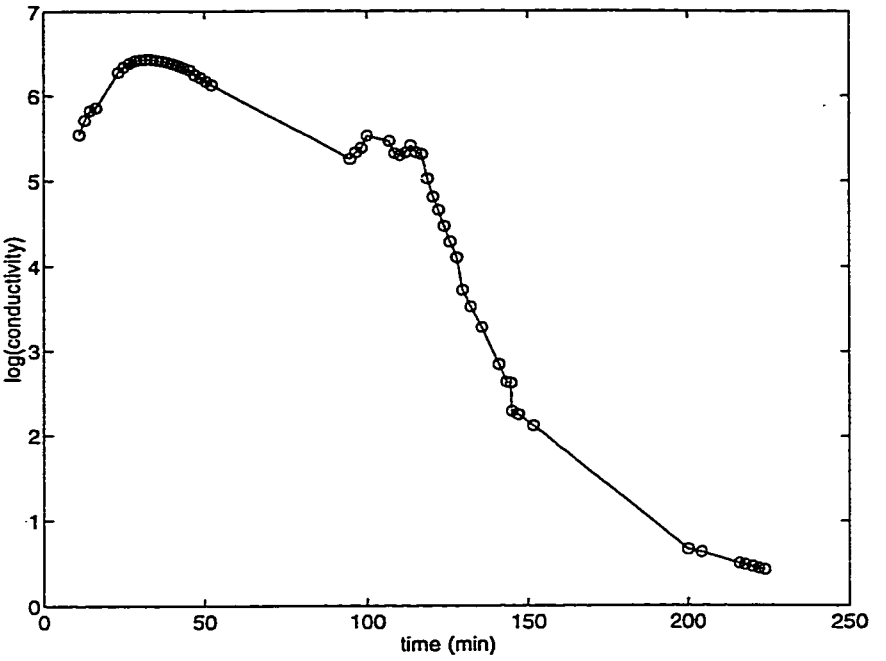


Figure 5.35: log(Conductivity) vs time obtained from experimental results for the modified curing process.

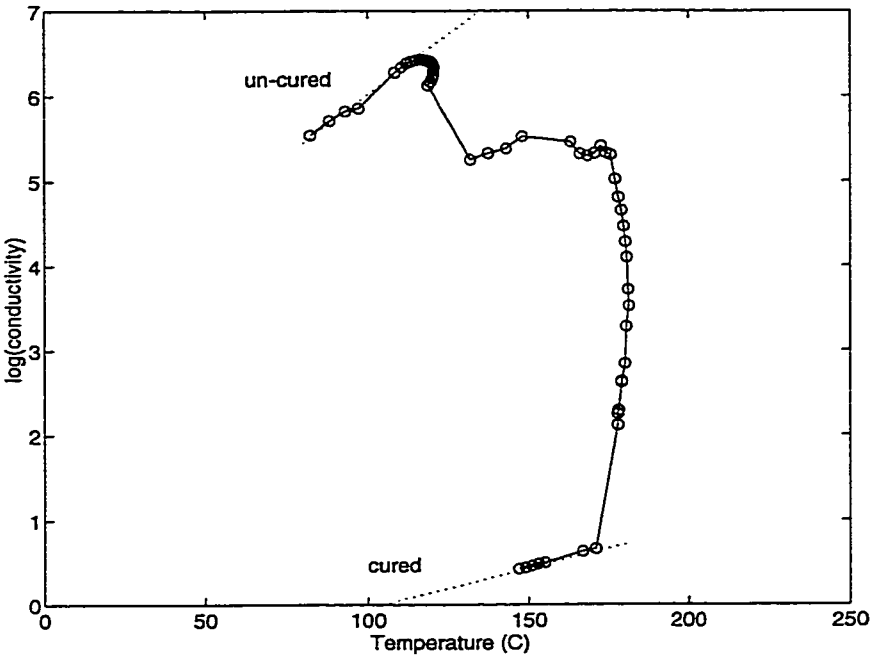


Figure 5.36: log(Conductivity) vs temperature obtained from experimental results for the modified curing process.

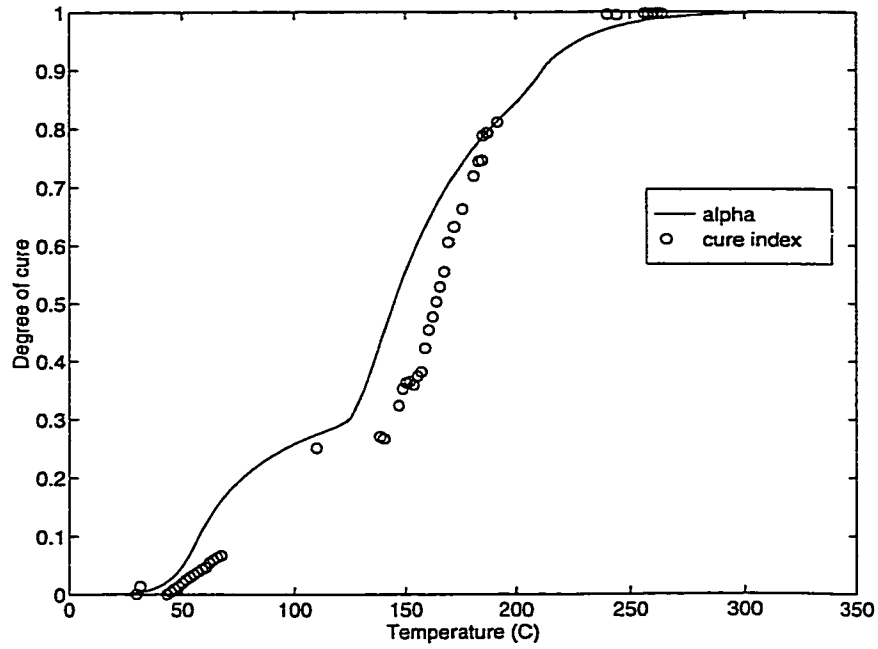


Figure 5.37: Cure Index and degree of cure vs time.

absorb the resin and hence decreasing the thickness and increasing the fiber volume fraction. However, the surface finish was not of the same appearance as that of a part processed without this extra layer.

Manufacturing a composite part with minimum variations in thickness and fiber volume fraction showed that mechanical strength was also enhanced. This achievement was on the bases of getting very high values of load and displacement up to the initial matrix failure. Furthermore, no premature cracks were observed before the major delamination initiation site.

# Chapter 6

# Conclusions and Contributions

The fundamental objective of the present work was to develop a method for manufacturing good composite curved parts. First, the investigation of the problems associated with manufacturing thick curved thermoset composite parts following the manufacturers recommended curing cycles was done. A two–dimensional anisotropic cure simulation code was developed to assist in predicting the thermal, chemical and flow behavior of the part through the different models that govern composites processing. A generalized boundary condition formulation for both temperature and pressure was found to help identifying the effect of tool and different bagging materials on the curing process. Further, this generalized formulation helped in reducing computational time and effort by replacing tool and bagging material modeling with one generalized boundary condition.

The general model consists of (1) thermal analysis to determine the time dependent temperature distribution over the cross–sectional area of the laminate, and

(2) resin flow analysis to predict the fiber volume fraction distribution and the final laminate thickness over the laminate length. Both analysis were solved simultaneously at every instant to obtain the different parameters during the cure process. To enable dealing with irregular geometries, the boundary fitted coordinate technique was utilized. Also, finite difference method was used to solve the resulted governing equations.

## 6.1 General Findings

- Curing of thick thermosetting composites with angle–bend was done following the recommended 2–step and 3–step curing cycles. The samples obtained were examined to investigate the part quality in terms of fiber volume fraction distribution across the thickness, and also in terms of the thickness variation along the laminate length. The results showed that resin flow out of the laminate was non–uniform resulting in a non–uniform fiber volume fraction distribution. Also, thickness variation over the laminate length was observed where thickness was greater at the bend than the straight edges.

- Results also showed that the final quality was strongly affected by the processing parameters (cure cycle temperature and time) and processing procedure (lay–up sequence). Restricting the resin flow out of the laminate was shown to have more effect on the part quality than the processing parameters themselves. When no restriction was imposed on resin flow, the effect of processing

parameters was more pronounced.

- Based on the experimental and theoretical results, a modified curing process was suggested and tested. The experiment was done and the results were satisfactory. The part processed with this modified cycle was in good quality in terms of having uniform fiber distribution over the laminate cross-section, and in terms of having uniform thickness along the laminate length. This success was a result of accurately modeling the boundary conditions related to resin flow and pressure build–up.

- The angle enclosed in the curved parts was measured and compared to the angle of the tool. A difference was observed due to the 'Spring In' effect induced by the difference in thermal expansion between in–plane and out–of–plane coefficients. The maximum difference was 0.86%. This low value was referred to the type of tooling, release film used, and due to the fact that the application of autoclave pressure was continued even after the curing cycle has finished which acted as a stress relief agent.

- Corner strength experiments were conducted to investigate the effect of different curing processes on the opening strength of the curved laminates. Indeed, there was a big difference in strength and displacement values between the samples since their processing conditions were different. These values were maximum when a good quality part was obtained through the modified curing process.

## 6.2 Contributions

- A new modified curing process has been developed to manufacture good quality composite parts with angle bend. This was done successfully through the simulation and through the experiment. The part obtained was of a uniform thickness and uniform fiber volume fraction.

- The temperature overshoot associated with processing thick composite laminates was minimized by following a modified curing cycle. The last holding temperature in this cycle is done after increasing the cycle temperature to one that is below the maximum recommended temperature and then decreasing it to the holding temperature at the recommended rate.

- The development of a generalized pressure boundary condition to quantify the resin flow out of the laminate was done. This was necessary to overcome the difficulty in modeling the resin flow through the peel, bleeder and other layers. A flow coefficient that accounts for the flow resistance associated with the different bagging materials was defined. The resulted generalized boundary condition form was analogous to that used for temperature boundary condition formulation. This form is practical in the way it is easy to apply numerically (only coefficients a, b and c have to be manipulated), and more realistic boundary conditions can be simulated. The generalized pressure boundary condition was easily imposed on the numerical code where experimental cases were tested. Experiments with different processing parameters were conducted

and results were compared. In doing so, the experimental work was in a good agreement with simulation results.

- The thickness and fiber volume fraction variations obtained for parts processed following the recommended curing cycles were eliminated by incorporating a bleeder cloth between the laminate and mold surfaces. The resulted laminate was of uniform thickness and uniform fiber volume fraction. Also, the corner strength was much higher than that obtained for the other laminates.

## 6.3 Recommendations for Future Work

It would be of great interest to implement the proposed procedure in processing parts with thickness variations, and to investigate the effect of fiber orientation and laminate sequence on the final thickness and fiber volume fraction of the part.

The implication of the pressure boundary condition can be extended to laminates of variable geometries such as the ply–drop geometry, where resin flow from one side can vary due to the difference in laminate thickness.

More comprehensive study is required to investigate the development of thermal stresses induced by processing parameters. Also, stress relieving techniques should be investigated to minimize the 'Spring In' effect experienced in curved laminates.

# Appendix A

# Numerical Equation Representation

## A.1 Laplacian Equations

The finite difference equations representing equation 3.2 for $x$ and $z$ are as follows:

$$\begin{aligned} &\wp_{i,j}\left[x_{i+1,j} - 2x_{i,j} + x_{i-1,j}\right] \\ &-2\beta_{i,j}\left[x_{i+1,j+1} - x_{i+1,j-1} - x_{i-1,j+1} + x_{i-1,j-1}\right] \\ &+\gamma_{i,j}\left[x_{i,j+1} - 2x_{i,j} + x_{i,j-1}\right] = 0 \end{aligned} \tag{A.1}$$

and

$$\begin{aligned} &\wp_{i,j}\left[z_{i+1,j} - 2z_{i,j} + z_{i-1,j}\right] \\ &-2\beta_{i,j}\left[z_{i+1,j+1} - z_{i+1,j-1} - z_{i-1,j+1} + z_{i-1,j-1}\right] \\ &+\gamma_{i,j}\left[z_{i,j+1} - 2z_{i,j} + z_{i,j-1}\right] = 0 \end{aligned} \tag{A.2}$$

where

$$\begin{aligned}
\wp_{i,j} &= \left[\left(\tfrac{x_{i,j+1}-x_{i,j-1}}{2}\right)^2 + \left(\tfrac{z_{i,j+1}-z_{i,j-1}}{2}\right)^2\right] \\
\beta_{i,j} &= \left[\left(\tfrac{x_{i+1,j}-x_{i-1,j}}{2}\right)\left(\tfrac{x_{i,j+1}-x_{i,j-1}}{2}\right) + \left(\tfrac{z_{i+1,j}-z_{i-1,j}}{2}\right)\left(\tfrac{z_{i,j+1}-z_{i,j-1}}{2}\right)\right] \\
\gamma_{i,j} &= \left[\left(\tfrac{x_{i+1,j}-x_{i-1,j}}{2}\right)^2 + \left(\tfrac{z_{i+1,j}-z_{i-1,j}}{2}\right)^2\right]
\end{aligned} \tag{A.3}$$

## A.2 Cross-derivatives

The cross-derivatives necessary for obtaining the partial derivatives of the governing equations are:

$$\begin{aligned}
\tfrac{\partial \xi}{\partial \xi} = 1 &= \tfrac{\partial \xi}{\partial x}\tfrac{\partial x}{\partial \xi} + \tfrac{\partial \xi}{\partial z}\tfrac{\partial z}{\partial \xi} \\
\tfrac{\partial \xi}{\partial \eta} = 0 &= \tfrac{\partial \xi}{\partial x}\tfrac{\partial x}{\partial \eta} + \tfrac{\partial \xi}{\partial z}\tfrac{\partial z}{\partial \eta}
\end{aligned} \tag{A.4}$$

from which we get:

$$\begin{Bmatrix} 1 \\ 0 \end{Bmatrix} = \begin{bmatrix} \frac{\partial x}{\partial \xi} & \frac{\partial z}{\partial \xi} \\ \frac{\partial x}{\partial \eta} & \frac{\partial z}{\partial \eta} \end{bmatrix} \begin{Bmatrix} \frac{\partial \xi}{\partial x} \\ \frac{\partial \xi}{\partial z} \end{Bmatrix}$$

Upon inversion, this equation becomes:

$$\begin{Bmatrix} \frac{\partial \xi}{\partial x} \\ \frac{\partial \xi}{\partial z} \end{Bmatrix} = \frac{1}{J} \begin{bmatrix} \frac{\partial z}{\partial \eta} & -\frac{\partial z}{\partial \xi} \\ -\frac{\partial x}{\partial \eta} & \frac{\partial x}{\partial \xi} \end{bmatrix} \begin{Bmatrix} 1 \\ 0 \end{Bmatrix} \tag{A.5}$$

In a similar way, the derivatives of $\eta$ with respect to $x$ and $z$ are obtained. Namely:

$$\begin{aligned}
\tfrac{\partial \eta}{\partial \xi} = 0 &= \tfrac{\partial \eta}{\partial x}\tfrac{\partial x}{\partial \xi} + \tfrac{\partial \eta}{\partial z}\tfrac{\partial z}{\partial \xi} \\
\tfrac{\partial \eta}{\partial \eta} = 1 &= \tfrac{\partial \eta}{\partial x}\tfrac{\partial x}{\partial \eta} + \tfrac{\partial \eta}{\partial z}\tfrac{\partial z}{\partial \eta}
\end{aligned}$$

or

$$\begin{Bmatrix} 0 \\ 1 \end{Bmatrix} = \begin{bmatrix} \frac{\partial x}{\partial \xi} & \frac{\partial z}{\partial \xi} \\ \frac{\partial x}{\partial \eta} & \frac{\partial z}{\partial \eta} \end{bmatrix} \begin{Bmatrix} \frac{\partial \eta}{\partial x} \\ \frac{\partial \eta}{\partial z} \end{Bmatrix}$$

which upon inversion becomes:

$$\begin{Bmatrix} \frac{\partial \eta}{\partial x} \\ \frac{\partial \eta}{\partial z} \end{Bmatrix} = \frac{1}{J} \begin{bmatrix} \frac{\partial z}{\partial \eta} & -\frac{\partial z}{\partial \xi} \\ -\frac{\partial x}{\partial \eta} & \frac{\partial x}{\partial \xi} \end{bmatrix} \begin{Bmatrix} 0 \\ 1 \end{Bmatrix} \tag{A.6}$$

where

$$J = z_\eta x_\xi - z_\xi x_\eta$$

The results of equations A.5 and A.6 are summarized below:

$$\begin{aligned}
\frac{\partial \xi}{\partial x} &= \frac{1}{J}\left(\frac{\partial z}{\partial \eta}\right) \\
\frac{\partial \xi}{\partial z} &= \frac{1}{J}\left(-\frac{\partial x}{\partial \eta}\right) \\
\frac{\partial \eta}{\partial x} &= \frac{1}{J}\left(-\frac{\partial z}{\partial \xi}\right) \\
\frac{\partial \eta}{\partial z} &= \frac{1}{J}\left(\frac{\partial x}{\partial \xi}\right)
\end{aligned} \tag{A.7}$$

# Appendix B

# Heat and Flow Equations

The transformation of the first term of equation 2.1 is done as follows:

$$
\begin{aligned}
k_{xx}\frac{\partial^2 T}{\partial x^2} &= \frac{\partial}{\partial x}\left(k_{xx}\frac{\partial T}{\partial x}\right) \\
&= \frac{\partial}{\partial x}k_{xx}\left[\frac{\partial \xi}{\partial x}\frac{\partial T}{\partial \xi}+\frac{\partial \eta}{\partial x}\frac{\partial T}{\partial \eta}\right] \\
&= \frac{\partial}{\partial x}k_{xx}\frac{1}{J}\left[\frac{\partial z}{\partial \eta}\frac{\partial T}{\partial \xi}-\frac{\partial z}{\partial \xi}\frac{\partial T}{\partial \eta}\right] \\
&= k_{xx}\left[\frac{\partial \xi}{\partial x}\frac{\partial}{\partial \xi}\left(\frac{\frac{\partial z}{\partial \eta}\frac{\partial T}{\partial \xi}-\frac{\partial z}{\partial \xi}\frac{\partial T}{\partial \eta}}{J}\right)+\frac{\partial \eta}{\partial x}\frac{\partial}{\partial \eta}\left(\frac{\frac{\partial z}{\partial \eta}\frac{\partial T}{\partial \xi}-\frac{\partial z}{\partial \xi}\frac{\partial T}{\partial \eta}}{J}\right)\right] \\
&= \frac{k_{xx}}{J^2}\left[\frac{\partial z}{\partial \eta}\left(\frac{\partial z}{\partial \eta}\frac{\partial^2 T}{\partial \xi^2}+\frac{\partial^2 z}{\partial \xi \partial \eta}\frac{\partial T}{\partial \xi}-\frac{\partial^2 z}{\partial \xi^2}\frac{\partial T}{\partial \eta}-\frac{\partial z}{\partial \xi}\frac{\partial^2 T}{\partial \xi \partial \eta}\right)\right. \\
&\quad \left.-\frac{\partial z}{\partial \xi}\left(\frac{\partial^2 z}{\partial \eta^2}\frac{\partial T}{\partial \xi}+\frac{\partial z}{\partial \eta}\frac{\partial^2 T}{\partial \xi \partial \eta}-\frac{\partial^2 z}{\partial \xi \partial \eta}\frac{\partial T}{\partial \eta}-\frac{\partial z}{\partial \xi}\frac{\partial^2 T}{\partial \eta^2}\right)\right] \\
&\quad +\frac{k_{xx}}{J^2}\left[\frac{\partial z}{\partial \eta}\left(\frac{\partial z}{\partial \eta}\frac{\partial T}{\partial \xi}-\frac{\partial z}{\partial \xi}\frac{\partial T}{\partial \eta}\right)\left(\frac{-\partial J/\partial \xi}{J}\right)+\frac{\partial z}{\partial \xi}\left(\frac{\partial z}{\partial \eta}\frac{\partial T}{\partial \xi}-\frac{\partial z}{\partial \xi}\frac{\partial T}{\partial \eta}\right)\left(\frac{\partial J/\partial \eta}{J}\right)\right]
\end{aligned}
\tag{B.1}
$$

Also, the second term is transformed as follows:

$$
\begin{aligned}
2k_{xz}\frac{\partial^2 T}{\partial x \partial z} &= 2k_{xz}\frac{\partial}{\partial z}\frac{1}{J}\left[\frac{\partial z}{\partial \eta}\frac{\partial T}{\partial \xi}-\frac{\partial z}{\partial \xi}\frac{\partial T}{\partial \eta}\right] \\
&= 2k_{xz}\left[\frac{\partial \xi}{\partial z}\frac{\partial}{\partial \xi}\left(\frac{\frac{\partial z}{\partial \eta}\frac{\partial T}{\partial \xi}-\frac{\partial z}{\partial \xi}\frac{\partial T}{\partial \eta}}{J}\right)+\frac{\partial \eta}{\partial z}\frac{\partial}{\partial \eta}\left(\frac{\frac{\partial z}{\partial \eta}\frac{\partial T}{\partial \xi}-\frac{\partial z}{\partial \xi}\frac{\partial T}{\partial \eta}}{J}\right)\right] \\
&= \frac{2k_{xz}}{J^2}\left[\frac{\partial z}{\partial \eta}\left(\frac{\partial^2 z}{\partial \xi \partial \eta}\frac{\partial T}{\partial \xi}+\frac{\partial z}{\partial \eta}\frac{\partial^2 T}{\partial \xi^2}-\frac{\partial^2 z}{\partial \xi^2}\frac{\partial T}{\partial \eta}-\frac{\partial z}{\partial \xi}\frac{\partial^2 T}{\partial \xi \partial \eta}\right)\right. \\
&\quad \left.+\frac{\partial x}{\partial \xi}\left(\frac{\partial^2 z}{\partial \eta^2}\frac{\partial T}{\partial \xi}+\frac{\partial z}{\partial \eta}\frac{\partial^2 T}{\partial \xi \partial \eta}-\frac{\partial^2 z}{\partial \xi \partial \eta}\frac{\partial T}{\partial \eta}-\frac{\partial z}{\partial \xi}\frac{\partial^2 T}{\partial \eta^2}\right)\right] \\
&\quad +\frac{2k_{xz}}{J^2}\left[\frac{\partial x}{\partial \eta}\left(\frac{\partial z}{\partial \eta}\frac{\partial T}{\partial \xi}-\frac{\partial z}{\partial \xi}\frac{\partial T}{\partial \eta}\right)\left(\frac{\partial J/\partial \xi}{J}\right)+\frac{\partial x}{\partial \xi}\left(\frac{\partial z}{\partial \eta}\frac{\partial T}{\partial \xi}-\frac{\partial z}{\partial \xi}\frac{\partial T}{\partial \eta}\right)\left(\frac{-\partial J/\partial \eta}{J}\right)\right]
\end{aligned}
\tag{B.2}
$$

Finally, the third term in equation is transformed as:

$$\begin{aligned}
k_{xz}\frac{\partial^2 T}{\partial z^2} &= \frac{\partial}{\partial z}k_{zz}\left[\frac{\partial \xi}{\partial z}\frac{\partial T}{\partial \xi}+\frac{\partial \eta}{\partial z}\frac{\partial T}{\partial \eta}\right] \\
&= k_{zz}\frac{\partial}{\partial z}\frac{1}{J}\left[-\frac{\partial x}{\partial \eta}\frac{\partial T}{\partial \xi}+\frac{\partial x}{\partial \xi}\frac{\partial T}{\partial \eta}\right] \\
&= k_{zz}\left[\frac{\partial \xi}{\partial z}\frac{\partial}{\partial \xi}\left(\frac{-\frac{\partial x}{\partial \eta}\frac{\partial T}{\partial \xi}+\frac{\partial x}{\partial \xi}\frac{\partial T}{\partial \eta}}{J}\right)+\frac{\partial \eta}{\partial z}\frac{\partial}{\partial \eta}\left(\frac{-\frac{\partial x}{\partial \eta}\frac{\partial T}{\partial \xi}+\frac{\partial x}{\partial \xi}\frac{\partial T}{\partial \eta}}{J}\right)\right] \\
&= \frac{k_{zz}}{J^2}\left[-\frac{\partial x}{\partial \eta}\left(-\frac{\partial^2 x}{\partial \xi \partial \eta}\frac{\partial T}{\partial \xi}-\frac{\partial x}{\partial \eta}\frac{\partial^2 T}{\partial \xi^2}+\frac{\partial^2 x}{\partial \xi^2}\frac{\partial T}{\partial \eta}+\frac{\partial x}{\partial \xi}\frac{\partial^2 T}{\partial \xi \partial \eta}\right)\right. \\
&+\frac{\partial x}{\partial \xi}\left(-\frac{\partial^2 x}{\partial \eta^2}\frac{\partial T}{\partial \xi}-\frac{\partial x}{\partial \eta}\frac{\partial^2 T}{\partial \xi \partial \eta}+\frac{\partial^2 x}{\partial \xi \partial \eta}\frac{\partial T}{\partial \eta}+\frac{\partial x}{\partial \xi}\frac{\partial^2 T}{\partial \eta^2}\right) \\
&\left.+\frac{\partial x}{\partial \eta}\left(-\frac{\partial x}{\partial \eta}\frac{\partial T}{\partial \xi}+\frac{\partial x}{\partial \xi}\frac{\partial T}{\partial \eta}\right)\left(\frac{\partial J/\partial \xi}{J}\right)+\frac{\partial x}{\partial \xi}\left(-\frac{\partial x}{\partial \eta}\frac{\partial T}{\partial \xi}+\frac{\partial x}{\partial \xi}\frac{\partial T}{\partial \eta}\right)\left(\frac{-\partial J/\partial \eta}{J}\right)\right]
\end{aligned} \tag{B.3}$$

Combining equations B.1, B.2 and B.3 the following is obtained:

$$\mathcal{A}_1\frac{\partial^2 T}{\partial \xi^2}+\mathcal{A}_2\frac{\partial^2 T}{\partial \eta^2}+\mathcal{A}_3\frac{\partial^2 T}{\partial \xi \partial \eta}+\mathcal{A}_4\frac{\partial T}{\partial \xi}+\mathcal{A}_5\frac{\partial T}{\partial \eta}+\dot{q}=\rho c_v\frac{\partial T}{\partial t} \tag{B.4}$$

where,

$$\begin{aligned}
\mathcal{A}_1 &= (k_{xx}z_\eta^2-2k_{xz}x_\eta z_\eta+k_{zz}x_\eta^2)/J^2 \\
\mathcal{A}_2 &= (k_{xx}z_\xi^2-2k_{xz}x_\xi z_\xi+k_{zz}x_\xi^2)/J^2 \\
\mathcal{A}_3 &= [-2k_{xx}z_\eta z_\xi-2k_{zz}x_\xi x_\eta+2k_{xz}(x_\xi z_\eta+x_\eta z_\xi)]/J^2 \\
\mathcal{A}_4 &= (k_{xx}\mathcal{C}_1+k_{zz}\mathcal{C}_2+2k_{xz}\mathcal{C}_3)/J^2 \\
\mathcal{A}_5 &= (k_{xx}\mathcal{C}_4+k_{zz}\mathcal{C}_5+2k_{xz}\mathcal{C}_6)/J^2
\end{aligned} \tag{B.5}$$

with the $\mathcal{C}_i$ coefficients given by:

$$\begin{aligned}
\mathcal{C}_1 &= z_\eta z_{\xi\eta}-z_\xi z_{\eta\eta}+(z_\eta z_\xi J_\eta-z_\eta^2 J_\xi)/J \\
\mathcal{C}_2 &= x_\eta x_{\xi\eta}-x_\xi x_{\eta\eta}+(x_\eta x_\xi J_\eta-x_\eta^2 J_\xi)/J \\
\mathcal{C}_3 &= z_{\eta\eta}x_\xi-z_{\xi\eta}x_\eta+(x_\eta z_\eta J_\xi-x_\xi z_\eta J_\eta)/J \\
\mathcal{C}_4 &= z_\xi z_{\xi\eta}-z_{\xi\xi}z_\eta+(z_\eta z_\xi J_\xi-z_\xi^2 J_\eta)/J \\
\mathcal{C}_5 &= x_\xi x_{\xi\eta}-x_{\xi\xi}x_\eta+(x_\eta x_\xi J_\xi-x_\xi^2 J_\eta)/J \\
\mathcal{C}_6 &= x_\eta z_{\xi\xi}-x_\xi z_{\xi\eta}+(z_\eta x_\xi J_\eta-x_\eta z_\xi J_\xi)/J
\end{aligned} \tag{B.6}$$

The corresponding Jacobians appearing in the $\mathcal{C}_i$ expressions are given by:

$$\begin{aligned}
J_\xi &= z_\eta x_{\xi\xi}+z_{\xi\eta}x_\xi-x_{\xi\eta}z_\xi-z_{\xi\xi}x_\eta \\
J_\eta &= z_\eta x_{\xi\eta}+z_{\eta\eta}x_\xi-x_{\eta\eta}z_\xi-z_{\xi\eta}x_\eta
\end{aligned} \tag{B.7}$$

In the same way, the resin flow equation 2.3 is transformed, and the result is:

$$\mathcal{B}_1\frac{\partial^2 P}{\partial \xi^2}+\mathcal{B}_2\frac{\partial^2 P}{\partial \eta^2}+\mathcal{B}_3\frac{\partial^2 P}{\partial \xi \partial \eta}+\mathcal{B}_4\frac{\partial P}{\partial \xi}+\mathcal{B}_5\frac{\partial P}{\partial \eta}=\mu m_v\frac{\partial P}{\partial t} \tag{B.8}$$

where,

$$\begin{aligned}
\mathcal{B}_1 &= (S_{xx}z_\eta^2 - 2S_{xz}x_\eta z_\eta + S_{zz}x_\eta^2)/J^2 \\
\mathcal{B}_2 &= (S_{xx}z_\xi^2 - 2S_{xz}x_\xi z_\xi + S_{zz}x_\xi^2)/J^2 \\
\mathcal{B}_3 &= [-2S_{xx}z_\eta z_\xi - 2S_{zz}x_\xi x_\eta + 2S_{xz}(x_\xi z_\eta + x_\eta z_\xi)]/J^2 \\
\mathcal{B}_4 &= (S_{xx}\mathcal{C}_1 + S_{zz}\mathcal{C}_2 + 2S_{xz}\mathcal{C}_3)/J^2 \\
\mathcal{B}_5 &= (S_{xx}\mathcal{C}_4 + S_{zz}\mathcal{C}_5 + 2S_{xz}\mathcal{C}_6)/J^2
\end{aligned} \tag{B.9}$$

# Appendix C

# Normal vectors for curvilinear cells:

The normal vector for a curvilinear cell shown in Figure C.1 according to Trafford [65] is:

$$\frac{\partial f}{\partial n} = \nabla f . \hat{n} \tag{C.1}$$

where the normal vectors are defined as:

$$\begin{aligned} \hat{n}_{(+\xi)} &= \frac{y_\eta . \hat{i} - x_\eta . \hat{j}}{\sqrt{\vartheta}} \\ \hat{n}_{(+\eta)} &= \frac{x_\xi . \hat{j} - y_\xi . \hat{i}}{\sqrt{\gamma}} \\ \hat{n}_{(-\xi)} &= \frac{-y_\eta . \hat{i} + x_\eta . \hat{j}}{\sqrt{\vartheta}} \\ \hat{n}_{(-\eta)} &= \frac{-x_\xi . \hat{j} + y_\xi . \hat{i}}{\sqrt{\gamma}} \end{aligned} \tag{C.2}$$

and

$$\begin{aligned} \wp &= \left(\frac{\partial x}{\partial \eta}\right)^2 + \left(\frac{\partial z}{\partial \eta}\right)^2 \\ \gamma &= \left(\frac{\partial x}{\partial \xi}\right)^2 + \left(\frac{\partial z}{\partial \xi}\right)^2 \end{aligned}$$

Since the gradient of $f$ is

$$\nabla f = \left[ \left( f_\xi y_\eta - f_\eta y_\xi \right) \hat{i} - \left( f_\eta x_\xi - f_\xi x_\eta \right) \hat{j} \right] \frac{1}{J} \tag{C.3}$$

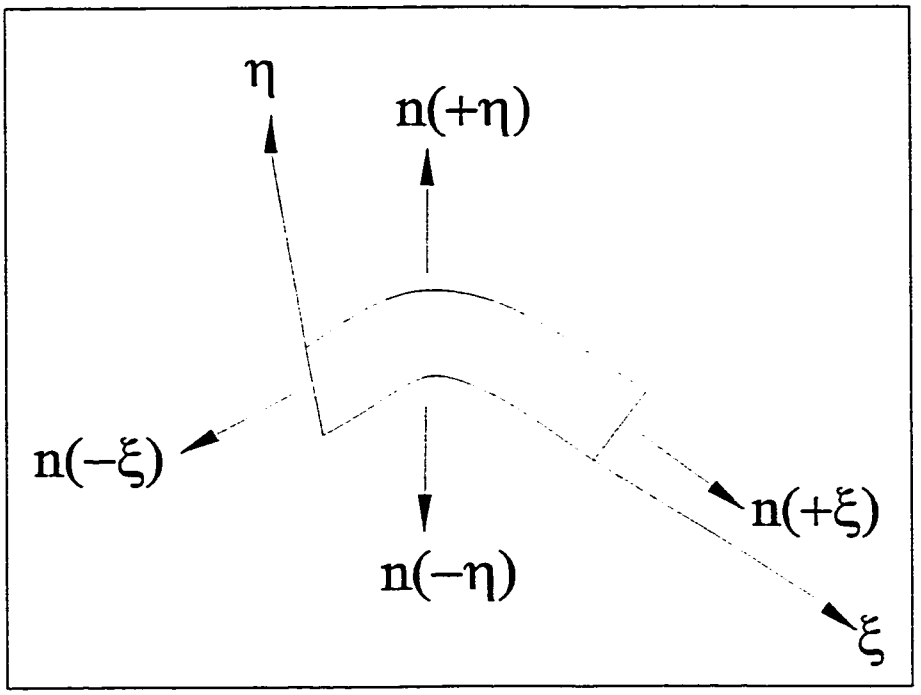


Figure C.1: Normal vectors on the different faces.

where

$$J = z_\eta x_\xi - z_\xi x_\eta$$

then the normal gradient for each side of the curvilinear cell would be:

$$\begin{aligned}
\frac{\partial f}{\partial n} &= \frac{\vartheta f_\xi - \beta f_\eta}{J\sqrt{\vartheta}} \quad \text{on the } (+\xi)\text{face} \\
\frac{\partial f}{\partial n} &= \frac{\gamma f_\eta - \beta f_\xi}{J\sqrt{\gamma}} \quad \text{on the } (+\eta)\text{face} \\
\frac{\partial f}{\partial n} &= \frac{\beta f_\eta - \vartheta f_\xi}{J\sqrt{\vartheta}} \quad \text{on the } (-\xi)\text{face} \\
\frac{\partial f}{\partial n} &= \frac{\beta f_\xi - \gamma f_\eta}{J\sqrt{\gamma}} \quad \text{on the } (-\eta)\text{face}
\end{aligned} \tag{C.4}$$

Since these derivatives occur at the boundaries, then they are represented by one–sided differences.

# Appendix D

# Hercules 3501–6 Epoxy Resin

## D.1 Introduction

Epoxies are the structures characterized by the presence of the epoxide group:

This epoxide qroup is a 3–membered cyclic ether which is reactive with a wide variety of reagents. Epoxy resins are characterized by good mechanical strength, chemical resistance, and electrical properties. Epoxy use in composites is dominated by prepregs, printed circuit board, and filament winding applications, which accounts for 80% of composite usage [73]. In curing epoxy resins, three main groups are used. These include: amines, anhydrides and catalytic curing agents.

## D.2 Hercules 3501-6

The composition of Hercules 3501-6 resin is given in tableD.1 [73].

| | |
|---|---|
| Epoxide No. 1 (H) | 100 |
| Curing Agent (DDS) | 44 |
| Epoxide No. 2 (H) | 16 |
| Epoxide No. 3 (H) | 15 |
| $BF_3$ | 2 |

Table D.1: The composition of Hercules 3501-6 resin. Ammounts are in parts per hundred.

The base resin for Hercules 3501-6 is the TGMDA (tetraglycidyle methelene dianilyne) resin known as Ciba-Geigy MY-720. It's composition is shown in Figure D.1. The DDS (diamino-diphenyl sulfone) curing agent is an aromatic amine that requires elevated temperature for complete cures. It's structure is shown in Figure D.2. The lewis acid $BF_3$ is a catalytic agent used to promote epoxy homopolymerization to achieve full cure. The cure chemistry of the amine-epoxy reaction is shown in Figure D.3.

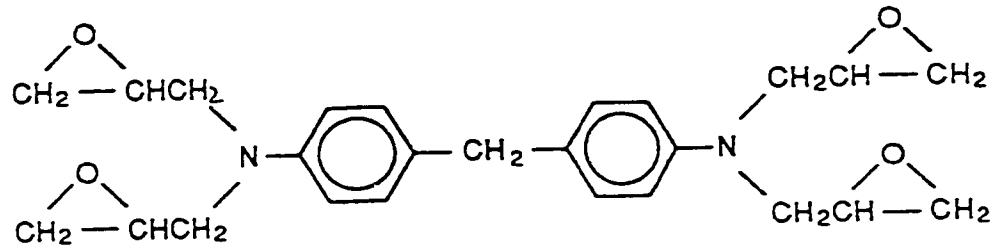

Figure D.1: Ciba-Geigy MY-720.

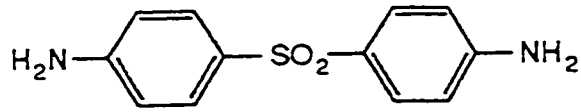

Figure D.2: DDS Curing agent.

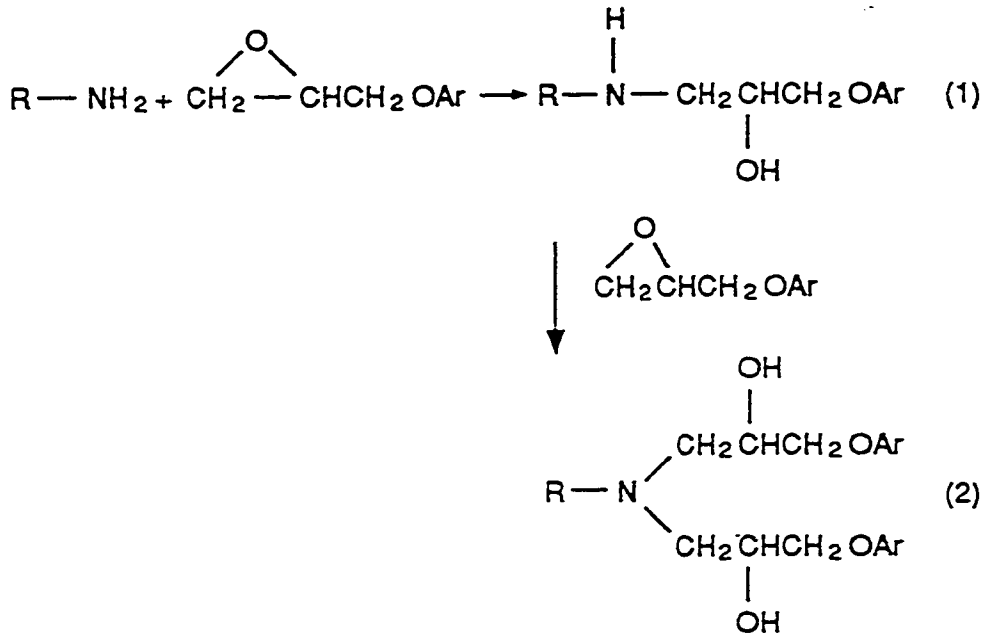

Figure D.3: Amine–epoxy reaction.

# Appendix E

# TA Instruments Dielectric Analyzer

## E.1 Technical Specifications

The following tables contain the technical specifications for the Dielectric Analyzer, such as measurement ranges, sampling system, and physical specifications.

## E.2 TA Instruments Thermal Analyst Controller

The controller is a computer that performs the following functions:

- Allows operator interface with and control of the system
- Stores experimental data
- Runs data analysis programs.

| | |
|---|---|
| Frequency range | 0.003 Hz to 100 kHz |
| Maximum number of frequencies scanned per experiment | 28 |
| Temperature range for Remote single surface sensor | $-100°C$ to $230°C$ |
| Applied voltage | 1 volt |
| Phase angle accuracy at 1 kHz | $10^{-4}$ radians |
| Tan $\delta$ sensitivity at 1 kHz | $1 \times 10^{-4}$ |
| Dielectric constant sensitivity at 1 kHz | 0.01 |
| Dielectric constant range | 1 to $10^5$ |
| Loss factor range | 0 to $10^8$ |
| Ionic conductivity range | $10^{-5}$ to $10^{10}$ pmhos/cm |

Table E.1: Measurement Ranges

| Dimensions | Remote single surface |
|---|---|
| Length | 3.8 mm |
| Width | 2.5 mm |
| Minimum Thickness | 0.013 mm |
| Maximum Thickness | no limit |

Table E.2: Sampling System

| | |
|---|---|
| Dimensions ($h \times w \times d$) | $21'' \times 23'' \times 17''$ |
| Weight | 70 pounds |
| Power requirements | 115V 50/60 Hz |

Table E.3: Physical Specifications of the TA instrument

All TA Instruments computer–based thermal analysis controllers have three components: Monitor, Keyboard, and System unit. The DEA executes experiments under the direction of the controller.

The Remote Single Surface Mode is used for surface property evaluations and curing experiments. In addition, because of its flexible design and ribbon–cable leads, it can be embedded in a sample of any size for product development. Applications include monitoring dielectric properties of a polymer during molding, or while exposed to adverse environments such as solvents or ultra–violet light. It is also possible to embed the sensor in full–sized prototype products during development for long–term test of end–use performance or stability and heat history during storage. In this mode, the sample is returned periodically to the instrument for evaluation.

The remote sensor uses co–planar interdigitated–comb electrode array vapor–deposited on a silicon substrate supported by a carrier of polyimide film and connected to conductors in the ribbon cable. The connector end of the ribbon cable is plugged into an interface box, which is connected to the front of the module. The flexibility of the cable and small sensor size, together with the use of a single amplifier in the integrated circuit adjacent to the sensor array, allows the sensor to monitor a sample up to 10 feet away from the instrument. Sample temperature is measured by a thermal diode adjacent to the sensing array. e' and e" are calculated from the current and phase data using a calibration table stored in module memory.

# Bibliography


[1] F. N. Cogswell, *Thermoplastic Aromatic Polymer Composites.* Butterworth–Heinemann Ltd., Oxford, 1992.

[2] T. E. Twardowski, S. E. Lin, and P. H. Geil, "Curing in thick composite laminates: Experiment and simulation," *J. Composite Materials*, vol. 27, pp. 216–250, 1993.

[3] T. A. Bogetti and J. W. Gillespie, "Two–dimensional cure simulation of thick thermosetting composites," *J. Composite Materials*, vol. 25, pp. 239–273, 1991.

[4] A. C. Loos and G. S. Springer, "Curing of epoxy matrix composites," *J. Composite Materials*, vol. 17, pp. 135–169, 1983.

[5] T. A. Bogetti and J. W. Gillespie, "Process-induced stress and deformation in thick section thermosetting composite laminates," in *21t SAMPE Technical Conference, New Jersy*, Sept. 1989.

[6] M. Hojjati and S. V. Hoa, "Curing simulation of thick thermosetting composites," *Composites Manufacturing*, vol. 5, no. 3, pp. 159–171, 1994.

[7] A. O. Kays, *Exploratory Development on Processing Science of Thick Section Composites.* Technical Report, AFWAL-TR-85-4090, Air Force Wright Aeronautical Laboratories, Wright Patterson AFB, OH, 1985.

[8] L. N. Hjellming and J. S. Walker, "Thermal curing cycles for composite cylinders with thick walls and thermoset resins," *J. Composite Materials*, vol. 23, pp. 1048–1064, 1989.

[9] T. W. McGann and E. R. Crilly, "Preparation for cure," in *Engineering Materials Handbook, Vol.1-Composites, ASM International, USA*, 1987.

[10] R. Dave, J. L. Kardos, and M. P. Dudukovic, "A model for resin flow during composite processing: Part 1- general mathematical development," *Polymer Composites*, vol. 8, pp. 29–38, 1987.

[11] S. R. White and H. T. Hahn, "Cure cycle optimization for the reduction of processing-induced residual stresses in composite materials," *J. Composite Materials*, vol. 27, pp. 1352–1378, 1993.

[12] P. Olivier, J. P. Cottu, and B. Ferret, "Effects of cure cycle pressure and voids on some mechanical properties of carbon/epoxy laminates," *J. Composite Materials*, vol. 26, pp. 509–515, 1995.

[13] P. R. Ciriscioli and Q. Wang, "Curing of epoxy matrix composites," *J. Composite Materials*, vol. 17, pp. 135–169, 1983.

[14] X. Xu and V. Galiatsatos, "Dielectric cure characterization of model elastomers," *Macromolecular Symposia*, no. 76, pp. 137–143, 1993.

[15] D. R. Day, "Cure characterization of thick SMC parts using dielectric and finite difference analysis," *J. Reinforced Plastics and Composites*, vol. 13, no. 10, pp. 918–926, 1994.

[16] F. Stephan, G. Seytre, G. Boiteux, and J. Ulanski, "Study of dielectric response of pmr–15 resin during cure," *J. Non–Crystalline Solids*, vol. 172, no. 2, pp. 1001–1011, 1994.

[17] G. Maistros and I. V. Partridge, "Dielectric monitoring of cure in a commercial carbon–fiber composite," *Composites Science and Technology*, vol. 53, pp. 355–359, 1995.

[18] D. D. Shepard, D. R. Day, and K. J. Craven, "Applications of dielectric analysis for cure monitoring and control in the polyester SMC/BMC molding industry," *J. Reinforced Plastics and Composites*, vol. 14, pp. 297–308, 1995.

[19] G. Levita, A. Livi, P. A. Rolla, and C. Culicchi, "Dielectric monitoring of epoxy cure," *J. Polymer Science: Part B: Polymer Physics*, vol. 34, pp. 2731–2737, 1996.

[20] V. Shtrauss, A. Kalpinsh, U. Lomanovskis, and J. Rotbahs, "Resin cure monitoring systems based on nondestructive dielectric spectrometry," *Mechanics of Composite Materials*, vol. 32, no. 3, pp. 279–285, 1996.

[21] Y. Deng and G. C. Martin, "Modeling diffusion during thermoset cure: An approach based on dielectric analysis," *Macromolecules*, vol. 27, pp. 5141–5146, 1994.

[22] J. O. Sympson and S. A. Bidstrup, "Rheological and dielectric changes during isothermal epoxy–amine cure," *J. Polymer Science: Part B: Polymer Physics*, vol. 33, pp. 55–62, 1995.

[23] S. Radhakrishnan, D. Hayward, A. J. Mackinnon, and R. A. Pethrick, "Investigation of cure in epoxy acrylate resins using rheological and dielectric measurements," *Polymer Engineering and Science*, vol. 35, no. 2, pp. 184–189, 1995.

[24] J. Mijovic, S. Andjelic, B. Fitz, W. Zurawsky, I. Mondragon, F. Bellucci, and L. Nicolais, "Impedance spectroscopy of reactive polymers. 3. correlations between dielectric, spectroscopic, and rheological properties during cure of a trifunctional epoxy resin," *J. Polymer Science: Part B: Polymer Physics*, vol. 34, pp. 379–388, 1996.

[25] Y. Deng and G. C. Martin, "Analysis of the cure–dependent dielectric relaxation behavior of an epoxy resin," *J. Polymer Science: Part B: Polymer Physics*, vol. 32, pp. 2115–2125, 1994.

[26] D. Alperstein, M. Narkis, and A. Siegmann, "Modeling the dielectric response of unsaturated polyester resin during cure," *Polymer Engineering and Science*, vol. 35, no. 3, pp. 284–288, 1995.

[27] D. R. Day, "Degree of cure in 3501–6 epoxy graphite: A comparison of dielectric cure index with model predictions," *Proceedings of the 35th International SAMPE Symposium*, pp. 2289–2297, 1990.

[28] P. R. Ciriscioli and G. S. Springer, "Dielectic cure monitoring – a critical review," *SAMPE Journal*, vol. 25, no. 3, pp. 35–42, 1989.

[29] L. Tredoux and J. van der Westhuizen, "Development of a numerical code that simulates combined heat transfer, resin flow and compaction during composites processing," *Composites Manufacturing*, vol. 6, no. 2, pp. 85–92, 1995.

[30] B. Joseph, F. W. Hanratty, and J. L. Kardos, "Model based control of voids and product thickness during autoclave curing of carbon/epoxy composite laminates," *J. Composite Materials*, vol. 29, no. 8, pp. 1000–1024, 1995.

[31] M. H. Chang, C. L. Chen, and W. B. Young, "Optimal design of the cure cycle for consolidation of thick composite laminates," *Polymer Composites*, vol. 17, no. 5, pp. 743–750, 1996.

[32] S. B. Shim, J. C. Seferis, and W. Hudson, "Process induced void formation in a high performance structural composites system manufactured by autoclave layup processing," *J. Advanced Materials*, vol. 28, no. 4, pp. 26–36, 1997.

[33] J. S. Kim and D. G. Lee, "Development of an autoclave cure cycle with cooling and reheating steps for thick thermoset composite laminates," *J. Composite Materials*, vol. 31, no. 22, pp. 2264–2282, 1997.

[34] S. D. Gilmore and S. I. Guceri, "Solidification in anisotropic thermoplastic composites," *Polymer Composites*, vol. 11, pp. 406–416, 1990.

[35] A. Johnston, P. Hubert, G. Fernlund, R. Vaziri, and A. Poursartip, "Process modeling of composite structures employing a virtual autoclave concept," *Science and Engineering of Composite Materials*, vol. 5, pp. 235–252, 1996.

[36] J. M. Kenny, A. Trivisano, and L. A. Berglund, "Chemorheological and dielectic behavior of the epoxy matrix in a carbon fiber prepreg," *SAMPE Journal*, vol. 27, no. 2, pp. 39–45, 1991.

[37] P. R. Ciriscioli, Q. Wang, and G. S. Springer, "Autoclave curing – comparisons of model and test results," *J. Composite Materials*, vol. 26, no. 1, pp. 90–102, 1992.

[38] J. S. Kim and D. G. Lee, "Measurement of the degree of cure of carbon fiber epoxy composite materials," *J. Composite Materials*, vol. 30, pp. 1436–1457, 1996.

[39] A. Maffezzoli, A. Trivisano, M. Opalicki, J. Mijovic, and J. M. Kenny, "Correlation between dielectric and chemorheological properties during cure of epoxy–based composites," *J. Materials Science*, vol. 29, pp. 800–808, 1994.

[40] C. C. Hiel, M. Smith, and D. Chappell, "A curved beam test specimen for determining the interlaminar tensile strength of laminated composites," *J. Composite Materials*, vol. 25, pp. 854–868, 1991.

[41] R. L. Ramkumar, G. Grimes, D. Adams, and E. Dusablon, *Effects of Materials and Process Defects on the Compression Properties of Advanced Composites.* Final Technical Report, Contract Nos. N00019–80–C–0490 and N00019–80–C–0484, Naval Air Systems Command, 1982.

[42] J. E. McCarty and M. M. Ratwani, *Damage Tolerance of Composites.* Interim Report No. 1, Contract No. F33615–82–C–3213, Air Force Wright–Aeronautical Laboratory, Wright–Patterson Air Force Base, OH, 1983.

[43] R. H. Martin, "Delamination failure in a unidirectional curved composite laminate," *Composite Materials: Testing and Design (Tenth Volume), ASTM STP 1120*, pp. 365–383, 1992.

[44] W. C. Jackson and R. Martin, "An interlaminar tensile strength specimen," *Composite Materials: Testing and Design (Eleventh Volume), ASTM STP 1206*, pp. 333–354, 1993.

[45] R. H. Martin and W. C. Jackson, "Damage prediction in cross–plied curved composite laminates," *Composite Materials: Fatigue and Fracture (Fourth Volume), ASTM STP 1156*, pp. 105–126, 1993.

[46] W. C. Jackson and P. G. Ifju, "Through–the–thickness tensile strength of textile composites," *Composite Materials: Testing and Design (Twelfth Volume), ASTM STP 1274*, pp. 218–238, 1996.

[47] K. N. Shivakumar, H. G. Allen, and V. S. Avva, "Interlaminar tension strength of graphite/epoxy composite laminates," *AIAA Journal*, vol. 32, pp. 1478–1484, 1994.

[48] V. S. Avva, H. G. Allen, and K. N. Shivakumar, "Through–the–thickness tension strength of 3–d braided composites," *J. Composite Materials*, vol. 30, pp. 51–68, 1996.

[49] G. S. Springer, "A model of the curing process of epoxy matrix composites," *Progress in Science and Engineering of Composite Materials*, vol. 1, pp. 23–35, 1982.

[50] J. T. Lindt, "Mechanical principles of formation of fiber reinforced materials," in *2nd International Conference on Reactive Processing of Polymers, Pittsburgh*, 1982.

[51] J. C. Halpin, J. L. Kardos, and M. P. Dudukovic, "Processing science: An approach for prepreg composite systems," *Pure and Applied Chemistry*, vol. 55, no. 5, 1983.

[52] T. G. Gutowski, T. Morigaki, and Z. Cai, "The consolidation of laminate composites," *J. Composite Materials*, vol. 21, pp. 172–188, 1987.

[53] M. R. Kamal, "Thermoset characterization for moldability analysis," *Polymer Engineering And Science*, vol. 14, no. 3, pp. 231–239, 1974.

[54] S. C. Mantell and P. R. Ciriscioli, "Cure model for ici feberite 977–2 and 977–3 resins," in *38th International SAMPE Symposium*, 1993.

[55] W. I. Lee, A. C. Loos, and G. S. Springer, "Heat of reaction, degree of cure, and viscosity of 3501-6 resin," *J. Composite Materials*, vol. 16, pp. 510–520, 1982.

[56] J. L. Kardos, M. P. Dudukovic, and R. Dave, "Void growth and resin transport during processing of thermosetting matrix composites," *Advances in Polymer Science*, vol. 80, p. 101, 1986.

[57] R. S. Dave, A. Mallow, J. L. Kardos, and M. P. Dudukovic, "Science-based guidelines for the autoclave process for composites manufacturing," *SAMPE Journal*, vol. 26, pp. 31–37, 1990.

[58] W.-B. Young, "Compacting pressure and cure cycle for processing of thick composite laminates," *Composites Science and Technology*, vol. 54, no. 3, pp. 299–306, 1995.

[59] B. T. Astrom, R. B. Pipes, and S. G. Advani, "On flow through aligned beds and its application to composite processing," *J. Composite Materials*, vol. 26, no. 9, pp. 1351–1373, 1992.

[60] B. R. Gebart, "Permeability of unidirectional reinforcement for RTM," *J. Composite Materials*, vol. 26, no. 8, pp. 1100–1134, 1992.

[61] J. F. Thompson, F. C. Thames, and C. W. Mastin, "Automatic numerical generation of body-fitted curvilinear coordinate systems for field containing any number of arbitrary two-dimensional bodies," *Journal of Computational Physics*, vol. 15, pp. 299–319, 1974.

[62] J. F. Thompson, Z. A. U. Waris, and C. W. Mastin, "Body-fitted coordinate systems for numerical solution of partial differential equations - a review," *J. Computational Physics*, vol. 47, pp. 1–108, 1982.

[63] S. Gilmore, *TGMESH User's Manual.* Center for Composite Materials, University of Delaware, Newark, DE, 1989.

[64] T. A. Bogetti, *Process Induced Stress and Deformation in Thick-Section Thermosetting Composites.* PhD thesis, University of Delaware, Newark, DE, 1989.

[65] D. Trafford, "Computational analysis and simulation of the mold filling process for hele–shaw flows," tech. rep., CAE Report–3/86, Department of Mechanical Engineering, University of Delaware, Newark, DE, 1986.

[66] G. M. Martinez, "Fast cures for thick laminated organic matrix composites," *Chemical Engineering Science*, vol. 46, no. 2, pp. 439–450, 1991.

[67] G. S. Springer and S. W. Tsai, "Thermal conductivity's of unidirectional materials," *J. Composite Materials*, vol. 1, pp. 166–173, 1967.

[68] J. ven der Westhuizen and J. P. D. Plessis, "Quantification of unidirectional fiber bed permeability," *J. Composite Materials*, vol. 28, pp. 619–637, 1994.

[69] J. van der Westhuizen and J. P. D. Plessis, "An attempt to quantify fiber bed permeability utilizing the phase average navier–stokes equation," *Composites. part a, applied science and manufacturing*, vol. 27, pp. 263–269, 1996.

[70] R. Dave, J. L. Kardos, and M. P. Dudukovic, "A model for resin flow during composite processing: Part 2–numerical analysis for unidirectional graphite/epoxy laminates," *Polymer Composites*, vol. 8, pp. 123–132, 1987.

[71] H. Z. Barakat and J. A. Clark, "On the solution of the diffusion equations by numerical methods," *J. Heat Transfer*, pp. 421–427, 1966.

[72] H. P. Kan, N. M. Bhatia, and M. A. Mahler, "Effect of porosity on flange–web corner strength," *Composite Materials: Fatigue and Fracture*, vol. 3, pp. 126–139, 1991.

[73] J. F. Carpenter, "Test program evaluation of hercules 3501-6 resin," tech. rep., Report No. N0009–77–C—155 McDonnell Aircraft Company, St. Lois, Missourri, 1978.